UNIVERSIDADE DE SANTIAGO DE COMPOSTELA
FACULTADE DE MATEMÁTICAS

Programa de Doutoramento en Métodos Matemáticos e Simulación Numérica en Enxeñaría e Ciencias Aplicadas

Ph.D. Thesis

Time series methods for SHM applications and multiple coherence computations: assessment in real and laboratory conditions

Ana Gómez González

Supervised by Jerónimo Rodríguez García

November 2016

USC
UNIVERSIDADE
DE SANTIAGO
DE COMPOSTELA

DON JERÓNIMO RODRÍGUEZ GARCÍA, Doctor en Ciencias (especialidad en Matemática Aplicada) por la Universidad de Paris-Dauphine (título homologado por la Universidad de Santiago de Compostela), como Profesor Contratado Doctor del Departamento de Matemática Aplicada de la Universidad de Santiago de Compostela,

INFORMA:
Como director de la Tesis Doctoral titulada:

Time series methods for SHM applications and multiple coherence computations: assessment in real and laboratory conditions

Presentada por Doña Ana Gómez González, alumna del Programa de Doctoramiento en Métodos Matemáticos y Simulación Numérica en Ingeniería y Ciencias Aplicadas

Autoriza la presentación de la tesis indicada, considerando que reúne los requisitos exigidos en el artículo 34 del reglamento de Estudios de Doctoramiento, y que como Director de la misma no incurre en las causas de abstención establecidas en la ley 40/2015.

En Santiago de Compostela, a 28 de noviembre de 2016.

El director: La doctoranda:

Jerónimo Rodríguez García Ana Gómez González

USC
UNIVERSIDADE
DE SANTIAGO
DE COMPOSTELA

A Cova, por todo lo que me has enseñado

USC
UNIVERSIDADE
DE SANTIAGO
DE COMPOSTELA

Acknowledgements

I cannot start without thanking everyone that has contributed to the development of the present thesis.

Firstly, I would like to thank my supervisor, Jerónimo Rodríguez for all his support and guidance throughout the development of this thesis. I also need to thank Alfredo Bermúdez de Castro and Xabier Sagartzazu, who introduced me to the topic and helped in the initial and subsequent steps. I cannot forget Spilios D. Fassois, thank you for your warm reception and for everything you taught me during my stay in Patras. Without all your help this thesis would have not been possible. I also want to express my gratitude to David Avendaño and Claus–Peter Fritzen for their reports and suggestions that helped me to improve the document in the final steps. Thank you as well to the committee members for accepting to supervise the present work.

Thank you to the FPU program, the Vibroacoustic projects from Orona in IK4–Ikerlan and the SYSWIND project for their essential financial support.

Of course, thanks to all my colleagues during this time: the Applied Mathematics Department in the University of Santiago de Compostela, the Mechanical Engineering and the Sensors Department in IK4–Ikerlan and last, but not least, the Stochastic Mechanical Systems & Automation (SMSA) Laboratory in the University of Patras. Most of you have not only been colleagues, helping to the successful completion of the work, but also friends.

Thank you to all my friends, starting from childhood friends, but also including the ones that I met during the development of the thesis (you know who you are).

Special thanks to my family, en especial a mis padres que me han ayudado y apoyado en cada una de las etapas de mi vida, sin olvidarme de César, que siempre ha estado ahí.

Thank you very much

Muchas gracias

Graciñas

Eskerrik asko

Ευχαριστώ πολύ

Abstract

Ana Gómez González – Time series methods for SHM applications and multiple coherence computations: assessment in real and laboratory conditions.

This doctoral thesis studies times series methods for different industrial applications in two fields: structural health monitoring and multiple coherence method. In both fields, different time series methods are used and proposed with a validation in several laboratory and real applications, including a lab–scale wind turbine tower and blade or a real elevator. More specifically:

i) Structural Health Monitoring (SHM): The aim in this first line of research is to develop methods to assess the health of a structure (if it has damage or not, location of the damage). SHM is defined as the process of acquiring and analyzing data from on–board sensors to evaluate the health of a structure. SHM methods can be physics based, which require in general a Finite Element Model (FEM) of the whole structure, or non–physics/data based, in the scope of the present work only data based methods will be considered. In particular all methods presented belong to the class of vibration–based methods, in which the response of the structure, and maybe also the excitation, is measured via appropriate sensors. It is supposed that damage will affect the response of the structure and these changes can be detected. Non–parametric (based on the Frequency Response Function, FRF, or the Power Spectral Density, PSD) and parametric (based on AutoRegressive, AR) techniques will be used. For all of them a learning phase will be performed in order to characterize the structure in the healthy state. Then, in the inspection phase, some characteristic of the signals obtained in the current state is compared (by hypothesis testing) with the corresponding one from the learning phase. For these type of methods it is very important to take into account the changing environmental and operational conditions (EOC), so that a change in these conditions will not produce a false alarm. In this sense, a supervised technique based on Principal Component Anal-

ysis (PCA) will be presented. Additionally some extensions to identify and localize the damage are considered. For the first case, the identification of the type of damage will be possible thanks to a learning process based on each available damage. Regarding the localization of the damage, an AR model in which the involved parameters depend on the position of the damage is used. These methods have been successfully applied to data obtained on a laboratory tower that simulates an offshore wind turbine and in a lab–scale wind turbine blade.

ii) Multiple Coherence Method (MCM): The second line of research is within the framework of multiple coherence calculations for non–stationary signals. The ultimate goal in this line is to identify the predominant sources of noise in different situations. Coherence calculation involves obtaining power spectral densities (autospectra and cross–spectra) of the signals involved. To do so classic methods are based on both the fast Fourier transform and parametric modeling (AR methods, for example). Both methods assume that the signals are stationary which, in many applications (like in the case of a moving source or receptor), is not satisfied, so there is the need to extend these techniques to non–stationary situations. In order to make such an extension, two alternatives have been explored. The first, unstructured, is to divide the signal into blocks using in each of them a technique for stationary signals. The autospectra and cross–spectra obtained with these methods have a great variability in time, which needs to be corrected performing averages in time. The second alternative, FS–TAR techniques, is to impose on the coefficients of the AR model a temporary dependency with a structure imposed a priori. This reduces the number of parameters involved and the temporal variability of the calculated spectra. The developed methods have been validated on experimental data: measurements in a semi–anechoic chamber with moving source and measurements in the shaft and cabin of an elevator.

Resumen

Ana Gómez González – Time series methods for SHM applications and multiple coherence computations: assessment in real and laboratory conditions.

Esta tesis doctoral estudia métodos de series temporales para diferentes aplicaciones industriales en dos ámbitos: monitorización estructural y método de la coherencia múltiple. En ambos campos, se usan y proponen diversos métodos de series temporales con su validación en varias aplicaciones de laboratorio y reales. De forma más específica:

i) Monitorización estructural: Esta primera línea de investigación se inscribe en el marco de la monitorización estructural (SHM, *Structural Health Monitoring*). El objetivo es elaborar métodos que permitan evaluar el estado de salud de una estructura (si contiene daño o no; localización del daño). SHM se define como el proceso de adquisición y análisis de los datos de los sensores integrados para evaluar la salud de una estructura. Los métodos para SHM pueden ser basados en la física, que requerirán en general un modelo de elementos finitos de toda la estructura, o basados en datos. En el ámbito del presente trabajo se tratarán solo métodos basados en datos. En particular, todos los métodos presentados pertenecen a la clase de los métodos basados en vibraciones, en los cuales se mide la respuesta vibratoria, y en ocasiones también la excitación, a través de los sensores adecuados. Se supone que el daño afectará a la respuesta de la estructura y que dichos cambios pueden ser detectados. Se usarán tanto métodos no paramétricos (basados en la función de respuesta en frecuencia o en la densidad de potencia espectral) como paramétricos (basados en modelización AutoRegresiva, AR). Para todos ellos se llevará a cabo una primera fase de aprendizaje para caracterizar la estructura en el estado sano. A continuación, en la fase de inspección, se comparará (mediante un contraste de hipótesis) el comportamiento de las señales obtenidas en el estado actual con el correspondiente en la fase de aprendizaje. Para este tipo de métodos es muy importante tener en cuenta las cambiantes condiciones medioambientales y operacionales, de forma que un cambio

en estas condiciones no produzca una falsa alarma. En este sentido se presenta una técnica supervisada basada en Análisis de Componentes Principales. Adicionalmente se consideran extensiones para identificar y localizar el daño. La identificación del tipo de daño se hace posible gracias a un proceso de aprendizaje de cada tipo de daño. De cara a la localización del daño se usa un modelo AR en el que los parámetros dependen de la posición del daño. Los métodos presentados han sido aplicados con éxito a datos procedentes de una torre de laboratorio que simula una torre de aerogenerador offshore a escala y en una pala de aerogenerador a escala.

ii) Método de coherencia múltiple (MCM): El objetivo en esta segunda línea es identificar fuentes predominantes de ruido en situaciones no estacionarias mediante el cálculo de coherencias. Esto implica la obtención de las densidades de potencia espectral (autoespectros y espectros cruzados) de las señales involucradas. Para ello los métodos clásicos se basan tanto en la transformada rápida de Fourier como en modelización paramétrica (métodos AR, por ejemplo). Ambos métodos suponen que las señales son estacionarias lo cual, en multitud de aplicaciones (como el estudio de una fuente o receptor en movimiento), no se satisface y motiva la extensión de este tipo de técnicas a situaciones no estacionarias. De cara a realizar tal extensión, se han explorado dos alternativas. La primera de ellas, no estructurada, consiste en dividir la señal en bloques aplicando en cada uno de ellos una técnica para señales estacionarias. Los autoespectros y espectros cruzados proporcionados tienen una gran variabilidad en tiempo que en ocasiones se tiene que corregir realizando medias en tiempo. La segunda alternativa, técnicas FS–TAR, consiste en imponer en los coeficientes del modelo AR una dependencia temporal con una estructura impuesta a priori. Ello reduce el número de parámetros que se deben emplear en el modelado y la variabilidad temporal de los espectros calculados. Los métodos desarrollados se han validado sobre datos experimentales: medidas en cámara semianecoica con fuente en movimiento y medidas realizadas en el hueco y cabina de un ascensor.

Resumo

Ana Gómez González – Time series methods for SHM applications and multiple coherence computations: assessment in real and laboratory conditions.

Esta tese doutoral estuda métodos de series temporais para diferentes aplicacións industriais en dous campos: monitoraxe estructural e método da coherencia múltiple. En ambas liñas de investigación usanse e propoñense diversos métodos de series temporais coa sua validación en varias aplicacións de laboratorio e reais. Específicamente:

i) Monitoraxe estrutural: Esta primeira liña de investigación inscríbese no marco da monitoraxe estrutural (SHM, *Structural Health Monitoring*). O obxectivo é elaborar métodos que permitan avaliar o estado de saúde dunha estrutura (se contén dano ou non; localización do dano). SHM defínese como o proceso de adquisición e análise dos datos dos sensores integrados para avaliar a saúde dunha estrutura. Os métodos para SHM poden ser baseados na física, que requirirán en xeral un modelo de elementos finitos de toda a estrutura, ou baseados en datos. No ámbito do presente traballo trataranse só métodos baseados en datos. En particular, todos os métodos presentados pertencen á clase dos métodos baseados en vibracións, nos cales se mide a resposta vibratoria, e en ocasións tamén a excitación, a través dos sensores adecuados. Suponse que o dano afectará á resposta da estrutura e que estes cambios poden ser detectados. Usaranse tanto métodos non paramétricos (baseados na función de resposta en frecuencia ou na densidade de potencia espectral) como paramétricos (baseados en modelización AutoRegresiva, AR). Para todos eles levará a cabo unha primeira fase de aprendizaxe para caracterizar a estrutura no estado san. A continuación, na fase de inspección, compararase (mediante un contraste de hipótese) o comportamento dos sinais obtidos no estado actual co correspondente na fase de aprendizaxe. Para este tipo de métodos é moi importante ter en conta as cambiantes condicións ambientais e operacionais, de forma que un cambio nestas condicións non produza unha falsa alarma. Neste sentido preséntase unha técnica su-

pervisada baseada en Análise de Componentes Principais (PCA). Ademais considéranse extensións para identificar e localizar o dano. No primeiro caso, a identificación do tipo de dano faise posible grazas a un proceso de aprendizaxe de cada tipo de dano. Para a localización do dano úsase un modelo AR no que os parámetros dependen da posición do dano. Os métodos presentados foron aplicados con éxito a datos procedentes dunha torre de laboratorio que simula unha torre de aeroxerador offshore a escala e nunha pa de aeroxerador a escala.

ii) Método da coherencia múltiple (MCM): O obxectivo nesta segunda liña é identificar as fontes predominantes de ruído en situacións non estacionarias mediante o cálculo de coherencias. Isto implica a obtención das densidades de potencia espectral (autoespectros e espectros cruzados) dos sinais involucrados. Para iso os métodos clásicos baséanse tanto na transformada rápida de Fourier como en modelización paramétrica (métodos AR, por exemplo). Ambos métodos supoñen que os sinais son estacionarios o cal, en multitude de aplicacións (como o estudo dunha fonte ou receptor en movemento), non se satisfai e motiva a extensión deste tipo de técnicas a situacións non estacionarias. Para realizar tal extensión, exploráronse dúas alternativas. A primeira delas, non estruturada, consiste en dividir o sinal en bloques aplicando en cada un deles unha técnica para sinais estacionarios. Os autoespectros e espectros cruzados proporcionados teñen unha gran variabilidade en tempo que en ocasións tense que corrixir realizando medias en tempo. A segunda alternativa, técnicas FS–TAR, consiste en impoñer nos coeficientes do modelo AR unha dependencia temporal cunha estrutura imposta a priori. Iso reduce o número de parámetros que se deben empregar no modelado e a variabilidade temporal dos espectros calculados. Os métodos desenvolvidos validáronse sobre datos experimentais: medidas en cámara semianecoica con fonte en movemento e medidas realizadas no oco e cabina dun ascensor.

Contents

Acknowledgements i

Abstract iii

Resumen v

Resumo vii

Contents ix

List of Figures xiii

List of Tables xvii

1 Introduction 1

1.1 Structural Health Monitoring 2

1.1.1 Levels in damage diagnosis 3

1.1.2 Damage detection – Level 1 3

1.1.3 Damage localization – Level 2 5

1.1.4 Accounting for varying environmental and operational conditions (EOC) 6

1.1.5 Application in the wind turbine field 8

1.2 Non–stationary analysis: multiple coherence computations 10

1.2.1 Classification of time–frequency methods 10

1.2.2 Application in the elevator field 12

1.3 Thesis goals and organization of chapters 13

2 Damage detection via parametric methods **15**
2.1 Introduction . . . 15
2.2 Autoregressive (AR) model of the involved signals . . . 16
2.3 The damage detection method . . . 17
2.3.1 Learning phase . . . 17
2.3.2 Inspection phase . . . 17
2.3.3 Application notes . . . 19
2.3.4 Extension to a level 2 algorithm . . . 19
2.4 Experimental set–up . . . 19
2.4.1 Tower for damage detection . . . 20
2.4.2 Tower with jacket for damage identification/location . . . 23
2.5 Results . . . 25
2.5.1 Damage detection – Tower without jacket . . . 25
2.5.2 Damage identification – Tower with jacket . . . 32
2.6 Conclusions and future work . . . 35
2.7 Appendix A - Model details (tower with jacket) . . . 36

3 Damage detection under varying EOC **41**
3.1 Introduction . . . 41
3.2 The damage detection methodology . . . 42
3.2.1 Preliminaries . . . 43
3.2.2 Outline of the methodology . . . 45
3.3 Laboratory validation of the methodology . . . 51
3.3.1 The experimental set-up, the damage scenarios, and the experiments 51
3.3.2 Experimental results . . . 55
3.4 Conclusions . . . 69

4 Damage diagnosis in wind turbine blades **71**
4.1 Introduction . . . 71
4.2 The damage diagnosis methodology . . . 72
4.2.1 Baseline phase . . . 72
4.2.2 Inspection phase . . . 73
4.3 Experimental set–up, damages and experiments . . . 75
4.4 Damage detection and localization results . . . 79
4.5 Concluding remarks . . . 87

4.6 Appendix A - Extra figures 88

5 Multiple coherence method in an elevator 95
5.1 Introduction 95
5.2 Theoretical background 96
5.2.1 Univariate case 97
5.2.2 Multivariate case 105
5.2.3 Ordinary and multiple coherence 108
5.3 Numerical and experimental results 109
5.3.1 Univariate analysis of numerical and laboratory signals 110
5.3.2 Experience with a moving source: numerical case 113
5.3.3 Experience with a moving source: experimental case in a semianechoic chamber 119
5.3.4 Elevator signals analysis 122
5.4 Conclusions 134

6 Conclusions and future work 137
6.1 Damage detection and identification 137
6.1.1 Future research 138
6.2 Multiple coherence computations 139
6.2.1 Future research 140

A Polynomial families 141
A.1 Chebyshev polynomials 141
A.2 Legendre polynomials 142
A.3 Bernstein polynomials 142

B Resumen extenso 145
B.1 Monitorización de la salud estructural 146
B.1.1 Niveles en la diagnosis del daño 147
B.1.2 Detección de daño – Nivel 1 147
B.1.3 Localización del daño – Nivel 2 150
B.1.4 Consideración de condiciones medioambientales y operacionales cambiantes 151
B.1.5 Aplicación en el campo de la eólica 152
B.2 Análisis no estacionario: coherencia múltiple 155

B.2.1 Clasificación de métodos tiempo–frecuencia 155
B.2.2 Aplicación en el campo de la elevación (ascensores) 157
B.3 Objetivos y organización de la tesis 158

C List of Publications **161**

Bibliography **163**

List of Figures

1.1 Example of catastrophic event: broken wind turbine. 2
1.2 Distribution of electricity demand divided by sectors, [3]. 9

2.1 Statistical hypothesis testing based on a χ^2- distributed statistic (one–sided test). 18
2.2 Tower photo and sensor enumeration and location 20
2.3 (a) Tower with jacket photo and (b) sensor location. 24
2.4 Damage location in the jacket. 25
2.5 Baseline phase – parametric AR modeling of the healthy structural dynamics for channel 1. 26
2.6 Damage detection results using the channels 1 to 6. 28
2.7 Damage detection results using channels 7 to 12. 29
2.8 Damage detection results using channels 13 to 16. 30
2.9 Damage detection using the sum of channels and thresholds. 30
2.10 Damage detection results. 33
2.11 Damage identification results. 34

3.1 The elements of transformed feature vector $\mathbf{s}$ in relation to dimensionality reduction. 47
3.2 An example of 3-dimensional (three principal components) sets Θ_0 and Θ_d. 50
3.3 Statistical hypothesis testing based on a χ^2- distributed statistic (one–sided test). 51
3.4 Drawing and photo of the lab–scale blade showing the vibration measurement positions. 52
3.5 Detail of the considered damages. 53
3.6 PSD estimates along with 95% confidence intervals for the vibration response at position Y2. 55

3.7 FRF estimates along with 95% confidence intervals for the vibration response signal at position Y2. . . . 56
3.8 The first 50 AR parameter estimates along with their 95% confidence intervals (vibration response signal at position Y2). . . . 58
3.9 Baseline phase – determination of the feature vector reduced dimensionality for each method. . . . 59
3.10 PSD based method – baseline phase (pictorial representation of Steps 5–6 in selecting the principal components to be included). . . . 64
3.11 Baseline Phase: The ratio R_j computed for different iterations in each one of which a new principal component is added. . . . 65
3.12 Inspection Phase – all methods: Damage detection results for data records from the inspection phase based on sensor position Y2 (false alarm probability $\alpha = 10^{-10}$). . . . 66
3.13 FRF based method – baseline phase (pictorial representation of Steps 5–6 in selecting the principal components to be included). . . . 67
3.14 AR parameter based method – baseline phase (pictorial representation of Steps 5–6 in selecting the principal components to be included). . . . 68

4.1 Statistical hypothesis testing based on a normal distributed statistic (two–tailed test). . . . 74
4.2 Drawing and photo of the lab–scale blade showing the damage locations and measurement locations. . . . 77
4.3 Detail of the experimental set-up: the exciter with part of the blade. . . . 77
4.4 Assessment of the effects of the considered damage on the blade dynamics via FRF magnitude comparison . . . 79
4.5 Baseline phase – parametric ARX modeling of the healthy structural dynamics . . . 81
4.6 Baseline phase: FP–ARX(120,120)$_{p=10}$ model based FRF magnitude versus frequency and damage location. . . . 82
4.7 Inspection phase – damage detection results via the FRF magnitude based scheme . . . 83
4.8 Inspection phase – damage localization results for two test cases . . . 84
4.9 Inspection phase – summary damage localization results . . . 85
4.10 Inspection phase – summary damage localization errors . . . 86

4.11 3D FRF magnitude representation with respect to frequency and damage position . . . 88
4.12 FRF magnitude representation. Comparison between healthy and different damage positions . . . 89
4.13 FRF magnitude representation. Comparison between healthy and different damage positions . . . 90
4.14 FRF magnitude representation. Comparison between healthy and different damage positions . . . 91
4.15 Cost function representation for different damage positions . . . 92
4.16 Cost function representation for different damage positions . . . 93
4.17 Cost function representation for different damage positions . . . 94

5.1 Configuration with a static noise source E_s and a moving one E_m, receptor at point R; $x - y$ projection. . . . 96
5.2 PSD obtained in a numeric case with the different methods. . . . 111
5.3 Variation of the first coefficient. . . . 112
5.4 Variation of the second coefficient. . . . 113
5.5 Variation of the third coefficient. . . . 113
5.6 Variation of the fourth coefficient. . . . 114
5.7 PSD obtained in a experimental case with the different methods. . . . 114
5.8 Sketch of the working scenario. . . . 115
5.9 Picture of the working scenario. . . . 116
5.10 Signals received at the receptor point. . . . 117
5.11 Coherences from the numeric case with the STFT method. . . . 117
5.12 Coherences from the numeric case with the Unstructured TAR method. . . . 118
5.13 Coherences from the numeric case with the FS–TAR method. . . . 118
5.14 PSD of the signals measured by the microphones next to each loudspeaker 120
5.15 Coherences from the experimental case with the STFT method . . . 121
5.16 Coherences from the experimental case with the Unstructured TAR method 121
5.17 Coherences from the experimental case with the FS–TAR method . . . 121
5.18 Sketch of the elevator under investigation . . . 123
5.19 Measurement positions in the elevator analysis . . . 124
5.20 PSD in dB of the full signal from an elevator drive machine . . . 126
5.21 PSD in dB of the deceleration part signal from an elevator drive machine . 126

5.22 Coherences from all the inputs and the microphone for the three speed regions considered . . . 127
5.23 Coherences from all the inputs and the accelerometer (direction z) for the three speed regions considered . . . 127
5.24 Representation of the division in groups. . . . 129
5.25 Coherences from inputs in group 1 and the microphone with the Unstructured TAR . . . 130
5.26 Coherences from all inputs in group 1 and the accelerometer (z direction) with the Unstructured TAR method . . . 130
5.27 Coherences from all inputs in group 1 and the accelerometer (z direction) with the STFT method . . . 130
5.28 Coherences from all inputs in group 1 and the accelerometer (direction z) with the FS–TAR method . . . 131
5.29 Coherences from inputs in group 2 and the microphone with the Unstructured TAR method . . . 131
5.30 Coherences from all inputs in group 2 and the accelerometer (z direction) with the Unstructured TAR method . . . 131
5.31 Coherences from inputs in group 3 and the microphone with the Unstructured TAR method . . . 132
5.32 Coherences from all inputs in group 3 and the accelerometer (z direction) with the Unstructured TAR method . . . 132
5.33 Coherences from inputs in group 4 and the microphone with the Unstructured TAR method . . . 132
5.34 Coherences from all inputs in group 4 and the accelerometer (z direction) with the Unstructured TAR method . . . 133

B.1 Ejemplo de evento catastrófico: turbina eólica rota. . . . 146
B.2 Distribución de la demanda de energía eléctrica dividida por sectores, [3]. . 153

List of Tables

1.1 Levels in damage detection. 3

2.1 Location and direction of different channels. 21
2.2 Definition of the damages. 22
2.3 Overview of the experiments and experimental details for the wind turbine tower. 23
2.4 Definition of the damages (tower with jacket). 25
2.5 Baseline phase – Damage detection estimation details (tower without jacket). 26
2.6 False alarm and missed damage rate using all available sensors and the sum of all of them. 31
2.7 Summary of the damage detection and identification results (tower with jacket). 33
2.8 Baseline phase – Damage detection estimation details (tower with jacket). . 36
2.9 Baseline phase – Damage identification estimation details (tower with jacket), learning with data record from D1 37
2.10 Baseline phase – Damage identification estimation details (tower with jacket), learning with data record from D2 38
2.11 Baseline phase – Damage identification estimation details (tower with jacket), learning with data record from D3 39
2.12 Baseline phase – Damage identification estimation details (tower with jacket), learning with data record from D4 40

3.1 Overview of the experiments and experimental details. 54
3.2 Parameters used for the non-parametric and parametric methods. 57
3.3 Summary of the damage detection results (inspection data records only). . 62

4.1 Description of the considered damage locations. 76

4.2 Numbers of experiments and vibration response signal details. 78
4.3 Damage detection and localization estimation details. 80

B.1 Niveles de detección de daño. 147

Chapter 1

Introduction

Time series appear everywhere in real life applications. The present work is devoted to the analysis of several time series methodologies. In particular the thesis is mainly focused in two fields:

- *Structural Health Monitoring*: parametric and non–parametric methods are used for damage detection (Chapter 2), also in the case of varying environmental conditions (Chapter 3), and additionally localization is also assessed (Chapter 4). For this application only stationary signals are considered. The chosen structures in which the methods are tested are related to the wind turbine field. In particular lab–scale towers (Chapter 2) and blades (Chapters 3 and 4) have been used.

- Analysis of *non–stationary signals*, using several techniques (parametric and non–parametric) and application of these techniques to obtain *coherences* (Chapter 5). Some numerical, laboratory and real applications of the methodologies are presented. The laboratory experiences are first simulated numerically and then mimicked in a semi–anechoic chamber. Finally a real application, specifically a real elevator system, is analyzed.

The rest of this chapter is organized as follows: sections 1.1 and 1.2 introduce and summarize the state of the art of structural health monitoring and the non–stationary analysis (including coherence computations) respectively, whereas section 1.3 presents the organization of the rest of the document including the objectives and contributions from each chapter.

1.1 Structural Health Monitoring

Structural Health Monitoring (SHM) is defined as the process of acquiring and analyzing data from on–board sensors to evaluate the health of a structure. The main characteristic inherent to any SHM system is that sensors have to be integrated, embedded or permanently attached to the structure, leading to the main advantage of SHM compared to Non–Destructive Testing (NDT): the inspection process can be automated, without disassembly. This allows the structure to be continuously monitored including processing abilities inside the structure, whereas NDT is usually performed periodically or on demand. Thus SHM provides large savings in expected maintenance costs (for aircraft, bridges and other infrastructures).

According to [7] SHM aims to give, at every moment during the life of a structure, a diagnosis of the "state" of the constituent materials, of the different parts, and of the full assembly of these parts constituting the structure as a whole. The state of the structure must remain in the domain specified in the design, although this can be altered by normal aging due to usage, by the action of the environment, and by accidental events. Damages in structures have caused many disasters in the course of history as can be seen in Figure 1.1. This has attracted the attention of the community related to construction techniques and maintenance of structures, such as bridges [108].

Figure 1.1: Example of catastrophic event: broken wind turbine.

According to [14] SHM is the integration of sensing and possibly also actuation devices to allow the loading and damaging conditions of a structure to be recorded, analyzed, localized, and predicted in a way that nondestructive testing (NDT) becomes an integral part of the structure and a material.

In view of the previous definitions it becomes evident that SHM involves *damage* detection, but what is understood by damage? According to [35] in the most general

terms, *damage* can be defined as changes introduced into a system that adversely affect its current or future performance. Implicit in this definition is the concept that damage is not meaningful without a comparison between two different states of the system, one of which is assumed to represent the initial, and often undamaged, state.

1.1.1 Levels in damage diagnosis

According to Rytter [93] four levels of damage can be distinguished in Structural Health Monitoring, these are shown in Table 1.1.

Level	*Description*
1	Determination of the existence of structural damage
2	Level 1 plus identification/localization of the damage
3	Level 2 plus quantification of the injury
4	Level 3 plus prediction of the remaining life (prognosis)

Table 1.1: Levels in damage detection.

The first level deals with the detection of the damage (analyze the presence or absence of structural damage). The second level also involves the identification (type of damage) and localization of the detected damage. In the third level, besides the identification and localization of the damage, its extent, magnitude or severity is assessed, while the fourth level additionally predicts the remaining life of the damaged structure.

Most of existing works are focused on levels 1 to 3, the fourth level involves in general a deeper knowledge and physical insight of the structure under study, so it has received less attention in the literature as it is the most complicated to accomplish. In the scope of the present work only the first two levels will be addressed.

1.1.2 Damage detection – Level 1

Traditional damage detection methods are based on ultrasound, acoustic, eddy currents or thermal field principles [27]. The main problem is that they require access to a vicinity of the potentially damaged area, so information regarding the possible location of the damage needs to be known a priori, which is not always possible. In general these techniques have been validated through simple beam or plate type structures rather than real structures. Moreover, most of them are expensive and time consuming.

An alternative approach that tries to overcome these difficulties are *vibration based methods* [37].

Vibration based methods

Vibration based Structural Health Monitoring (SHM) methods form a technologically important family. The main idea of these methods is that small variations in a structure cause changes in the vibrational response which can be detected. Some of the vibrational methods are based on natural frequencies [52, 71], others on modal shapes [5, 73] or on modal strain energy [64]. Worden *et al* [109] developed a method using outlier analysis for damage detection. Principal Component Analysis (PCA) was used in [21] for the detection and localization of structural damage. A novel analysis method based on the Kalman model was recently proposed in [113].

They offer a number of advantages, mainly in that they require no visual inspection, are global (in the sense of covering large areas with a few sensors), capable of working at a system level, can be potentially used under ambient excitation, can be automated and also tend to be time and cost effective [95, 27, 91].

In this subclass further classifications can be made:

- *Parametric* versus *non–parametric* methods.
- *Response–only* versus *excitation–response* methods.
- *Supervised* versus *unsupervised* methods (referring to the fact of using or not damaged data records in the learning/baseline phase).
- *Scalar* (univariate) versus *vector* (multivariate) methods.
- Etc.

In the scope of this work mainly the first three classifications will be considered, presenting different methods covering the different options. In all chapters involving damage diagnosis only scalar methods will be used. It is also worth mentioning that for damage diagnosis only the time–invariant dynamics (under stationary conditions) of the structures will be considered.

Non–parametric vibration–based methods for SHM are based, for example, on power spectral estimates [37, 72], or on frequency response functions [90]. Parametric methods are based on corresponding time series representations. One example widely used is the

AutoRegressive model [77, 61], which will characterize the data in the healthy state. The damage will be detected by comparing a characteristic feature in an unknown state with the corresponding one in the healthy state. These types of method have received considerable attention in the literature [37, 82]. A more general case using AutoRegressive Moving Average (ARMA) models or AR with eXogenous inputs (ARX) is analyzed in [101] and [76]. A method based on subspace identification and state space model residuals is reported in [9].

Statistical time series SHM methods form an important class within the context of vibration based SHM methods. Their main three elements are:

i) Random excitation and/or vibration response signals.

ii) Statistical model building.

iii) Statistical decision making for inferring the health state of the structure.

These methods involve two different phases: in an initial *baseline* (*training* or *learning*) phase, the methods employ random vibration and/or excitation response signals obtained from the structure under its healthy state (sometimes also from some potential damage scenarios) and obtain a non–parametric or parametric statistical model describing the structure in the considered state. A *characteristic quantity* is then extracted to characterize the structure in this, in general healthy, state. In the *inspection phase* given a new measured time series (in an unknown state) the method uses statistical decision making to decide whether the structure is currently damaged or undamaged. In some cases also an identification/localization of the damage may be achieved. Another advantage of this type of methods is that they inherently account for certain uncertainties as they use statistical tools.

Vibration based methods can be data–based [33, 9] or physics–based methods, based in general, on finite element models, [27]. In the context of the present work only data–based methods will be considered. This is an advantage for many applications, since a model will not always be available and furthermore, even in cases where a model is available, it may be computationally expensive. An extra advantage is that they are easily generalized in different contexts and structures, due to the fact that only response signals (and maybe also the excitation signals) are used.

1.1.3 Damage localization – Level 2

Damage localization corresponds to level 2 in the previously described Table 1.1.

In the context of vibration based methods, damage localization has been tackled in general through complex and detailed models (typically Finite Element Models) using current vibration signals and model updating procedures. The need of a detailed model may be a drawback for some applications. In addition, damages considered need to be simulated in the models and some parameters identified to be updated with the current vibration measurements [98, 59]. In practice such a procedure typically requires large FEMs and several vibration sensors for proper model updating [10, 22]. In these cases damage is localized within a particular finite element.

Within the context of data–based approaches the damage localization subproblem has been tackled as a classification problem where the structure is divided into a number of regions or elements and damage is localized to any one of them [67, 111]. In [94] the problem of *precise* damage localization is considered, in the sense that the full topology is considered and the specific coordinates are estimated through a novel Functional Model Based Method (FMBM) (which may also be used for damage quantification or accounting for varying environmental conditions).

1.1.4 Accounting for varying environmental and operational conditions (EOC)

An important limitation of vibration–based methods is that changes in the dynamics may be also caused by varying environmental conditions and uncertainty, thus potentially limiting the performance characteristics and reliability of damage diagnosis [62]. This is also true for typical statistical methods, which although accounting for certain types of uncertainty, they still fail to account for environmental conditions and uncertainties not employed during their training (baseline) phase.

The problem of effectively coping with varying environmental conditions and uncertainty is thus important, and a current technology application barrier. The general approach for overcoming it involves, in broad terms, proper "pre–processing" of the raw vibration data records or of the selected characteristic quantity (feature vector), aiming at the "removal" of the effects of uncertainty. Such pre–processing may be distinguished into *model–based* or *non–model based*, and is also referred to as "data normalization" (see [99] for an overview).

In the first class of methods (model–based), environmental conditions and uncertainty are assumed to be *measurable*, so that their effects on the dynamics may be properly quantified and modelled, resulting into their potential separation from those of damage.

This may be achieved through *multi–model* methods, in which an individual model is obtained for each specific condition, and then these are properly linked together. Such methods establish relationships among modal parameters (such as eigenfrequencies) and environmental effects (such as temperature) by means of regression or interpolation techniques [110], correction formulae [63], ARX models [85], or linear filters [100]. Clustering for different environmental conditions is also used [70], while global functional models (referred to as Functionally Pooled models) capable of describing the effects of measurable environmental conditions on the dynamics are employed in [56]. The main limitation of these methods stems from the fact that uncertainties are *not* always measurable, in which case they cannot be properly accounted for.

The second class of methods (non–model based) is based on proper manipulation ("pre–processing" or transformation) of the selected characteristic quantity (feature vector) so that its transformed version remains sensitive to damage but insensitive to changes in the environmental conditions and uncertainty. These methods are often simpler than their model–based counterparts, and do not require measurable uncertainties. They include Principal Component Analysis (PCA) based methods [40, 114, 45, 11] which transform (project) an original feature vector into an orthogonal space in which the most prominent elements expressing variability under healthy conditions are removed (as being related to environmental conditions and other uncertainties), while the least prominent elements are retained as they are expected to be affected by damage. Of course, this cannot be generally guaranteed, and as reported in [40], the approach may not always achieve high performance.

Similar in philosophy techniques include Kernel Principal Component Analysis, which is a non–linear variant of the PCA [75, 83], factor analysis [25] which attempts to identify a linear subspace in which the environmental effects lie and then project the measured signals in its orthogonal subspace, averaging techniques [8] based on the null–space method in which an averaged sample Hankel matrix accounting for various conditions is used, cointegration [19] which attempts to find and eliminate common trends in the healthy and damaged vibration signals that may be caused by environmental or operational uncertainties, a negative selection approach that uses an analogy with the immune system [105], and a method employing a large array of sensors and spatial filters for obtaining a characteristic quantity capable of differentiating between damage and environmental changes [24]. Typically only healthy data records are used in the training phase of these methods (the case of *unsupervised learning*) which may result in limitations in their effectiveness, while for certain methods a large number of sensors may be also necessary.

1.1.5 Application in the wind turbine field

Damage diagnosis on wind turbine structures is of obvious practical and economic importance. Especially as the structures, including the blades, are increasing in size in an effort to capture as much wind power as possible. The need to continuously monitor the health state of these structures is thus evident as visual inspection is not an effective and viable option. Furthermore, the current trend in this field is to locate the wind power plants offshore, [15]. One advantage of this change in location is that the wind is stronger off the coasts, and unlike wind over the continent, offshore breezes can be strong in the afternoon, matching the time when people are using the most electricity, see Figure 1.2. An extra advantage, depending on their location, is that the visual pollution is no longer an issue. Offshore turbines can also be located close to power–hungry populations along the coasts, eliminating the need for new overland transmission lines. However, offshore plants have some drawbacks, [29, 16]:

- Usual onshore difficulties need to be accounted for, these include high towers or great forces generated at the edge of the blade.
- Requirements of long life of the structure and a minimum percentage of time out of service.
- Costs, including maintenance and operations, increase significantly compared to onshore ones.
- The demanding conditions of the marine environment have to be taken into account.

These drawbacks have increased the level of interest in the implementation of different concepts of SHM in these structures [17].

In this field, accounting for varying environmental and operating conditions, is crucial. For wind turbines the varying conditions may be due to weather (temperature, humidity), wind speed, varying rotational speed, and so forth, and they may lead to poor detection performance if not properly accounted for.

Among the different parts of wind turbines, the tower has received limited attention in the literature [54, 23], specially when compared to other parts such as the blades. In [13] strain sensors are used to for crack detection in tower, with the most promising strategy using the strain difference between adjacent strain sensors as an index of the presence of a crack. The main problem is the number of sensors to be installed.

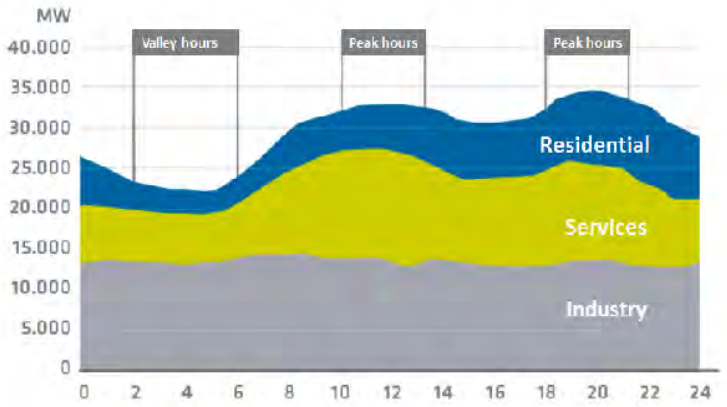

Figure 1.2: Distribution of electricity demand divided by sectors, [3].

It is clear that wind turbine blades are subject to damage, and this may even lead to tower damage as well [74, 44]. Previous studies [41] have focused on changes in modal frequencies under different damage scenarios for a laboratory scale wind turbine blade, reaching the conclusion that the first seven modes may be sufficient to indicate damage. Yet no actual damage detection is performed.

In another study [92], fatigue tests on full size blades are performed, using the results to validate a variety of damage Structural Health Monitoring methods, such as acoustic emission, impedance based methods, or wave propagation based methods. In [74] a 1–meter–long section of a wind turbine blade is analyzed via different methods: Lamb wave propagation, frequency response analysis, and statistical time series type methods. The damage is simulated by adding a piece of putty on the surface. For all methods, the damage index (characteristic quantity) used has been obtained from cross–correlations between a baseline signal and a corresponding signal from the current (in unknown state) structure, under slightly varying conditions (position of the blade section on the table). The differences due to damage in this case are larger than those due to the considered variations, and detection is performed by comparing to a single "healthy" baseline case, with good overall results.

In [28] a simulation and an experiment are presented in which damage localization is performed using wavelets. In the experimental case, a 1.74 m length blade is used, and damage is simulated by adding a mass on the surface (2 to 12% of the total mass). The blade is excited via an electromechanical shaker, and a laser Doppler vibrometer is used for obtaining the mode shapes. The differences between the healthy and current continuous wavelet transform coefficients are computed and used for damage localization.

In [107] mode shapes are also employed, presently with 2D wavelets being used for damage detection, localization, and assessment in a simulated 41.2 m long wind turbine blade. The main limitation of the method seems to be the large amount of measurement points required.

1.2 Non–stationary analysis: multiple coherence computations

In many industrial applications non–stationary signals are present, and its analysis taking into account this non–stationarity is of paramount importance [42]. Some examples appear in transient events such as an emergency stop or when starting an engine. Another examples include bridges with crossing vehicles, wind turbines [6], aircraft systems and many more. Another important case comes up when a source of noise is moving with respect to the receptor, [32], or viceversa, this is the case of pass–by noise, or the noise received in an elevator cabin. In this last case the signal measured at the receptor point may be non–stationary even if the emitted signal was stationary (for example in amplitude, but also its frequency content, due to the Doppler effect). Time–frequency representations are necessary to understand the frequency content of the signals and how it varies with time.

1.2.1 Classification of time–frequency methods

Methods handling time varying signals may be classified into parametric or non–parametric depending on the type of model adopted. Among the non–parametric, which have been the more widely used in the literature, some examples are the Short Time Fourier Transform [18], the Wigner–Ville distribution [55] or wavelet analysis [103]. Parametric models such as Time dependent ARMA [89] or state space models [65], belong to the second class, which has, in general, received less attention.

In the present work three particular methods will be presented and compared. A pure non–parametric approach, a second one parametric in frequency and non parametric in time and a third one parametric both in time and in frequency.

The main idea of the first two methods considered in the scope of this work is to divide the signal into short time blocks, so as to capture the time dependency (non–parametric in time). Then the signal will be restricted to each block and the restriction will be considered

stationary. For each stationary block a classic technique for stationary signals is applied. The more conventional procedures are based on techniques which use the Fast Fourier Transform (FFT), and are thus non–parametric (in frequency). The application of this technique to short time block is known as Short Time Fourier Transform (STFT). They are extremely attractive due to their computational efficiency and their easy implementation. Nevertheless, the spectral estimators obtained have a high variability. Some work has been done to overcome this high–variance problem [112], by applying several windows to the same signal and averaging the results but the estimator has a reduced time and frequency resolution. To overcome some of the difficulties which appear in FFT–based methods (high variance/poor resolution) a model–based or parametric method may be applied to each block. This gives rise to a method which is non–parametric in time and parametric in frequency. Within the field of parametric estimation, the most popular models include autoregressive moving average methods [61, 87] (known as ARMA methods). These last methods offer a better spectral resolution compared to the one provided by methods based on the FFT, although they also involve a higher computational cost. In this case a time dependent ARMA (TARMA) representation with unstructured variation of the parameters is obtained (in each block, the parameters are computed independently). In the FFT based method increasing the time resolution, by reducing the size of the blocks, results in a drop in spectral resolution. In the case of the ARMA methods, a reduction in the size of the block reduces the statistical efficiency and the numerical reliability of the estimation method, obtaining a less accurate model. However in the last method, the model may provide a, probably erroneous, spectral representation of infinite frequency resolution.

In order to handle the time dependency in a more natural way and to decrease the number of involved parameters, a TARMA model with a deterministic parameter evolution [50], can be considered. This means that the parameters will evolve in a structured form, represented by functions belonging to specific functional spaces [102]. This is a more elaborated method, known as FS–TARMA method. The basis of these spaces should be selected according to the characteristics of the signal under study, since this will predetermine the type of behavior that can be captured. If the signal presents fast transitions, then piecewise constant functions would be more suitable, as suggested in [53], otherwise smooth time dependency will be obtained by using polynomials or trigonometric functions. In this process also the variance needs to be estimated. An approximation of the variance using high order polynomials might lead to a non–positive approximation due to the Runge phenomenon (see [104], p. 186). To avoid a non–positive variance, Bernstein

polynomials [78] are proposed for this approximation leading to a non–negative approximation which is of crucial importance in coherence computations, as will be shown later. An advantage of the FS–TARMA method with respect to the unstructured one is the low number of parameters present in the model. It must be noted that the calculation of these parameters is expensive, since they must be obtained all at once unlike in the unstructured case, where for each block the parameters can be obtained in an independent way. These kind of methods have been used in [31] to identify vehicle signatures using the coefficients of this model, or in [32] to dereverberate a signal coming from a moving speaker. In both applications the time varying dynamics comes from a moving noise source (vehicle/speaker).

For many purposes it will be necessary to deal with more than one signal. An important example is the case of coherence calculation between signals. Coherence calculation is widely used in electroencephalogram (EEG) signals [66, 81] and in the automotive industry [86, 96]. It allows to obtain the degree of contribution of a particular noise source to the total noise received at some point. In this case multivariate models need to be considered, in which all the signals are treated together. Previous works like [116] have already introduced a similar concept of coherence based in FS–TAR models to be used in biomedical applications. For coherence computations, the high variance present in the STFT method, reduces the statistical significance of the estimators obtained, [116].

1.2.2 Application in the elevator field

Comfort in an elevator [57] basically depends on variables such as the the *vibration* during the travel as well as the *noise* received in the cabin. There are some reference measurements that can give an idea of the quality of the travel and also of the current state of the installation (helping maintenance operations) [30]. The noise received in the cabin may be transmitted through the structure (that means generated by the vibration of the structure) also known as *structure–borne* noise, or it can be transmitted through the air, also known as *air–borne* noise [43].

In this work, the objective is to identify the main contributions to both the vibration and the noise received in the elevator cabin during a travel. To achieve this, measurement of different possible sources of noise and vibration were recorded, as well as the noise and vibration perceived in the elevator cabin.

1.3 Thesis goals and organization of chapters

The topics covered in the present thesis together with the objectives and contributions are included in this section. These are presented chapter by chapter:

- Chapter 2 presents an implementation of a level 1 algorithm together with a possible extension to a level 2 algorithm. The methodology is applied in a lab–scale offshore wind turbine tower in two versions, with and without jacket. The method used is an example of vibration–based parametric method (AR model) that makes use of statistical analysis using only output measurements from the structure. The specific objectives and contributions are:

  1. A parametric vibration–based damage detection methodology is used in a lab–scale wind turbine tower.
  2. Even with only one sensor accurate detection results are obtained.
  3. Analysis of the different directions and locations of measurement is performed.
  4. A global approach adding the damage indicators of all the channels is also proposed.
  5. Based on a supervised learning process, identification of the damage is achieved.

- Chapter 3 proposes a novel non–model based supervised PCA based methodology for damage detection under varying environmental conditions. The suggested methodology, in three different forms, is validated in a lab–scale wind turbine blade with temperature and humidity variations. The specific objectives and contributions are:

  1. Development of a supervised statistical, non–model based, PCA–type methodology for damage detection.
  2. Achievement of high damage detection performance under environmental effects and uncertainty through improved learning that involves the use of data records obtained under healthy *and* various damage scenarios (supervised learning).
  3. Validation of the methodology on a lab–scale wind turbine blade.
  4. Comparison of the different implementations (incarnations) of the methodology: only output and input–output, parametric and non–parametric.
  5. Operating with a low number of sensors (even a single sensor).

6. Operating within a limited and low frequency bandwidth.

- Chapter 4 deals with the problem of damage diagnosis in a lab–scale wind turbine blade. An FRF methodology is used for damage detection and an FP–ARX method is proposed for the precise localization of the damage, considering the blade as one–dimensional. The specific objectives and contributions are:

  1. Examination of the feasibility of damage diagnosis (detection and localization) on a lab–scale wind turbine blade.
  2. Use of a single pair of force excitation and vibration acceleration response signals.
  3. Use of a limited and low frequency bandwidth.

- Chapter 5 considers different non–stationary laboratory and real applications in the context of multiple coherence computations for the identification of predominant sources of noise. Three approaches are presented and compared in different situations: univariate analysis, simple two inputs and one output example and a complex real system. The specific objectives and contributions are:

  1. Definition of multiple coherence for non–stationary signals employing non–parametric, semi–parametric and parametric methods.
  2. Introduction of Bernstein polynomials for the approximation of the variance to ensure positiveness/positive definiteness of its approximated versions.
  3. Application of the multiple coherence method in numerical and laboratory applications.
  4. Analysis of a real elevator case with a very high number of measured sources, trying to identify the predominant sources and paths for different considered outputs studying the effect of air–borne and structure–borne contributions.

- Chapter 6 finally summarizes the conclusions and presents the future work.

Chapter 2

Damage detection via parametric methods: application to a lab–scale wind turbine off–shore tower

2.1 Introduction

In this chapter an implementation of a level 1 algorithm is presented together with a possible extension to a level 2 algorithm. The methodology will be applied in a tower similar to the one of an offshore wind turbine in two versions, with and without jacket. The method used is an example of vibration–based parametric method (AutoRegressive model) that makes use of statistical analysis using only output measurements from the structure. In a previous work [117], the tower with jacket structure has been tested by the author and some collaborators, and a comparison between this AutoRegressive technique and a NullSpace based one was presented.

The rest of the chapter is organized as follows: in section 2.2 the AutoRegressive modeling of the signals involved is presented, in section 2.3 the methodology used for damage detection and identification will be described, in section 2.4 the experimental setup for each case is presented. Section 2.5 is devoted to the presentation of the obtained results. Finally section 2.6 the conclusions and future work are described.

2.2 Autoregressive (AR) model of the involved signals

Let $\{x[n]\}_{n=1}^{N}$ be a time series. In an autoregressive model the signal is approximated by the linear difference equation with real coefficients given by:

$$x[n] = u[n] - \sum_{k=1}^{p} a[k]x[n-k], \tag{2.1}$$

where $x[n]$ is the output sequence of a filter (of order p) which models the observed data, and $u[n]$ is the conducting noise, which will be supposed to be a white noise with zero mean and variance σ_u^2. $\boldsymbol{\theta}$ will denote the vector of p parameters:

$$\boldsymbol{\theta} = \begin{bmatrix} a[1] \\ \vdots \\ a[p] \end{bmatrix}. \tag{2.2}$$

To obtain the coefficients $a[k]$, with $k = 1, \ldots, p$ and the variance of the white noise σ_u^2 from a finite series of data the so called Yule–Walker equations must be solved, which are just a linear system, see [60]. In principle $O(p^3)$ operations would be needed to solve it, but its particular structure allows us to solve it in $O(p^2)$ operations by the Levinson algorithm. Note that this order p will be related to the length of the signal, but will not be higher than half this length and in general will be much lower.

The selection of this order is not an easy task and it is a critical aspect for building an appropriate model. The optimum filter order is not known a priori, which is why in practice, various orders need to be postulated. In [61], the authors outline different criteria for selecting this order. Some examples of error criteria are the Final Prediction Error (FPE) or the Bayesian Information Criterion (BIC). What is done is to postulate a minimum and a maximum order between which the optimal order must be. After this, all the intermediate models are obtained and the value of the corresponding error is calculated. Finally the order is chosen as the one that minimizes the selected error criterion.

2.3 The damage detection method

The damage detection will be performed by comparing a parametric feature of the structure in an unknown state with the corresponding one in the healthy state. The method used in this chapter is an algorithm of level 1, based on autoregressive methods, [37].

The method consists of two different steps. In the first one, known as *learning phase*, the behaviour of the structure in the healthy state will be modeled, as it will be described later. After that, in the *inspection phase* given a new data record in an unknown state, the method will determine if it has any failure or not by using statistical hypothesis testing. Let's detail how both phases of the method work.

2.3.1 Learning phase

Given one representative data record from the healthy structure, an AR model is built of the form in Equation (2.1) to characterize it, namely:

$$x_{ref}[n] = u_{ref}[n] - \sum_{k=1}^{p} a_{ref}[k] x_{ref}[n-k], \tag{2.3}$$

where $u_{ref}[n]$ is a white noise with variance σ^2_{ref}. When estimating the vector of parameters in the reference state, θ_{ref}, the variance matrix, P_{ref}, of this estimation is also computed, see Ljung, [77]. In this step the model order needs to be chosen for the time series given.

2.3.2 Inspection phase

Damage detection will be based on testing for statistically significant changes in the parameter vector θ_{ref}.

Given a new data record corresponding to an unknown state, an analogous model to the reference one is built:

$$x_{new}[n] = u_{new}[n] - \sum_{k=1}^{p} a_{new}[k] x_{new}[n-k], \tag{2.4}$$

with a new vector of parameters θ_{new}, being $u_{new}[n]$ a white noise with variance σ^2_{new}. Note that in this step the model order obtained in the previous step is used.

The statistical hypothesis test used is then, see [68]:

$$\begin{aligned} H_o: &\quad \delta\theta = 0 \qquad \text{(null hypothesis – healthy structure)} \\ H_1: &\quad \delta\theta \neq 0 \quad \text{(alternative hypothesis – damaged structure)}, \end{aligned} \tag{2.5}$$

where $\delta\theta = \theta_{ref} - \theta_{new}$ is the difference between the new parameters obtained and the reference ones. The estimation of this difference follows a normal distribution with the following mean and variance:

$$\delta\widehat{\theta} = \widehat{\theta}_{ref} - \widehat{\theta}_{new} \sim N(\delta\theta, \delta P), \tag{2.6}$$

with $\delta P = P_{ref} + P_{new}$. Under the null hypothesis:

$$\delta\widehat{\theta} = \widehat{\theta}_{ref} - \widehat{\theta}_{new} \sim N(0, 2P_{ref}) \tag{2.7}$$

and the quantity

$$D = \delta\theta^T \left(2P_{ref}\right)^{-1} \delta\theta, \tag{2.8}$$

follows a χ^2 distribution with $d = p$ degrees of freedom. By using the estimated version of the covariance matrix, $\widehat{P}_{ref}$, the following test is constructed, see Figure 2.1:

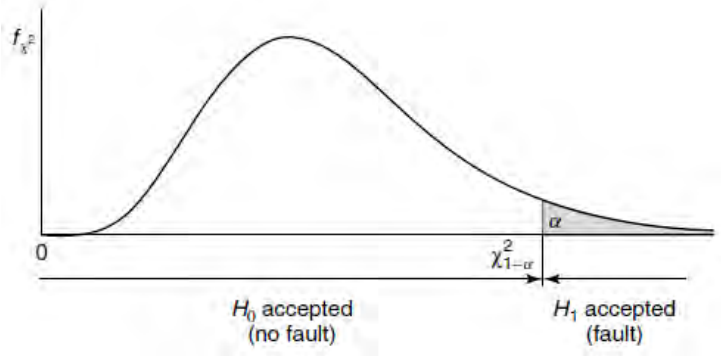

Figure 2.1: Statistical hypothesis testing based on a χ^2- distributed statistic (one–sided test).

$$D \leq \chi^2_{1-\alpha}(d) \quad \Rightarrow \quad H_0 \text{ is accepted} \tag{2.9}$$

$$\text{Else} \quad \Rightarrow \quad H_1 \text{ is accepted}, \tag{2.10}$$

where α is the chosen (type I) risk level for the test, and $\chi^2_{1-\alpha}(d)$ is the $\chi^2(d)$ distribution's $1-\alpha$ critical point.

2.3.3 Application notes

It is important to notice that the methodology here presented refers to just one data record, i.e. the healthy state is supposed to be characterized with the signal measured in just one point. As will be shown in the next section, the laboratory towers tested will have different points of measurement, and in some of them more than one direction, which makes several channels of measurement.

To deal with the different channels of monitoring two alternatives could be used. The first one consists of analyzing with the previously described method each channel in an independent way. This is the option selected for this work. It has to be taken into account that with this technique it is possible that not all the damages are detected by all the channels. As a conservative approach, it may be said that there is damage if at least one channel indicates it, but in this case too many false alarms may appear. Another alternative is to sum all the metrics for each channel and all the thresholds and say that there is damage if the sum of the metrics is greater than the sum of the thresholds, this alternative will also be analyzed.

A second option corresponds to considering all the signals as a group. In this way multivariate autoregressive models can be built taking into account all the signals at a time. This could be analyzed in a future work, analyzing the distribution followed by the matrix of parameters appearing in this approach.

2.3.4 Extension to a level 2 algorithm

In a laboratory test like those that will be presented, where all the damages are a priori known, it is possible to extend the methodology described to a level 2 algorithm. For the damage identification it will be enough to perform the same learning process but now with a characteristic signal of that specific damage state, instead of using a healthy signal. In this case, in the detection phase, the fact that the new unknown state stays below the threshold will indicate the presence of that specific damage, instead of indicating a healthy state of the structure.

2.4 Experimental set–up

Two different structures have been considered for the assessment of the techniques, a tower similar to a wind turbine and the same tower adding a jacket to simulate an offshore wind

turbine.

2.4.1 Tower for damage detection

The tested structure is a tower model, similar to those of a wind turbine, see Figure 2.2(a). This structure is 2.2 m high; the top piece is 1 m long and 0.1 m width. The tower is composed of three sections joined with bolts. Each joint has four connecting bolts. The damage is simulated by acting on these bolted joints.

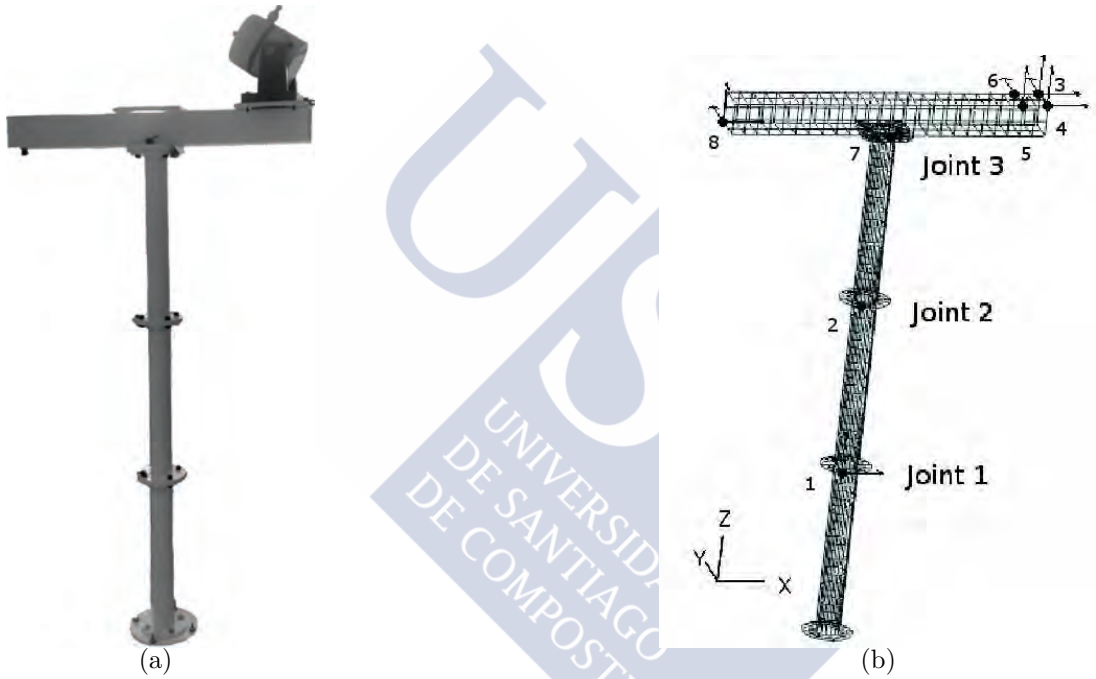

(a) (b)

Figure 2.2: (a) Tower photo and (b) Sensor enumeration and location.

As it can be seen in Figure 2.2(a) there is a modal shaker placed on top of the structure, simulating the weight of the nacelle of a wind turbine, so that it can create a vibrational movement. To detect the structural response, some accelerometers are placed in the tower. In order to know the best location for these sensors, FemTools (by Dynamic Design Solutions) has been used. The pretest analysis made to the Finite Element model of the tower, resulted in 8 accelerometers, 4 triaxial, and 4 uniaxial, see Figure 2.2(b). In Table 2.1 the location and measurement direction from all sensors and channels is indicated.

The optimal sensor location was found using the Sensor Elimination Algorithm by the Modal Assurance Criterion (SEAMAC) method implemented in FemTools, see [115]. The

Sensor	*Location*	*Channel*	*Direction*
1	Joint 1	1	$x+$
		2	$y+$
		3	$z+$
2	Joint 2	4	$y+$
3	Right corner	5	$x-$
		6	$y-$
		7	$z+$
4	Right corner	8	$x-$
		9	$y-$
		10	$z+$
5	Right corner	11	$z+$
6	Right corner	12	$y+$
7	Joint 3	13	$y+$
8	Left corner	14	$x-$
		15	$y+$
		16	$z-$

Table 2.1: Location and direction of different channels.

modal assurance criterion (MAC) is commonly used to compare mode shapes. Given a group of R mode shapes, $\{\Phi_i\}_{i=1}^{R}$ from the structure, a MAC matrix (of dimension $R \times R$) can be constructed. Each term in the MAC matrix measures the squared cosine of the angle between two mode shapes and is obtained as:

$$\mathrm{MAC}_{i,j} = \frac{\left(\Phi_i^t \Phi_j\right)^2}{\left(\Phi_i^t \Phi_i\right)\left(\Phi_j^t \Phi_j\right)}. \tag{2.11}$$

When $\mathrm{MAC}_{i,j} = 0$, the $i-$th and the $j-$th mode shapes are orthogonal to each other. Hence the mode shapes are linearly independent when all the off–diagonal terms in the MAC matrix are zero. The SEAMAC algorithm is a sensor elimination method algorithm, that attempts to find a measurement point configuration minimizing MAC values in the off–diagonal terms. The method is based on eliminating iteratively (and one by one) those degrees of freedom that show a lower impact on the MAC values. This iterative process stops when a default MAC matrix is reached (sum of all values on the off–diagonal terms non greater than a pre–specified value). There may also be some extern restrictions

related to the number of accelerometers available.

The structure is excited with a modal vibrator which excites the structure using a white noise. The vibration modes of the structure are important in order to know the behaviour of the structure, and how should the data be acquired. In this tower, an Operational Modal Analysis has been made in order to have a good quality Finite Element Model. In this case, the first 10 modes will be analyzed, which are located under 500 Hz. The data is acquired using an OROS OR36 system with an acquisition frequency of 1024 Hz (enough for capturing all first 10 modes), and 2 seconds long time series. In consequence, each data record consists of 2048×16 points.

First, the data acquired in the undamaged state is introduced in the algorithm implemented in Matlab. In this point, it learns and characterizes how the healthy structure behaves.

Subsequently different structural damages are introduced by acting on the bolted joints. There are four different bolted joints in each level of the tower. A total of nine different damages are created by loosening, respectively, one, two, or three connecting bolts (three damage severity levels) on each level of the tower. The damages considered are shown in table 2.2.

Damage name	*Description*
D1	One loosened bolt in joint 1
D2	Two loosened bolts in joint 1
D3	Three loosened bolts in joint 1
D4	One loosened bolt in joint 2
D5	Two loosened bolts in joint 2
D6	Three loosened bolts in joint 2
D7	One loosened bolt in joint 3
D8	Two loosened bolts in joint 3
D9	Three loosened bolts in joint 3

Table 2.2: Definition of the damages.

Several repetitions of each condition are considered, details can be found in Table 2.3.

All data records are acquired using the same type of excitation, the response of the accelerometers is stored. The algorithm provides the damage indicator values, representing the existence or absence of structural damage. The comparison of this metric with a

Health State	*Number of experiments*
Healthy	240
Damage 1	120
Damage 2	120
Damage 3	120
Damage 4	120
Damage 5	120
Damage 6	120
Damage 7	120
Damage 8	120
Damage 9	120
Sampling frequency $f_s = 1024$ Hz	
Signal bandwidth $3 - 500$ Hz	
Signal length $N = 2048$ samples (2 s)	

Table 2.3: Overview of the experiments and experimental details for the wind turbine tower.

threshold determines whether structural damage exists or not.

2.4.2 Tower with jacket for damage identification/location

The tested structure is a lab–scale tower, similar to those of an offshore wind turbine, see Figure 2.3(a). The top part corresponds to the presented in the previous section, but in this case a jacket is added,being now the structure 2.7 m high. The jacket is composed with several sections, all of them joined with bolts. The damage is simulated by acting on the bolted joints located in the jacket. There is a modal shaker placed on top of the structure, simulating the nacelle mass of a wind turbine, and it creates vibrational movements. The modal shaker excites the structure using a white noise.

As before, the data is acquired using an OROS OR36 system. The vibration modes of the structure are important in order to know the behavior of the structure, and how data should be acquired. In this tower, an Operational Modal Analysis has also been performed in order to have a good quality Finite Element Model. In this case, the first 10 modes will be analyzed, which are located under 100 Hz. For this reason the sampling frequency selected was of 256 Hz. To detect the structural response, some accelerometers

are placed in the tower. The best location for these sensors is found again using the sensor elimination by the modal assurance criterion (SEAMAC) pretest method implemented in FemTools. The analysis of the tower resulted in five triaxial accelerometers, two located in the jacket, one in the tower itself, and another two in the top part of the structure. These are shown in Figure 2.3(b). The duration of the data records is 15 seconds, so a time series consists of a matrix with 15 rows (one for each channel of measurement) and 3840 columns.

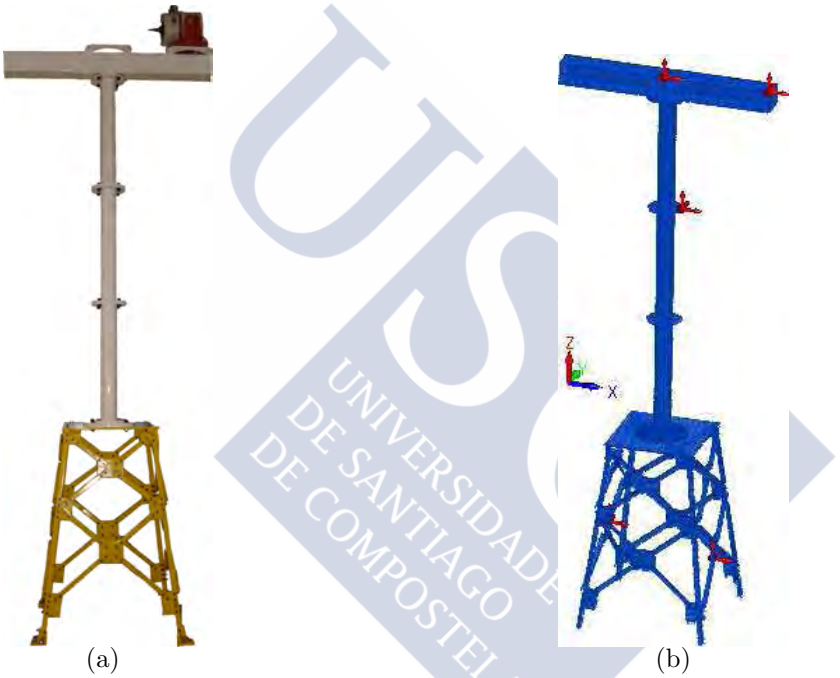

(a) (b)

Figure 2.3: (a) Tower with jacket photo and (b) sensor location.

The damages introduced are shown in Figure 2.4. Each bar located in the jacket structure is bolted using four bolts. The damages are introduced in two of the bars, with two different severities. The smallest damage is simulated by loosening two of those four bolts, and for the second one, four bolts are loosened (all of them). In Table 2.4 a description of the damages is shown.

For each state (healthy and all the damages) 16 data records are available. One of them will be used in the learning process, and the others will be used to test the algorithm.

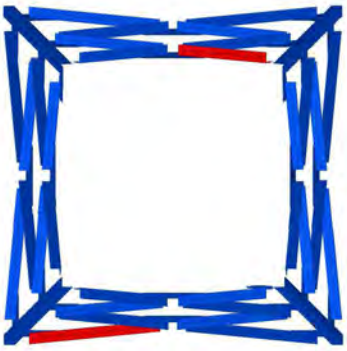

Figure 2.4: Damage location in the jacket.

Damage name	*Description*
D1	Two loosened bolts in the bar of the highest part of the jacket
D2	All loosened bolts in the bar of the highest part of the jacket
D3	Two loosened bolts in the bar of the lowest part of the jacket
D4	All loosened bolts in the bar of the lowest part of the jacket

Table 2.4: Definition of the damages (tower with jacket).

2.5 Results

In this section the results obtained will be presented and analyzed. First results corresponding to damage detection in the tower without jacket and after to damage identification for the tower with jacket.

2.5.1 Damage detection – Tower without jacket

Before presenting the results some details on the model identification will be presented.

Table 2.5 presents all the details of the models estimated for every channel. Figure 2.5 shows the validation of the model identified for the first channel. For the other 15 channels analogous checks were done to validate the identified model.

First of all, since an analysis channel by channel has been done, sixteen different Figures are shown, Figures 2.6(a)–(f), 2.7(a)–(f) and 2.8(a)–(d). An extra Figure corresponding to the sum of all channels and thresholds is included. For the sake of simplicity, even if a very big number of data records have been analyzed, in all Figures shown only three date records from each state are presented. So, the x axis represents the different

Channel	*Model Order*	*Condition number*	*Samples per parameter*
1	78	1.05×10^7	26.25
2	87	7.29×10^6	23.54
3	99	1.79×10^5	20.69
4	87	3.86×10^6	23.54
5	80	1.39×10^5	25.6
6	161	2.88×10^5	12.72
7	82	1.84×10^4	24.98
8	80	2.16×10^5	25.6
9	151	4.91×10^5	13.56
10	80	1.69×10^4	25.6
11	117	4.21×10^4	17.5
12	131	5.76×10^5	15.63
13	129	1.03×10^7	15.87
14	101	3.30×10^4	20.28
15	119	5.97×10^4	17.21
16	69	1.11×10^5	29.68

Table 2.5: Baseline phase – Damage detection estimation details (tower without jacket).

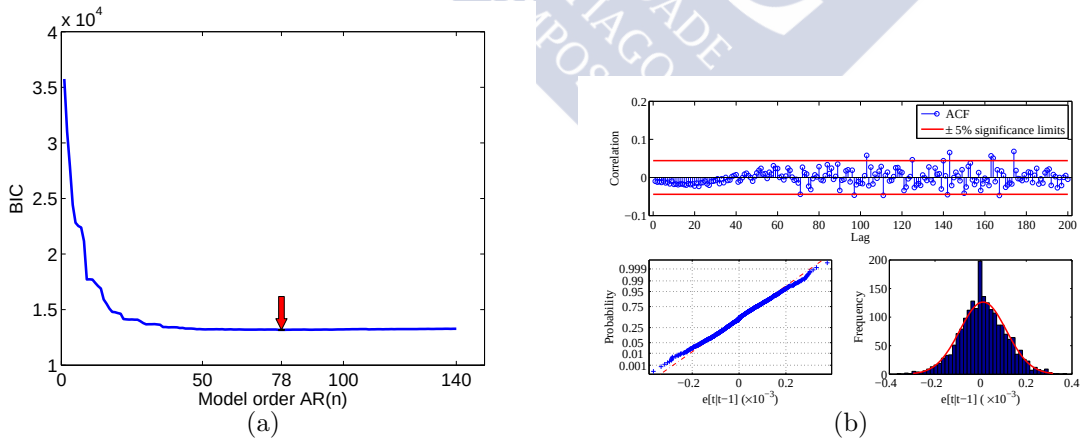

Figure 2.5: Baseline phase – parametric AR modeling of the healthy structural dynamics for channel 1: (a) BIC versus AR model order; (b) whiteness and Gaussianity tests on the model residuals.

data records, the first three correspond to the healthy condition, and then the nine types of damage are represented, they are labeled with the reference of the damage as indicated in the previous section. Healthy data records are plotted in white, all the cases where one bolt has been loosened (D1, D4 and D7) are presented in light gray, cases where two bolts have been loosened (D2, D5 and D8) are in darker gray and finally cases where three bolts have been loosened (D3, D6 and D9) are in black. For all Figures, the y axis represents the value of the metric given by Equation (2.8) that indicates structural damage, in a logarithmic scale. The black dashed line indicates the threshold considered, values above the line indicate the presence of damage. The threshold presented has been obtained for an α value of 10^{-3}.

It is observed that in general, the values for data records of the same type of damage are similar. Indeed, and as could be expected, the value of the metric increases as more bolts are loosened in the same joint.

The fist damage (D1, one loosened bolt in Joint 1) has some detectability problems, with values for the damage indicator very close to and even lower than the healthy ones. For this reason, in this case, perfect results (that would mean no false alarms and no undetected damages) cannot be obtained. In fact, increasing the value of the threshold one could reduce the number of false alarms, but this would imply increasing the number of missed damages. The value selected for the threshold (corresponding to $\alpha = 10^{-3}$) was selected trying to obtain reasonable results (not trying to reduce as possible false alarms at the cost of increasing the missed alarm rate significantly).

Figures just show an idea of how the behavior of the different channels is. But for full details, in Table 2.6 a summary of all the results (for all data records, detailed in Table 2.3) obtained is shown. There, false alarm and missed damage rate are presented for the analysis channel by channel and for the sum of channels and thresholds.

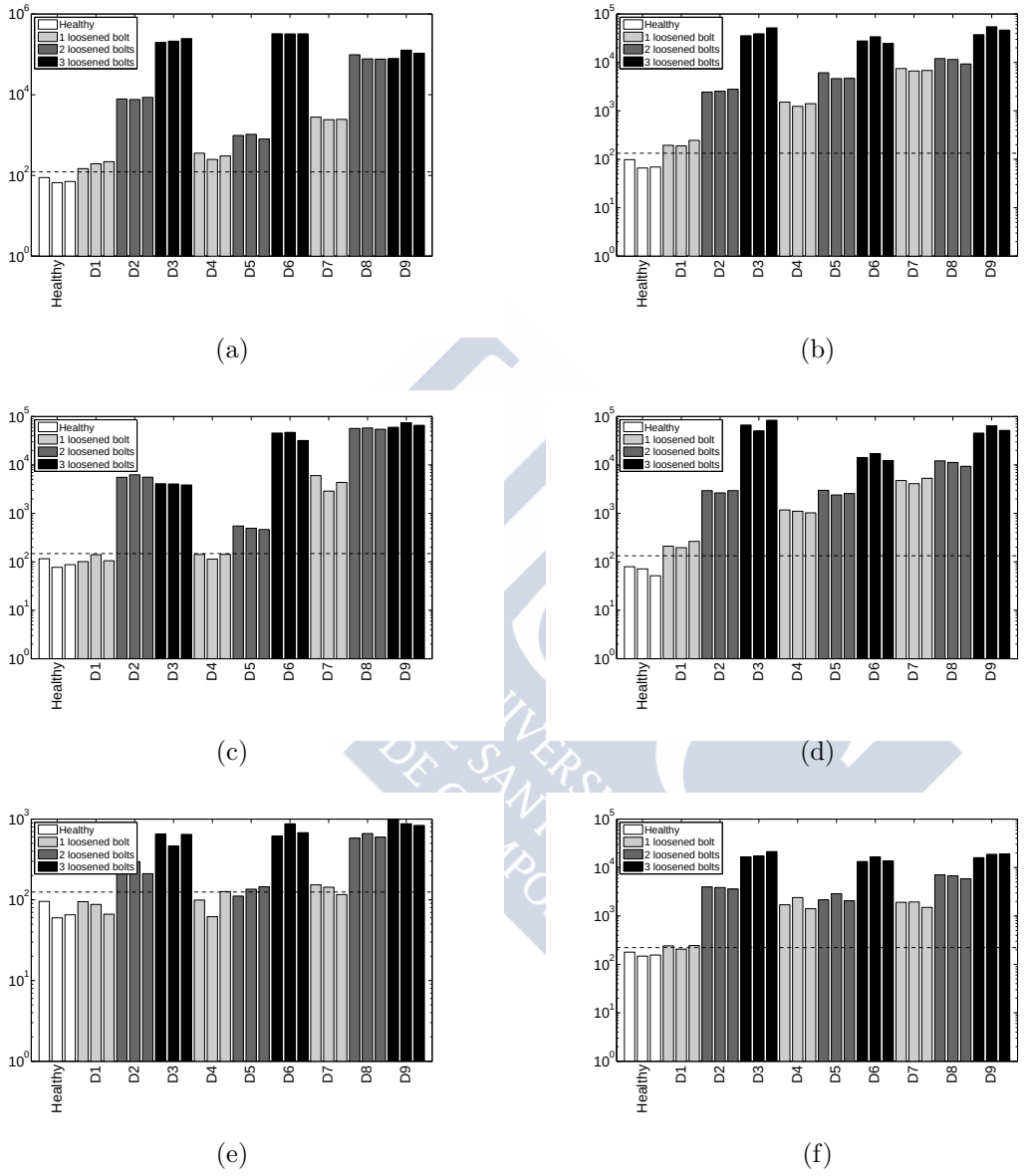

Figure 2.6: Damage detection results using (a) channel 1, (b) channel 2, (c) channel 3, (d) channel 4, (e) channel 5 and (f) channel 6. In the y axis the damage indicator in logarithmic scale is shown.

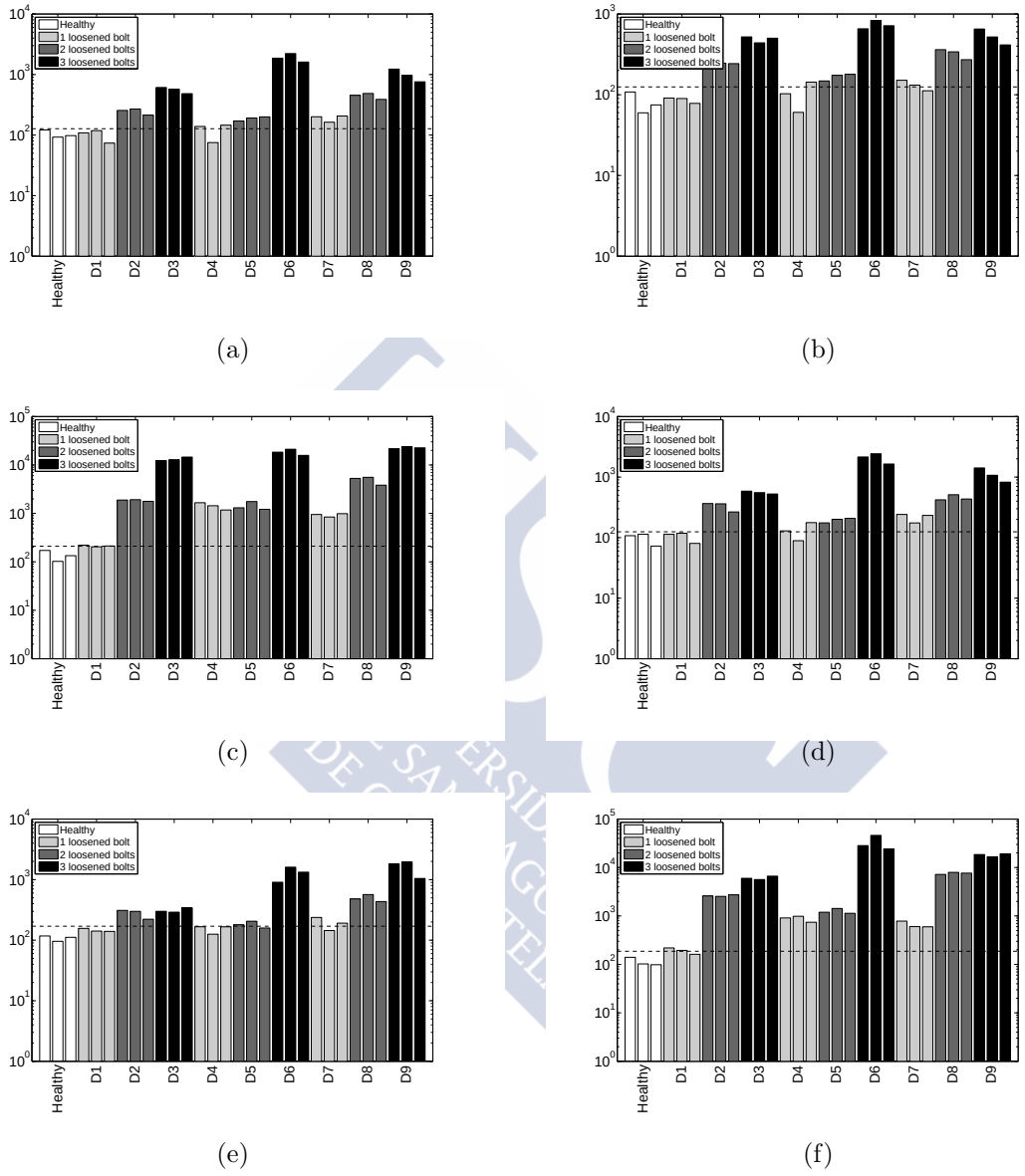

Figure 2.7: Damage detection results using (a) channel 7, (b) channel 8, (c) channel 9, (d) channel 10, (e) channel 11 and (f) channel 12. In the y axis the damage indicator in logarithmic scale is shown.

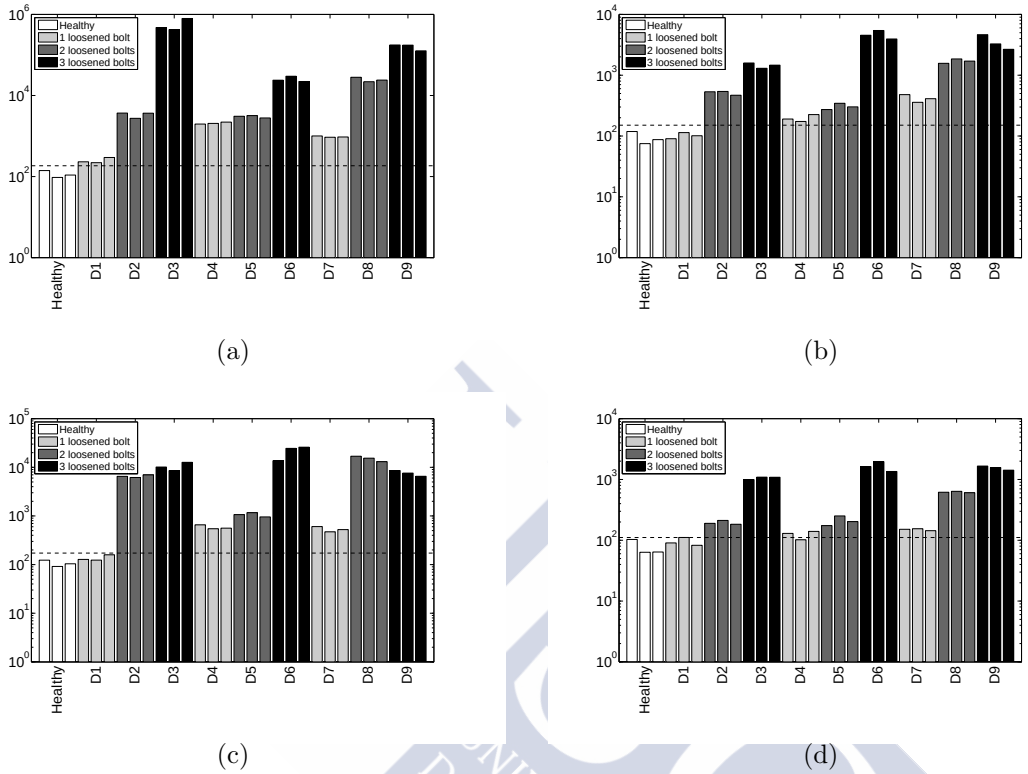

Figure 2.8: Damage detection results using (a) channel 13, (b) channel 14 and (c) channel 15, (d) channel 16. In the y axis the damage indicator in logarithmic scale is shown.

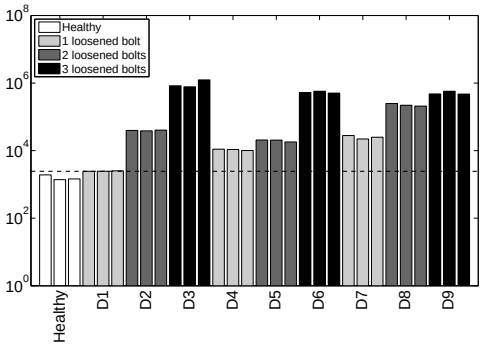

Figure 2.9: Damage detection using the sum of channels and thresholds.

		False alarm rate	*Missed damage rate*								
Channel	*Direction*	Undamaged	D1	D2	D3	D4	D5	D6	D7	D8	D9
1	x	7.9 %	10.8 %	0.0 %	0.0 %	0.0 %	0.0 %	0.0 %	0.0 %	0.0 %	0.0 %
2	y	17.5 %	3.3 %	0.0 %	0.0 %	0.0 %	0.0 %	0.0 %	0.0 %	0.0 %	0.0 %
3	z	7.5 %	85.8 %	0.0 %	0.0 %	60%	0.0 %	0.0 %	0.0 %	0.0 %	0.0 %
4	y	16.7 %	2.5 %	0.0 %	0.0 %	0.0 %	0.0 %	0.0 %	0.0 %	0.0 %	0.0 %
5	x	1.3 %	97.5 %	0.0 %	0.0 %	92.5 %	41.7 %	0.0 %	34.2 %	0.0 %	0.0 %
6	y	44.6 %	36.7 %	0.0 %	0.0 %	0.0 %	0.0 %	0.0 %	0.0 %	0.0 %	0.0 %
7	z	36.7 %	65.0 %	1.7 %	0.0 %	51.7 %	4.2 %	0.0 %	5.8 %	0.0 %	0.0 %
8	x	4.2 %	95.8 %	1.7 %	0.0 %	83.3 %	10.0 %	0.0 %	42.5 %	0.0 %	0.0 %
9	y	12.5 %	60.8 %	0.0 %	0.0 %	0.0 %	0.0 %	0.0 %	0.0 %	0.0 %	0.0 %
10	z	50.4 %	45.8 %	0.0 %	0.0 %	35.0 %	4.2 %	0.0 %	1.7 %	0.0 %	0.0 %
11	z	7.5 %	79.2 %	1.7 %	0.0 %	76.7 %	60.8 %	0.0 %	9.2 %	0.0 %	0.0 %
12	y	25.4 %	51.7 %	0.0 %	0.0 %	0.0 %	0.0 %	0.0 %	0.0 %	0.0 %	0.0 %
13	y	10.8 %	1.7 %	0.0 %	0.0 %	0.0 %	0.0 %	0.0 %	0.0 %	0.0 %	0.0 %
14	x	1.7 %	97.5 %	0.0 %	0.0 %	15.8 %	0.0 %	0.0 %	0.0 %	0.0 %	0.0 %
15	y	21.7 %	80.8 %	0.0 %	0.0 %	0.0 %	0.0 %	0.0 %	0.0 %	0.0 %	0.0 %
16	z	8.8 %	89.2 %	0.0 %	0.0 %	18.3 %	0.0 %	0.0 %	4.2 %	0.0 %	0.0 %
Sums	–	11.7 %	38.3 %	0.0 %	0.0 %	0.0 %	0.0 %	0.0 %	0.0 %	0.0 %	0.0 %

Table 2.6: False alarm and missed damage rate using all available sensors and the sum of all of them.

From Table 2.6 it is concluded that channels in the y (fore–aft) direction present better results, with just some false alarms and missed damages for damage D1. For channels in other directions it is seen that missed damages in another cases appear. The only damages in which no undetected damages appear are those where three bolts have been loosened in the same joint (D3, D6 and D9), which are the more severe considered. In the cases where one or two bolts have been loosened undetected damages appear for some channels.

The channel with the best results is Channel 13 (uniaxial accelerometer in the y direction (number 7) located in Joint 3, see Figure 2.2(b) and Table 2.1. Also Channels 2 and 4 (y direction in Joints 1 and 2 respectively) present good results. And finally the sum of damage indicators for all channels and the threshold given by the sum of each individual threshold gives quite good results.

2.5.2 Damage identification – Tower with jacket

In this section the obtained results in the tower with jacket case are presented (damage detection and identification).

Details of the models used in this case can be found in the appendix 2.7. As before the models have been validated through Gaussianity and whiteness test on the residuals.

Figure 2.10 shows the results of the damage detection, while Figures 2.11(a)–(d) show the results of the identification of the damages. In all the figures, each bar corresponds to a different data record. In the y axis, the value of the damage indicator (given by Equation (2.8)) is shown, in a logarithmic scale; specifically, the sum of the metrics for all of the different channels. As mentioned in the previous section, 16 signals of each state are available. So, the first 16 white bars correspond to the healthy structure. Then there are another 64 bars, 16 for each damage. Each bar corresponds to the resulting damage indicator of a time series. The threshold is indicated with a dashed line at the specific height. For all the experiments the value chosen for α was 10^{-4}.

Table 2.7 summarizes the results obtained. It can be seen how there are very few misclassified instances. Actually there is only a detectability problem for the less severe damages (D1 and D3). For these damages there are also some misclassifications when the identification of the damage is to be performed. In the detection problem there are no healthy signals detected as damaged (false alarms). For all conditions there are no more than 3 misclassified data records. Note that in every case, the sixth signal of the group is the one used in the learning process to characterize the structure in each specific state (healthy or damaged). Since the value of this damage indicator is 0 for the data record

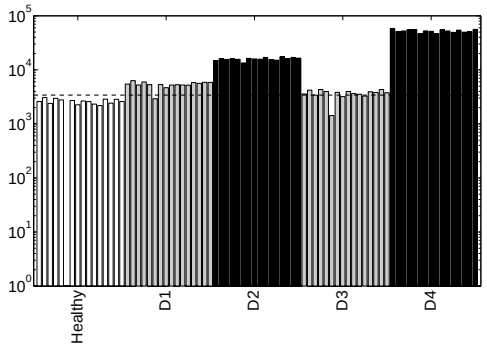

Figure 2.10: Damage detection results.

	Healthy	*Damage 1*	*Damage 2*	*Damage 3*	*Damage 4*
Detection	0/16 (0.0%)	1/16 (6.3%)	0/16 (0.0%)	3/16 (18.8%)	0/16 (0.0%)
Identification D1	0/16 (0.0%)	0/16 (6.3%)	0/16 (0.0%)	1/16 (6.3%)	0/16 (0.0%)
Identification D2	0/16 (0.0%)	0/16 (0.0%)	0/16 (0.0%)	0/16 (0.0%)	0/16 (0.0%)
Identification D3	1/16 (6.3%)	1/16 (6.3%)	0/16 (0.0%)	0/16 (0.0%)	0/16 (0.0%)
Identification D4	0/16 (0.0%)	0/16 (0.0%)	0/16 (0.0%)	0/16 (0.0%)	0/16 (0.0%)

Table 2.7: Summary of the damage detection and identification results (tower with jacket). Number of misclassified instances. Sum of all channels.

used for learning, in logarithmic scale this would be $-\infty$ so it does not appear. For the identification of the damage it is also seen how almost all data records corresponding to that specific damage have damage indicator values under the threshold, whereas the other data records have them above this threshold.

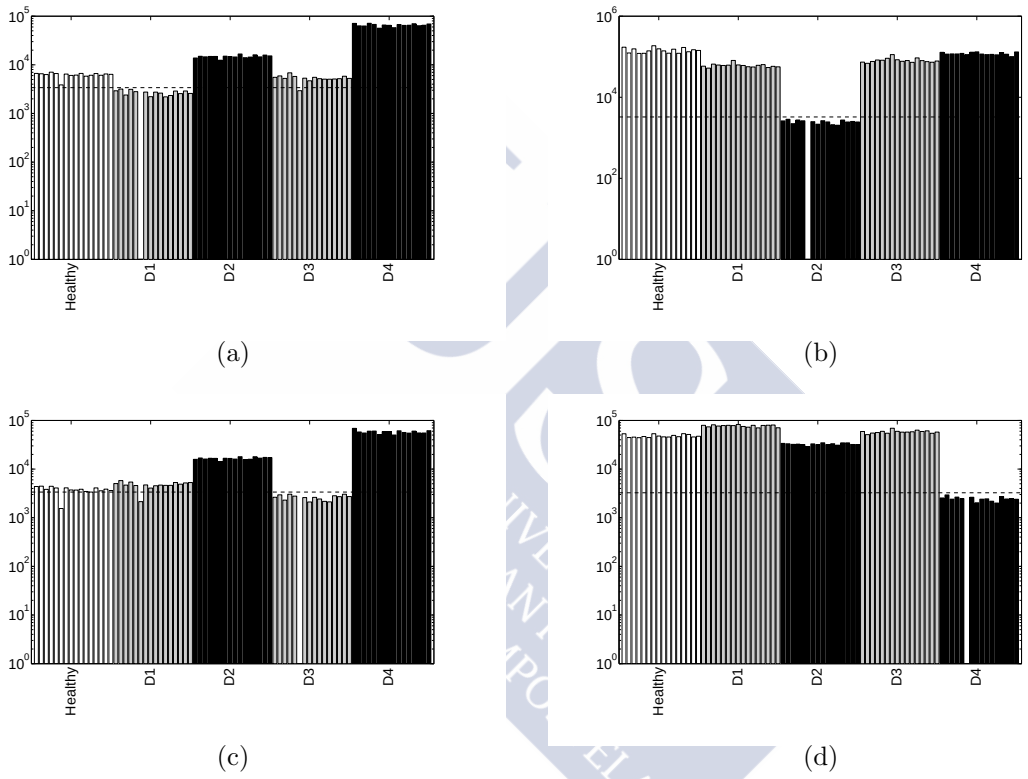

Figure 2.11: Damage identification results learning with one (a) data record from D1, (b) data record from D2, (c) data record from D3 and (d) data record from D4. In the y axis the damage indicator in logarithmic scale is shown.

2.6 Conclusions and future work

The application to a laboratory tower of this damage detection method based on AutoRegressive modeling has been able to correctly detect damage in the structure with a preliminary identification of the type of damage. The chosen metric indicates failure for all the series corresponding to the structure with damage, and it indicates absence of failure for all the series corresponding to a healthy state. The method is also able to identify the type of damage based on a process of learning of each damaged state.

For a real implementation, it must be noted that the identification part is not immediate since process of learning for each type of damage is needed. Anyway, the process of learning the behavior in the different damaged states could be a progressive one, and once a damage has been detected (with this method) and identified (in some other way) this damage can be stored and identified automatically in the sequel. It can also be seen that the metric indicating failure has higher values in the cases where two bolts are loosened than the corresponding case where just one bolt is loosened. This fact is what coul be expected to obtain, since a greater level of damage is related to a higher value of the metric.

2.7 Appendix A - Model details for the tower with jacket case (detection and identification)

Table 2.8 presents all the details of the models estimated for every channel for the detection case, whereas Tables 2.9–2.12 present the estimation details for each of the identification cases.

Channel	*Model Order*	*Condition number*	*Samples per parameter*
1	112	7.98×10^5	34.29
2	200	3.73×10^6	19.2
3	155	7×10^8	24.77
4	108	2.54×10^6	35.56
5	200	3.19×10^6	19.2
6	143	2.82×10^8	26.81
7	173	4.49×10^7	22.2
8	161	1.47×10^7	23.85
9	153	1.1×10^7	25.1
10	177	6.27×10^4	21.69
11	146	1.22×10^5	26.3
12	145	4.1×10^4	26.48
13	152	4.04×10^4	25.26
14	130	6.2×10^3	29.54
15	148	1.44×10^7	25.95

Table 2.8: Baseline phase – Damage detection estimation details (tower with jacket).

Channel	*Model Order*	*Condition number*	*Samples per parameter*
1	109	5.24×10^5	35.23
2	200	2.97×10^6	19.2
3	155	1.12×10^9	24.77
4	150	4.14×10^6	25.6
5	149	2.53×10^6	25.77
6	155	4.92×10^8	24.77
7	104	2.8×10^7	36.92
8	162	1.68×10^7	23.7
9	155	8.19×10^6	24.77
10	189	1.2×10^5	20.32
11	133	1.46×10^5	28.87
12	160	1.09×10^5	24
13	160	3.93×10^4	24
14	163	1.1×10^4	23.56
15	148	1.13×10^7	25.95

Table 2.9: Baseline phase – Damage identification estimation details (tower with jacket), learning with data record from D1

Channel	*Model Order*	*Condition number*	*Samples per parameter*
1	96	5.64×10^5	40
2	158	2.71×10^6	24.3
3	109	2.9×10^8	35.23
4	159	1.62×10^6	24.15
5	158	2.61×10^6	14.3
6	157	1.6×10^8	24.46
7	158	4.6×10^7	24.3
8	162	1.92×10^7	23.7
9	154	7.97×10^6	24.94
10	177	9.6×10^4	21.69
11	118	3.94×10^5	32.54
12	145	3.9×10^4	26.48
13	160	7.68×10^4	24
14	123	2.35×10^4	31.22
15	148	1.08×10^7	25.95

Table 2.10: Baseline phase – Damage identification estimation details (tower with jacket), learning with data record from D2

Channel	*Model Order*	*Condition number*	*Samples per parameter*
1	113	5.96×10^5	33.98
2	200	2.67×10^6	19.2
3	166	8.03×10^8	23.13
4	107	2.67×10^6	35.89
5	199	2.56×10^6	19.3
6	155	3.26×10^8	24.77
7	158	4.25×10^7	24.31
8	108	1.41×10^7	35.56
9	153	9.75×10^6	25.1
10	177	6.29×10^4	21.69
11	176	7.58×10^5	21.82
12	148	5.43×10^4	25.95
13	152	4.03×10^4	25.26
14	132	6.77×10^3	29.1
15	126	1.25×10^7	30.48

Table 2.11: Baseline phase – Damage identification estimation details (tower with jacket), learning with data record from D3

Channel	*Model Order*	*Condition number*	*Samples per parameter*
1	110	1.73×10^6	34.91
2	150	3.4×10^6	25.6
3	118	3.22×10^8	32.54
4	89	1.1×10^6	43.15
5	177	2.84×10^6	21.69
6	182	2.4×10^8	21.1
7	143	1.69×10^7	26.85
8	149	9.09×10^6	25.77
9	154	7.42×10^6	24.94
10	177	6.11×10^4	21.69
11	176	8.6×10^5	21.82
12	141	3.49×10^4	27.23
13	144	4.98×10^4	26.67
14	128	1.15×10^4	30
15	142	1.37×10^7	27.04

Table 2.12: Baseline phase – Damage identification estimation details (tower with jacket), learning with data record from D4

Chapter 3

Damage detection under varying environmental conditions: assessment with a scale wind turbine blade

3.1 Introduction

Structural damage diagnosis is of primary importance in mechanical, aerospace, and civil engineering. Vibration–based methods are based on the premise that damage causes changes in the structural dynamics which may be detected through measured vibration data records and inverse–type techniques [26]. This is accomplished by monitoring a *characteristic quantity* (or else *feature vector*), selected to best embed the dynamical information pertinent to damage, which is estimated based on the measured vibration data records [36, 68].

The aim of the present chapter is the introduction of a statistical, non–model based, PCA–type methodology, capable of: (a) achieving high damage detection performance under environmental effects and uncertainty through improved learning that involves the use of data records obtained under healthy *and* various damage scenarios (supervised learning), (b) operating with a low number of sensors (even a single sensor), and (c) operating within a limited and low frequency bandwidth.

In standard PCA–type methods a feature vector simply corresponding to the selected, least important, eigenvalues is formed in a single step. The proposed methodology uses

supervised learning where damaged–state data records are employed to *sequentially* form an improved feature vector. This is constructed by appending a transformed scalar element at a time under the condition that it *optimally*, among all remaining elements, improves damage detectability. This leads to the formulation of feature vectors with optimized sensitivity to damage, and thus overall high damage detectability.

Three particular methods – incarnations of the methodology – are introduced and validated: Two are *non–parametric* (early versions reported in the conference papers [48, 47]), one based on the vibration response Power Spectral Density (PSD) as feature vector and the other on the excitation–response Frequency Response Function (FRF). The third is *parametric*, based on the parameter vector of an AutoRegressive (AR) representation of the vibration response as feature vector. They have been published in the journal paper [46].

The laboratory validation and comparative assessment of the three methods is based on an experimental case study focusing on damage detection on a laboratory–scale wind turbine blade. For this purpose two levels of damage are considered under varying environmental conditions, which include temperature variation in the $[-20, 20]^{\circ}$C range and additional uncertainty coming from the experiment and the potential presence of sprayed water.

The rest of the chapter is organized as follows: The damage detection methodology is presented in section 3.2, and its laboratory validation in section 3.3. The conclusions of the study are finally summarized in section 3.4.

3.2 The damage detection methodology

Vibration–based damage detection methods utilize a feature vector (characteristic quantity) selected to best embed the dynamical information pertinent to potential structural damage, and this vector is estimated based on measured vibration data records [38]. In conventional methods feature vector selection is based on a single representative data record from the healthy state of the structure. This selection, and the environmental conditions under which the data record is acquired, are crucial for detection performance, as changes in such conditions, or the use of a non–representative data record, or the presence of other uncertainties, may lead to significant performance deterioration.

A typical approach aiming at overcoming this is based on the use of *multiple data records* corresponding to the healthy state of the structure and a PCA–type (or related)

procedure aiming at feature vector transformation and dimensionality reduction in a way in which information associated with variability due to uncertainty is rejected, while that associated with damage is retained [40, 114]. Yet, the degree to which these characteristics are achieved is not warranted, as the selections made are not based on checks with damaged–state data records.

The postulated damage detection methodology aims at overcoming this limitation by employing multiple data records obtained under *both* the healthy and damaged states of the structure, thus being of the *supervised learning* type. It is PCA–type, and its main idea consists of using a supervised learning procedure for the *sequential* formulation a feature vector (characteristic quantity). This vector is obtained by appending a transformed scalar element to it at a time, under the condition that it *optimally*, among all remaining elements, improves damage detectability as obtained by using the available damaged–state data records. Optimality is based upon a normalized Mahalanobis distance type criterion.

3.2.1 Preliminaries

Based on the feature vector (characteristic quantity) selected, three distinct methods – incarnations of the methodology – are considered (see [38] on their conceptual basis and elementary forms):

(a) A non–parametric Power Spectral Density (PSD) based method in which the characteristic quantity is the non–parametric vibration response PSD (response–only scheme; the excitation is not used).

(b) A non–parametric Frequency Response Function (FRF) based method in which the characteristic quantity is the non–parametric excitation–response FRF (excitation–response scheme; the excitation is used).

(c) A parametric AutoRegressive (AR) model parameter based method in which the characteristic quantity is the parameter vector of the vibration response AR model (response–only scheme; the excitation is not used).

More details on the feature vector employed by each method follow.

Initial feature vector selection and estimation (for the three incarnations).

For a given measured random vibration response signal $y[t]$ and the corresponding excitation $x[t]$, $t = 1, \ldots, N$[1], the sample mean is adjusted to zero and the sample variance

[1] t designates normalized discrete time; N designates the signal length in samples.

normalized to unity (independently for the response and excitation). The normalized signals will still be referred to as $x[t]$ and $y[t]$. Then the Welch Power Spectral Density (PSD) point estimate [38] of the vibration response is obtained as (MATLAB function *pwelch.m*):

$$\widehat{S}_{yy}(\omega) = \frac{1}{K}\sum_{i=1}^{K} Y_L^{(i)}(j\omega)\cdot Y_L^{(i)}(-j\omega), \tag{3.1}$$

with

$$Y_L^{(i)}(j\omega) = \frac{1}{\sqrt{L}}\sum_{t=1}^{L} a[t]y^{(i)}[t]e^{-j\omega tT_s},$$

where the hat indicates estimator/estimate, $\omega \in [0, 2\pi/T_s]$ stands for frequency in rad/s, T_s for the sampling period, j for the imaginary unit, K for the number of segments used (each of length L), and $a[t]$ the selected time window. The superscript (i) indicates a specific segment of the signal.

The Welch PSD estimate $\widehat{S}_{xx}(\omega)$ for the excitation signal is defined analogously, while the Welch Cross Power Spectral Density (CPSD) point estimate between the excitation and the response then is:

$$\widehat{S}_{yx}(j\omega) = \frac{1}{K}\sum_{i=1}^{K} Y_L^{(i)}(j\omega)\cdot X_L^{(i)}(-j\omega), \tag{3.2}$$

with

$$X_L^{(i)}(j\omega) = \frac{1}{\sqrt{L}}\sum_{t=1}^{L} a[t]x^{(i)}[t]e^{-j\omega tT_s}.$$

The corresponding FRF point estimate is then obtained as (MATLAB function *tfestimate*):

$$\widehat{H}(j\omega) = \widehat{S}_{yx}(j\omega)/\widehat{S}_{xx}(\omega). \tag{3.3}$$

The parametric method employs AR modelling of the vibration response signal $y[t]$ that is [38]:

$$y[t] + \sum_{i=1}^{n_a} a_i \cdot y[t-i] = w[t], \qquad w[t] \sim \text{iid } \mathcal{N}(0, \sigma_w^2), \tag{3.4}$$

with n_a designating the AutoRegressive (AR) order, a_i the AR parameters, and $w[t]$ the innovations (white) signal which is zero mean and of variance σ_w^2; iid stands for independent identically distributed and $\mathcal{N}(\cdot,\cdot)$ for normal distribution with the indicated mean

and variance. AR estimation is based on Linear Least Squares ([38]; MATLAB function *arx.m*). The required model order is selected via the Bayesian Information Criterion (BIC) [38], while posterior model validation (consisting of whiteness and Gaussianity tests on the model residuals) is performed prior to final model selection.

Based on the above, the initial feature vector, say $\boldsymbol{\theta} \in \mathbb{R}^n$, is selected as follows for each one of the methods:

PSD–based method: non–parametric response–only

$$\boldsymbol{\theta} = [S_{yy}(\omega_1) \ \ldots \ S_{yy}(\omega_n)]^T . \tag{3.5a}$$

FRF–based method: non–parametric excitation–response

$$\boldsymbol{\theta} = [|H(j\omega_1)| \ \ldots \ |H(j\omega_n)|]^T . \tag{3.5b}$$

AR–based method: parametric response–only

$$\boldsymbol{\theta} = [a_1 \ \ldots \ a_n]^T . \tag{3.5c}$$

with n designating the feature vector dimensionality and ^{T} matrix transposition.

3.2.2 Outline of the methodology

As with all vibration–based methods, the methodology involves a *baseline (training) phase* and an *inspection phase*. The first phase is performed once, during set–up, while the latter – which is much simpler – corresponds to normal operation and may be performed periodically or continuously in time. The two phases are presented in the sequel.

Baseline phase

A "healthy set" Θ_0, consisting of ρ_0 data records obtained from the structure in healthy state, under different environmental conditions and uncertainty, is used. Based on this, an interval estimate (sample mean and covariance matrix) of the *initial* feature vector is obtained using ρ_0 point estimates of the form of the previous subsection.

A "damaged set" Θ_d, consisting of ρ_d data records obtained from the structure under various damage states and different environmental conditions and uncertainty, is also used. This set is needed in order to select scalar components of the feature vector according to their damage detection capability.

A Principal Component Analysis (PCA) [58, pp. 1–6] based sequential procedure is then postulated in order to formulate a corresponding *final* feature vector that should be

insensitive to environmental conditions and uncertainty, but still sufficiently sensitive to damage. The precise steps of the procedure are outlined in the sequel.

Step 1. *Sample mean and covariance estimation of the initial feature vector.*
Based on the ρ_0 point estimates of the ($n-$dimensional) feature vector $\boldsymbol{\theta}$ (obtained from the "healthy set" Θ_0), an interval estimate (sample mean and covariance) is obtained as:

$$\overline{\boldsymbol{\theta}} = \frac{1}{\rho_0} \sum_{\boldsymbol{\theta} \in \Theta_0} \boldsymbol{\theta}, \qquad \widehat{\mathbf{P}} = \frac{\sum_{\boldsymbol{\theta} \in \Theta_0} (\boldsymbol{\theta} - \overline{\boldsymbol{\theta}})(\boldsymbol{\theta} - \overline{\boldsymbol{\theta}})^T}{\rho_0 - 1}. \tag{3.6}$$

It is noted that in order to avoid potential ill–conditioning of the covariance matrix, the feature vector dimensionality n should be sufficiently smaller than the number of data records ρ_0. Otherwise, alternative estimators, such as a shrinkage–type covariance estimator (which is always well conditioned and optimum in the mean square error sense) or a pseudomodel–based estimator should be employed [97, 80].

Step 2. *Principal Component Analysis & feature vector transformation.*
The obtained sample covariance matrix is decomposed as follows (PCA):

$$\widehat{\mathbf{P}} = \mathbf{U}\, \boldsymbol{\Lambda}\, \mathbf{U}^T, \tag{3.7}$$

where $\boldsymbol{\Lambda} = \text{diag}\,(\lambda_1, \ldots, \lambda_n) \in \mathbb{R}^{n \times n}$ and $\mathbf{U} = [\mathbf{u}_1 \quad \ldots \quad \mathbf{u}_n] \in \mathbb{R}^{n \times n}$ with diag(...) designating a diagonal matrix composed of the indicated elements, $\lambda_i (> 0)$ the $i-$th eigenvalue of $\widehat{\mathbf{P}}$ ordered in descending order, and $\mathbf{u}_i$ the corresponding normalized eigenvector. Each feature vector $\boldsymbol{\theta}$ may be then transformed into principal components as follows:

$$\mathbf{s} = \mathbf{U}^T (\boldsymbol{\theta} - \overline{\boldsymbol{\theta}}) \in \mathbb{R}^n, \tag{3.8}$$

which, for elements in Θ_0, warrants a sample mean of $\mathbf{0}$ and diagonal covariance matrix $\boldsymbol{\Lambda}$.

Step 3. *Feature vector reduced dimensionality ($\underline{n}$) selection.*
The feature vector reduced dimensionality is selected as the integer that satisfies the condition:

$$\underline{n} = \text{minimum integer such that} \quad \frac{\sum_{j=1}^{\underline{n}} \lambda_j}{\sum_{j=1}^{n} \lambda_j} \geq \delta \tag{3.9}$$

where δ $(0 < \delta < 1)$ is a user defined threshold (typical values $0.950 \ldots 0.999$). Following this, the first $\underline{n}$ transformed feature vector components are discarded, while certain (specifically n_0) of the remaining $n - \underline{n}$ transformed components (which are $\{s_{\underline{n}+1}, \ldots, s_n\}$

are to be kept in the feature vector according to the procedure described in subsequent steps (also see Figure 3.1).

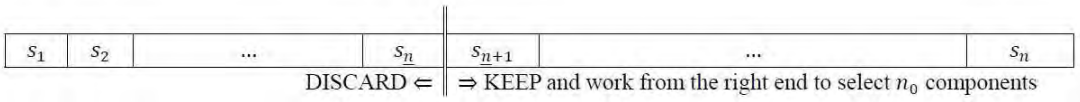

Figure 3.1: The elements of transformed feature vector $\mathbf{s}$ in relation to dimensionality reduction.

Step 4. *Iteration index j initialization.*
n_0, out of the remaining $n - \underline{n}$, transformed feature vector components are to be kept in the final feature vector according to an iterative procedure characterized by the iteration index j ($j = 1, \ldots, n - \underline{n}$). In each iteration a single scalar component is to be selected for inclusion in the transformed feature vector, until the inclusion of a new component no longer implies an improvement on damage detectability.

The iteration index is now initialized to $j = 1$ (feature vector with a single component).

Step 5. *Selecting a new scalar component for the transformed feature vector (greedy algorithm).*
Selecting a new (not previously appended) scalar component to the transformed feature vector is examined through the quantity:

$$R_j = \frac{\min_{\boldsymbol{\theta} \in \Theta_d} D_j^2(\boldsymbol{\theta})}{\max_{\boldsymbol{\theta} \in \Theta_0} D_j^2(\boldsymbol{\theta})}, \tag{3.10}$$

with $D_j^2(\boldsymbol{\theta})$ designating the squared Mahalanobis distance[2] of the *transformed* feature vector $\boldsymbol{\theta}$ (with j scalar components designated by the indices $b(1), \ldots, b(j)$) from the (transformed "healthy") set Θ_0. The numerator of this quantity represents the minimum[3] (among all "damaged" baseline feature vectors Θ_d) Mahalanobis distance to the set of "healthy" feature vectors Θ_0. The denominator represents the maximum[4] (among all

[2]The Mahalanobis distance (MATLAB function *mahal.m*) of a vector $\boldsymbol{\theta} = [\theta_1 \ldots \theta_n]^T$ from a probability density with mean $\overline{\boldsymbol{\theta}} = [\overline{\theta}_1 \ldots \overline{\theta}_n]^T$ and covariance matrix $\mathbf{P}$ is defined as [58, p. 237]:

$$D(\boldsymbol{\theta}) = \sqrt{(\boldsymbol{\theta} - \overline{\boldsymbol{\theta}})^T \mathbf{P}^{-1} (\boldsymbol{\theta} - \overline{\boldsymbol{\theta}})}.$$

[3]The minimum is taken in order to consider the "least detectable" case.
[4]The maximum is taken in order to consider the "most probable false alarm".

"healthy" baseline feature vectors Θ_0) Mahalanobis distance to the set of "healthy" feature vectors Θ_0. Note that the set for which the maximum and the minimum are computed are not the same.

Each Mahalanobis distance is given by:

$$D_j^2(\boldsymbol{\theta}) = \mathbf{s}_j^T \boldsymbol{\Lambda}_j^{-1} \mathbf{s}_j, \tag{3.11}$$

with:

$$\begin{gathered} \mathbf{s}_j = \mathbf{U}_j^T(\boldsymbol{\theta} - \overline{\boldsymbol{\theta}}) \in \mathbb{R}^j, \qquad \boldsymbol{\Lambda}_j = \operatorname{diag}\left(\lambda_{b(1)}, \ldots, \lambda_{b(j)}\right) \in \mathbb{R}^{j \times j}, \\ \mathbf{U}_j = \left[\mathbf{u}_{b(1)} \ \ldots \ \mathbf{u}_{b(j)}\right] \in \mathbb{R}^{n \times j}. \end{gathered} \tag{3.12}$$

For the current j the addition of a new scalar component, designated by the index $b(j)$, into the transformed feature vector is now examined. For the case $j = 1$, $b(1)$ is selected as:

$$b(1) = \arg\max_{b(1) \in \{\underline{n}+1, \ldots, n\}} R_1(b(1)). \tag{3.13}$$

For $j > 1$ the new scalar component is to be selected among the remaining components as that maximizing $R_j(b(j))$ with respect to the remaining $b(j)$'s, that is:

$$b(j) = \arg\max R_j(b(j)) \qquad \text{for } b(j) \in \{\underline{n}+1, \ldots, n,\ b(j) \neq b(k)\, \forall\, k < j\}. \tag{3.14}$$

Let the value of this maximum quotient, at iteration j, be designated as R_j^{max}. The selected new component $b(j)$ will be appended to the feature vector if and only if:

$$R_j^{max} > R_{j-1}^{max} \tag{3.15}$$

which means that the new component improves damage detectability. In this case proceed to Step 6. Otherwise proceed to Step 7.

Step 6. *Iteration index j increase.*
Set $j \leftarrow j + 1$ and go back to Step 5. If $j = n - \underline{n} + 1$ then there are no components left for examination; set $n_0 = n - \underline{n}$ and proceed to the next step (Step 7).

Step 7. *The final transformed feature vector.*
At this stage n_0 components are retained in the feature vector and the $\mathbf{U_{n_0}}$ matrix is obtained as:

$$\mathbf{U}_{n_0} = \left[\mathbf{u}_{b(1)} \ \ldots \ \mathbf{u}_{b(n_0)}\right] \in \mathbb{R}^{n \times n_0} \tag{3.16}$$

The final transformed feature vectors are then computed as:

$$\mathbf{s}_{n_0} = \mathbf{U}_{n_0}^T(\boldsymbol{\theta} - \overline{\boldsymbol{\theta}}) \in \mathbb{R}^{n_0}. \tag{3.17}$$

Remarks:

1. The overall aim of the procedure is the formulation of a feature vector consisting of Principal Components through which the effects of damage are evident, irrespectively of environmental conditions and uncertainty. Since the sample covariance matrix is based on data records under different environmental conditions, the main part of the feature vector covariance is expected to stem from the variation of those conditions. For this reason the "last" principal components (corresponding to the smallest eigenvalues) are expected to be least dependent on environmental conditions and uncertainty – but still sensitive to damage – and are retained in the procedure (see Figure 3.1).

2. From the initially retained components, only n_0 are to be finally kept in the feature vector according to their sensitivity to damage. The selected mathematical tool for measuring this sensitivity is based on a squared Mahalanobis type distance. The aim then is to retain components for which the Mahalanobis distance is "large" when the feature vector belongs to a damaged structural state, but "small" when it corresponds to a healthy state. In Figure 3.2 an example involving three principal components is shown with the sets Θ_0 (represented by the blue triangles) and Θ_d (represented by red circles). The blue set is the reference set with respect to which all distances are measured. The red circles represent damage cases. The distances of all blue dots and all red dots with respect to the set of blue dots are computed. Observe how the blue triangles are centered around the zero vector. The Θ_d set is not completely separated from Θ_0, but actually surrounding it. The aim is to retain the components which make these two sets as *separable* as possible (blue set as close to the $\mathbf{0}$ $j-$dimensional vector, and red set as separated as possible, leaving in general the blue set inside it). As already stated, the idea is the inclusion of a new component only if it results into a better separation of the two sets.

Inspection phase

Given a fresh vibration data record from the structure operating under a current, to be determined, structural state, the current feature vector $\boldsymbol{\theta}_u$ is obtained and then trans-

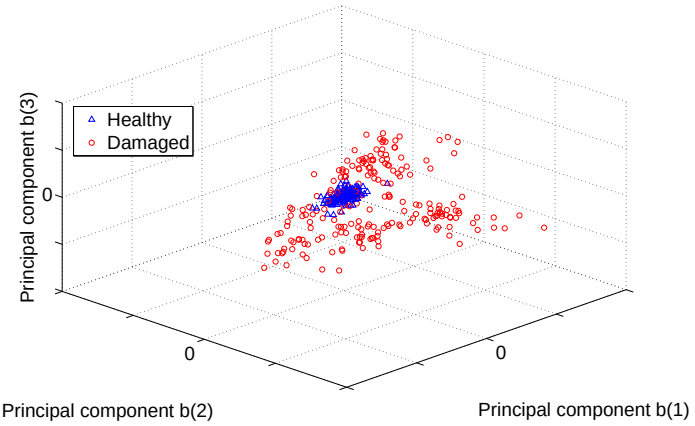

Figure 3.2: An example of 3-dimensional (three principal components) sets Θ_0 and Θ_d.

formed according to Equation (3.17). The squared Mahalanobis distance between $\boldsymbol{\theta}_u$ and the "healthy" set Θ_0 is then obtained as:

$$D^2_{n_0}(\boldsymbol{\theta}_u) = \mathbf{s}^T_{n_0} \boldsymbol{\Lambda}^{-1}_{n_0} \mathbf{s}_{n_0}, \text{ with } \boldsymbol{\Lambda}_{n_0} = \text{diag}\left(\lambda_{b(1)}, \ldots, \lambda_{b(n_0)}\right) \in \mathbb{R}^{n_0 \times n_0} \tag{3.18}$$

Since each principal component is a linear combination of random variables, applying the central limit theorem [58, p. 236] leads to normality (even if the original variables are not normally distributed). Taking this into account, the squared Mahalanobis distance in Equation (3.18) is a sum of n_0 squared $N(0,1)$ and mutually independent random variables, thus D^2 follows a χ^2 distribution with n_0 degrees of freedom.

Then the following hypothesis testing problem may be formulated:

$$\begin{aligned} H_o: &\quad D^2_{n_0}(\boldsymbol{\theta}_u) = 0 \quad \text{(null hypothesis – healthy structure)} \\ H_1: &\quad D^2_{n_0}(\boldsymbol{\theta}_u) > 0 \quad \text{(alternative hypothesis – damaged structure).} \end{aligned} \tag{3.19}$$

Then for a user selected α risk level (false alarm probability equal to α), the quantity $D^2_{n_0}(\boldsymbol{\theta}_u)$ should – under the null H_o hypothesis – be in the range $(0, \chi^2_{1-\alpha}(n_0)]$ with probability $1-\alpha$ (see Figure 3.3), so that decision making is as follows:

$$\begin{aligned} D^2_{n_0}(\boldsymbol{\theta}_u) \leq \chi^2_{1-\alpha}(n_0) &\quad \Rightarrow \quad \text{Healthy structure} \\ \text{Else} &\quad \Rightarrow \quad \text{Damaged structure} \end{aligned} \tag{3.20}$$

with $\chi^2_{1-\alpha}(n_0)$ designating the critical point of the χ^2 distribution with n_0 degrees of freedom at the $1-\alpha$ level.

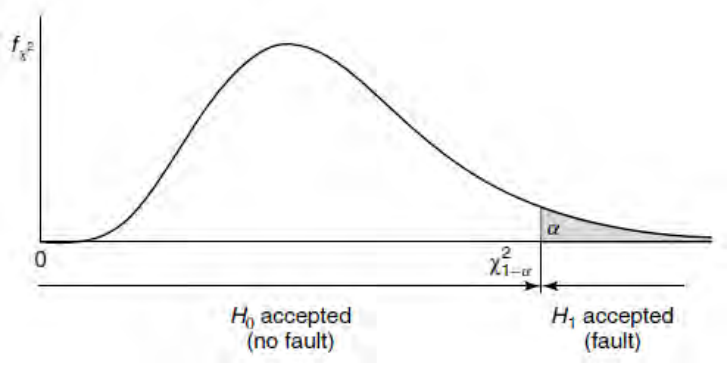

Figure 3.3: Statistical hypothesis testing based on a χ^2- distributed statistic (one–sided test).

3.3 Laboratory validation of the methodology

The postulated methodology – in the form of its three methods – is experimentally validated, and a comparative assessment of the methods is also made. This is based on a case study focusing on damage detection on a lab–scale wind turbine blade under varying environmental conditions which include temperature variation in the $[-20, 20]^{\circ}$C range and the potential presence of moisture (sprayed water). Two levels of damage are considered. In each test case only one of four measured vibration response signals is used within a limited $(20 - 2000$ Hz) frequency range.

It is noted that the use of a laboratory–scale structure in this study is sufficient for testing and assessing the postulated methodology, which is the goal of the present work. Yet, it is clear that for a proper practical assessment of damage detection on wind turbine blades, testing with full–scale blades is also necessary, mainly because damage effects are *not* expected to be scalable.

3.3.1 The experimental set-up, the damage scenarios, and the experiments

The lab–scale wind turbine composite blade employed (length 0.71 m including the clamping, maximum width 0.135 m, mass 0.646 kg) is depicted in the drawing of Figure 3.4(a). The blade is placed in a freezer and clamped (by means of 3 bolts – torque of 5 N·m) on one end on a steel base in a cantilever position and excited by a shaker – Figure 3.4(b).

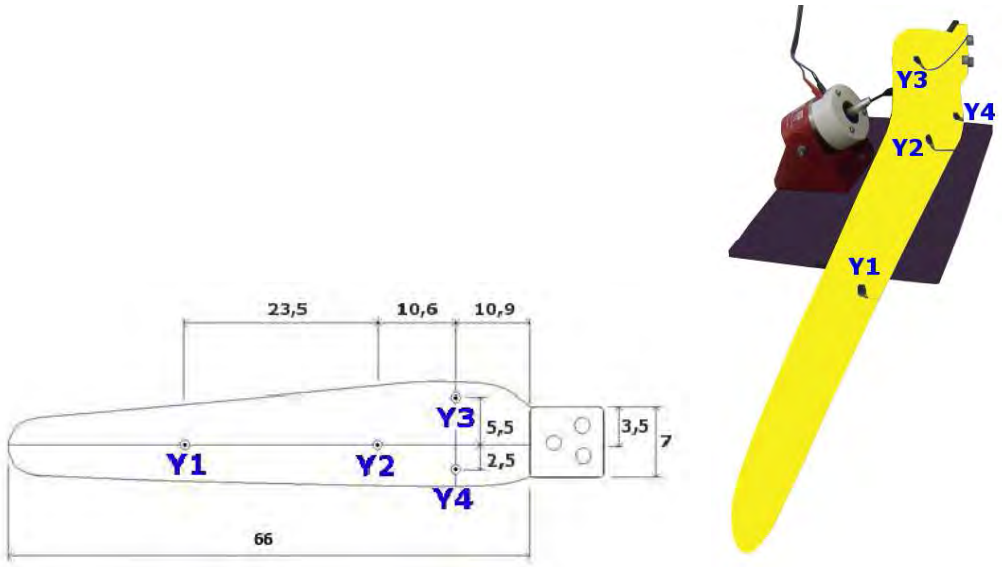

(a) (b)

Figure 3.4: (a) Drawing of the lab–scale blade showing the vibration measurement positions (Y1–Y4; distances in cm), (b) photo of the experimental set–up showing the clamping, the shaker, and the vibration measurement positions.

The experiments are carried out under quasi–static thermal conditions with the precise temperature measured via a digital thermometer with a K–type bead thermocouple attached near the clamp. Water spraying is also used in some experiments for simulating rainy conditions.

Two levels of damage are introduced: The first one (D1) consists of a semicircular cut at the trailing edge, with a radius of 2.5 mm (Figure 3.5(a)). The second (D2) is based on enlarging the cut, with the total length now being 1.5 cm while the width remains at 2.5 mm (Figure 3.5(b)).

In each experiment the blade is excited by a random stationary force, with approximately flat spectrum within its bandwidth of $20 - 2000$ Hz, applied via a shaker and measured via an impedance head (PCB M288D01, sensitivity 98.41 mV/lb). The random vibration response is measured at four points (Points Y1, Y2, Y3 and Y4) via lightweight accelerometers (PCB ICP 352C22, 0.5 gr, bandwidth 0.003 – 10 kHz, sensitivity $\approx 1.052 mV/m/s^2$). All signals are collected by means of two SigLab modules at a sampling frequency of $f_s = 5120$ Hz. Following sample mean subtraction, each signal (excitation and response) is normalized to unit sample variance.

Several hundreds of experiments are carried out for each health state of the blade and under various environmental conditions (temperatures and water sprayed or not). For the Healthy and Damage 2 states, signals are collected every 2°C, whereas in the other conditions (Healthy with water, Damage 1 and Damage 2 with water), this is done every 4°C. In each case, 40 signals are collected, 5 of them to be used exclusively in the baseline phase and the remaining 35 in the inspection phase. Complete details are provided in Table 3.1.

It should be emphasized that only a *single* measured vibration response signal (Y1 or Y2 or Y3 or Y4) is used in each damage detection case, while, depending on the particular damage detection method (details in subsequent sections), the measured excitation signal may or may not be used.

(a) (b)

Figure 3.5: Detail of the considered damages: (a) damage D1 (small), (b) damage D2 (large).

Blade Health State	*Temperature step – Number of cases (Temp. range $-20..20^\circ C$)*	*Number of experiments (for each temperature)*		*Total number of experiments (data records)*			
		Baseline	*Inspection*	*Baseline*		*Inspection*	
Healthy	Step 2°C – 21 cases	5	35	105	**160**	735	**1120**
Healthy with water	Step 4°C – 11 cases	5	35	55		385	
Damage 1	Step 4°C – 11 cases	5	35	55	**55**	385	**385**
Damage 2	Step 2°C – 21 cases	5	35	105	**160**	735	**1120**
Damage 2 with water	Step 4°C – 11 cases	5	35	55		385	
Sampling frequency $f_s = 5120$ Hz							
Signal bandwidth $20 - 2000$ Hz							
Signal length $N = 32768$ samples (6.4 s)							

Table 3.1: Overview of the experiments and experimental details.

3.3.2 Experimental results

Details and damage detection results corresponding to each one of the methods are presented in the sequel.

Preliminary considerations

Welch based PSD and FRF estimates, obtained using Θ_0–sample–long segments (0% overlap, $K = 16$ averaged segments), are for the vibration response Y2 case depicted in Figures 3.6 and 3.7, respectively. The first 50 AR parameters are (also for the Y2 case) presented in Figure 3.8. Along with point estimates, 95% confidence intervals are also shown; it is worth noting that the latter appear narrower for the FRF curves and the AR parameters than for their PSD counterparts.

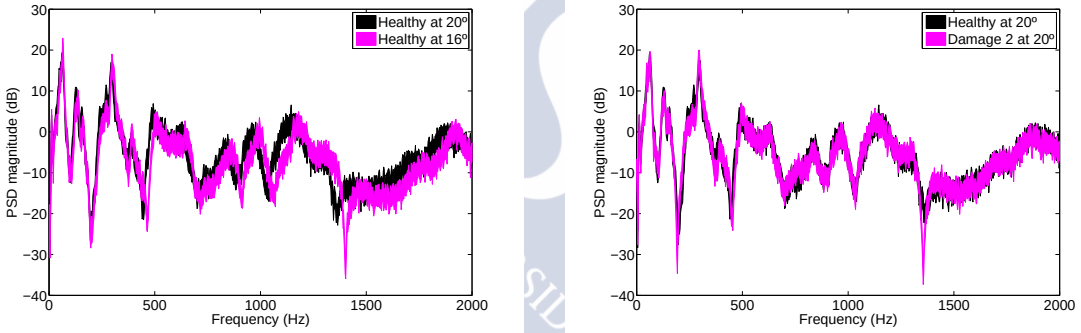

Figure 3.6: PSD estimates along with 95% confidence intervals for the vibration response at position Y2: (a) healthy case at 20°C (black) compared to healthy case at 16°C (pink), (b) healthy case at 20°C (black) compared to damage 2 at the same temperature of 20°C (pink).

In Figures 3.6(a), 3.7(a) and 3.8(a) the PSD, FRF, and AR parameter, respectively, interval estimates for two "healthy" signals at two different temperatures are presented, whereas in Figures 3.6(b), 3.7(b) and 3.8(b) those of a "healthy" and a "damaged" signal at the same temperature are shown. It may be observed that changes due to the temperature difference (even though only 4°C) are larger than those due to damage at a fixed temperature (particularly at higher frequencies). This is a serious problem for standard methods in which environmental effects are not properly accounted for.

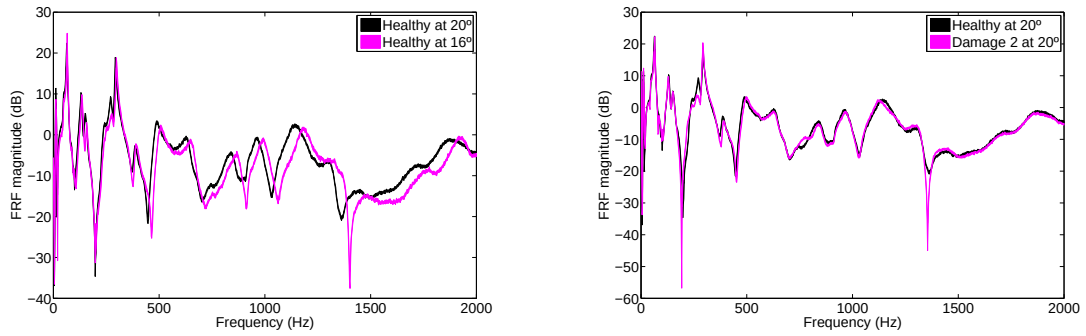

Figure 3.7: FRF estimates along with 95% confidence intervals for the vibration response signal at position Y2: (a) healthy case at 20°C (black) compared to with healthy case at 16°C (pink), (b) healthy case at 20°C (black) compared to damage 2 at the same temperature of 20°C (pink).

The selected methodology parameters are provided in Table 3.2. For good estimation of the covariance matrix it is desirable to have more data records than estimated parameters. For this reason PSD and FRF estimation is based on a short segment length ($L = 128$), which (as the bandwidth is limited to 2000 Hz) leads to an initial feature vector dimensionality of $n = 51$. Likewise, the first $n = 50$ AR parameters are used in the AR based methods.

The set Θ_0 is then composed of 5 data records per structural and environmental condition (baseline phase; Table 3.1), which leads to a dimensionality of $\rho_0 = 160$ for this set. Analogously for Θ_d, 5 data records from each structural and environmental condition are used, resulting into $\rho_d = 215$. The selected values of $\underline{n}$ and n_0 are, for all three methods, provided in Table 3.2 (sensor position Y2). All other parameters, including δ and α, are kept common for all vibration response sensor positions and every method.

The non–parametric PSD based method

The method's selected parameters are provided in Table 3.2. The steps are described in the sequel using the vibration response position Y2.

Baseline phase

Step 1: 160 feature vectors corresponding to the baseline healthy data set Θ_0 are used for interval estimation (Equation (3.6)).

Common parameters			
ρ_0	160 (from 32 conditions)	ρ_d	215 (from 43 conditions)
δ	0.997	α	10^{-10}
$\underline{n}$	PSD scheme: 11 FRF scheme: 18 AR scheme: 10	n_0	PSD scheme: 12 FRF scheme: 13 AR scheme: 13

Non-parametric methods			
Estimation method	Welch	*Window type*	Hamming
L	128 samples	K	256 segments
Overlap	0 samples	n	51

Parametric (AR based) method			
n_a	200	n	50

Table 3.2: Parameters used for the non-parametric and parametric methods.

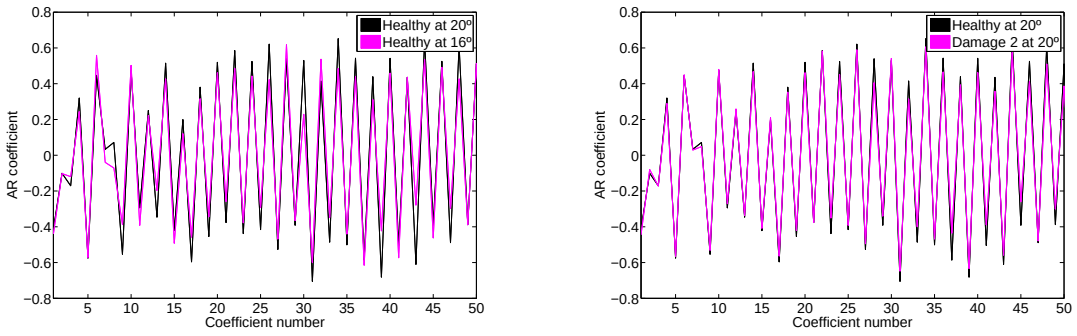

Figure 3.8: The first 50 AR parameter estimates along with their 95% confidence intervals (vibration response signal at position Y2): (a) healthy case at 20°C (black) compared to healthy case at 16°C (pink), (b) healthy case at 20°C (black) compared to damage 2 at the same temperature of 20°C (pink).

Step 2: PCA is performed on the estimated covariance matrix (Matlab function *princomp.m*) and the transformed feature vectors are obtained according to Equation (3.8).

Step 3: The value obtained for n is 11, as the first 11 principal components explain 99.7% of the variance in the PSD (see the blue continuous line in Figure 3.9; notice that $\delta = 0.997$ – Table 3.2).

Step 4: j is set to 1, and the iterative procedure for the selection of the n_0 components starts.

Steps 5 – 6: The 160 "healthy" data records forming Θ_0, along with the 215 "damaged" data records forming Θ_d, are used in the baseline phase (also see Table 3.1). In Figure 3.10(a) the behaviour of the first selected component is shown ($j = 1$), and then significant improvement is achieved with the inclusion of the second component ($j = 2$) (Figure 3.10(b)). The main objective is to maximize the distance between the "healthy" data records and the "damaged" ones. In Figure 3.10(c) an intermediate step is shown, with the final selection depicted in Figure 3.10(d). In this case it may be seen that all "healthy" data records have distances lower than those of the "damaged" data records, which is the desirable behaviour. Note that in all subfigures of Figure 3.10, "healthy" data records are indicated in blue, whereas "damaged" data records are indicated in red (damage 1) or green (damage 2). These three groups are separated by dashed vertical lines. Data records are ordered in such a way as to correspond to decreasing temperature. Also dotted vertical lines are included in the healthy and damage 2 cases to distinguish

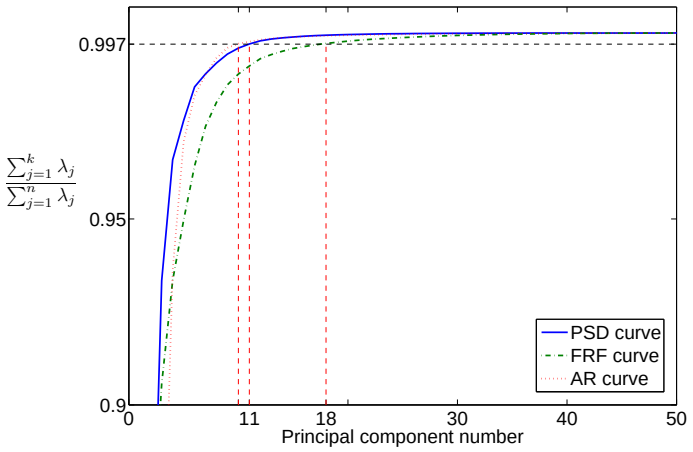

Figure 3.9: Baseline phase – determination of $\underline{n}$ for each method. The principal component number is represented on the horizontal axis, and the fraction of variance cumulatively explained by each and all previous components is depicted by the curve (blue solid line for the PSD based method, green dashed line for the FRF based method, red dotted line for the AR based method). The selected δ and the resulting $\underline{n}$ are indicated by the horizontal and vertical dashed lines, respectively.

the cases without water sprayed from the ones in which water has been sprayed. The data record corresponding to the maximum distance from "healthy" data records and the data record corresponding to the minimum distance from the "damaged" ones is color filled since these are the values used in the computation of each R_j. In Figure 3.11(a) the R_j ratios are shown for a few iterations. On the horizontal axis $n - \underline{n} = 40$ (from the 12^{th} till the 51^{st}) components are analyzed. In the case $j = 13$ $R_{13}(b(13)) = R_{12}(b(12))$, so the 13–th component is not included. In this case n_0 is set to 12 ($n_0 = 12$) and the process ends. The cases $j = 1, 5, 10, 12$ are shown. The selected components are marked with a solid blue circle.

Step 7: The matrix $\mathbf{U}_{n_0}$ is constructed and new transformed feature vectors are to be computed per Equation (3.17).

Inspection phase

Damage detection results with the selected principal components are shown for data records from the inspection phase (which are different from those used in the baseline phase – the cross–validation principle; also see Table 3.1) in Figure 3.12(a) . The first

1120 data records are healthy time series (35 for every temperature available with and without water), with 735 without water and the next 385 with water; the next 1505 data records correspond to damaged cases (also 35 data sets for every damage at specific temperatures and with water sprayed when available), so the first 385 correspond to damage 1, the next 735 to damage 2 without water and the last 385 to damage 2 with water sprayed. Healthy, damage 1, and damage 2 cases are separated by dashed vertical lines, the difference between water sprayed and not sprayed is made by a dotted line for the healthy and damaged 2 cases. The squared Mahalanobis distance is represented on the vertical axis. Overall, 15 false alarms and 13 undetected damages are obtained (1 corresponding to damage 1 and 12 to damage 2).

The non–parametric FRF magnitude based method

The method's selected parameters are provided in Table 3.2. The initial feature vector is obtained by means of Equation (3.5b). The steps are described in the sequel using the vibration response position Y2.

Baseline phase

Steps 1–2: As in the previous method.

Step 3: The value obtained for n is now 18, which is higher larger than in the previous method. This reflects the fact that the first 18 principal components explain 99.7% of the variance present in the FRF magnitude, and is also depicted in Figure 3.9 (green dashed line).

Step 4: Iteration index j is set to 1.

Steps 5–7: The intermediate results from these steps are shown in Figure 3.13, which is analogous to Figure 3.10. For this case the value obtained for n_0 is 13. Now, in Figure 3.11(b) the cases $j = 1, 5, 10, 13$ are shown. Again for the baseline data records a perfect separation of both sets is achieved with the final selection of components. It may be observed that the separation is better for the PSD based scheme for the baseline data records, as can be seen by the higher value of R_j obtained in Figure 3.11(a) with respect to the one obtained in 3.11(b). This can also be observed by comparing Figure 3.10(d) with Figure 3.13(d).

Inspection phase

The obtained damage detection results are presented In Figure 3.12(b). In this case a total number of 5 false alarms and 15 undetected damages are obtained (1 corresponding

to damage 1 and 14 to damage 2). The number of false alarms is thus reduced, although that of undetected damages is slightly increased.

The parametric AR based method

The specific values of the method's parameters are provided in Table 3.2. The model order selected based on the BIC criterion and model validation is $n_a = 200$. This order is kept common for all models (each one corresponding to each one of the vibration response measurement positions Y1, Y2, Y3, Y4).

The initial feature vector is chosen to consist of the first $n = 50$ parameters (Equation (3.5c)). Note that like with the previous methods, for proper covariance matrix estimation ρ_0 should be higher than n. The steps are described in the sequel using the vibration response position Y2.

Baseline phase

Steps 1 – 2: As in the previous methods.

Step 3: The value obtained for n is 10, which reflects the fact that the first 10 principal components explain 99.7% of the variance in the AR parameters (see the red dotted line in Figure 3.9).

Step 4: Iteration index j is set to 1.

Steps 5 – 7: The intermediate results from these steps are shown in Figure 3.14, which is analogous to Figures 3.10 and 3.13. For this case the value obtained for n_0 is 13 (as in the FRF method). The cases $j = 1, 5, 10, 13$ are presented in Figure 3.11(c). Like before, a perfect separation of the sets is achieved with the final selection of components; in fact this separation in much better with the present (AR based) method as may be observed by the higher value of R_j obtained in Figure 3.11.

Inspection phase

The obtained damage detection results are presented in Figure 3.12(c). In this case a total number of 4 false alarms and no undetected damages are obtained. Consistent with this improved performance is the fact that the distance between the "healthy" and "damaged" data records is quite higher than those corresponding to the two non–parametric (PSD and FRF based) methods.

Summary results and discussion

Summary damage detection results by all three methods and for each of the Y1, Y2, Y3, Y4 vibration measurement positions are provided in Table 3.3. It is interesting that the larger damage (D2) appears slightly less detectable than the smaller (D1) damage. Yet, this is probably due to the fact that – unlike with D1 – two cases (associated with the presence on no presence of sprayed water) are associated with D2 (refer to Table 3.1).

Method	*Sensor*	*False alarm rate*	*Undetected damage rate*	
			D1	D2
PSD	1	2/1120 (0.2%)	0/385 (0.0%)	13/1120 (1.2%)
based	2	15/1120 (1.3%)	1/385 (0.3%)	12/1120 (1.1%)
method	3	7/1120 (0.6%)	4/385 (1.0%)	22/1120 (2.0%)
	4	12/1120 (1.1%)	0/385 (0.0%)	0/1120 (0.0%)
FRF	1	5/1120 (0.5%)	0/385 (0.0%)	35/1120 (3.1%)
based	2	5/1120 (0.5%)	1/385 (0.3%)	14/1120 (1.2%)
method	3	3/1120 (0.3%)	0/385 (0.0%)	0/1120 (0.0%)
	4	1/1120 (0.1%)	0/385 (0.0%)	0/1120 (0.0%)
AR	1	3/1120 (0.3%)	0/385 (0.0%)	0/1120 (0.0%)
based	2	4/1120 (0.4%)	0/385 (0.0%)	0/1120 (0.0%)
method	3	0/1120 (0.0%)	0/385 (0.0%)	0/1120 (0.0%)
	4	6/1120 (0.6%)	0/385 (0.0%)	0/1120 (0.0%)

Table 3.3: Summary of the damage detection results (inspection data records only). All three methods (PSD, FRF, AR) employing a single vibration response sensor (Y1, Y2, Y3, Y4) at a time.

Comparing the results obtained by the methods (Figure 3.12), it is observed that all three perform very well, with the parametric method performing best. Indeed, it may be noted that the discrepancy between healthy and damaged data records is higher for the parametric method. Also, for this method and all vibration response measurement positions, there are no undetected damage cases at all, while the false alarm rate is no more than 0.6%; in fact it may be made zero with a small adjustment of the threshold.

Then, restricting attention to the two non–parametric methods, it may be observed that their performance is very good and comparable. Overall, it may be said that the FRF based method performs slightly better – which is expected as excitation information is additionally used – but the improvement is not significant. The undetected damage rate

does not exceed 3.1% for the FRF based method and 2.0% for its PSD based counterpart. On the other hand the false alarm rate does not exceed 0.5% for the FRF based method and 1.3% for its PSD based counterpart.

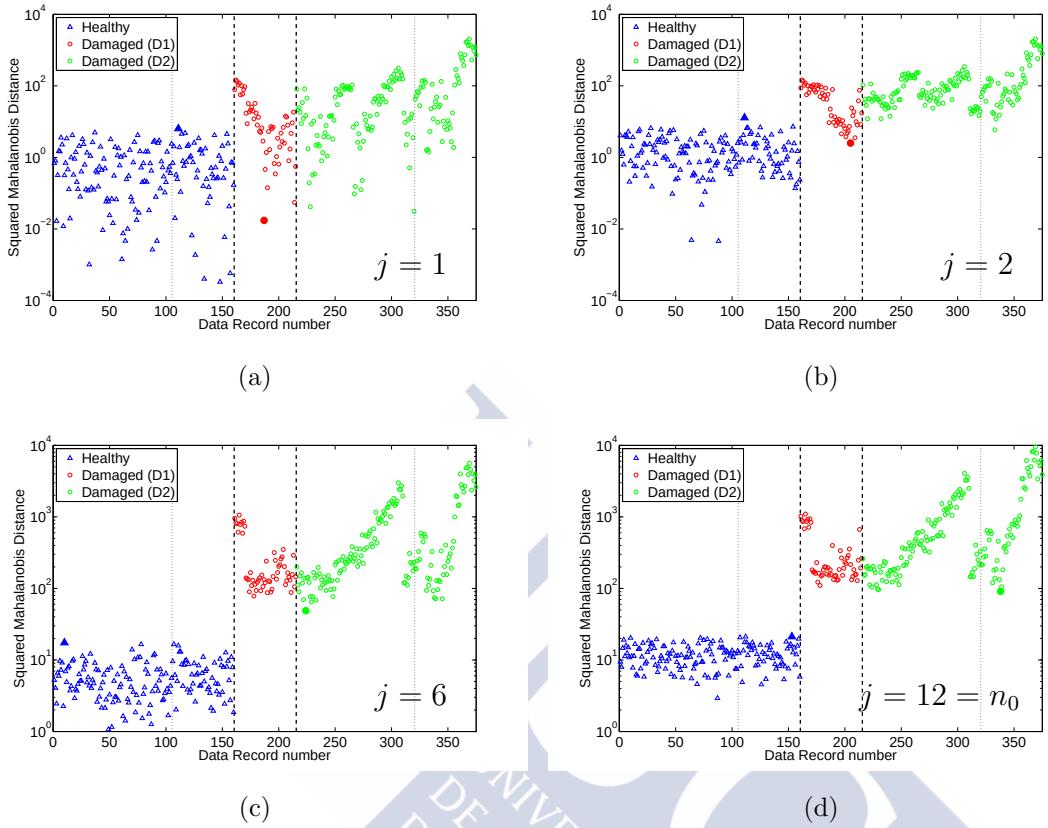

Figure 3.10: PSD based method – baseline phase (pictorial representation of Steps 5–6 in selecting the principal components to be included): Squared Mahalanobis distance from the various ("healthy" and "damaged") data records to the "healthy" set. The first 160 data sets (blue triangles) correspond to the healthy blade (the first 105 without water sprayed, the next 55 with water sprayed, separated by dotted vertical lines). The next 55 (red circles) correspond to damage 1 and the last 160 (green circles) to damage 2 (also here the first 105 without water sprayed, the next 55 with water sprayed, separated by dotted vertical lines). The three main groups are distinguished by dashed vertical lines. The data record corresponding to the maximum distance among all "healthy" data records to the reference set Θ_0 is designated by a solid blue triangle. The data record corresponding to the minimum distance among all "damaged" data records to the reference set Θ_0 is designated by a solid red or green circle. (a) One principal component included, (b) two principal components included, (c) intermediate step with six principal components included, (d) final selection of $n_0 = 12$ principal components.

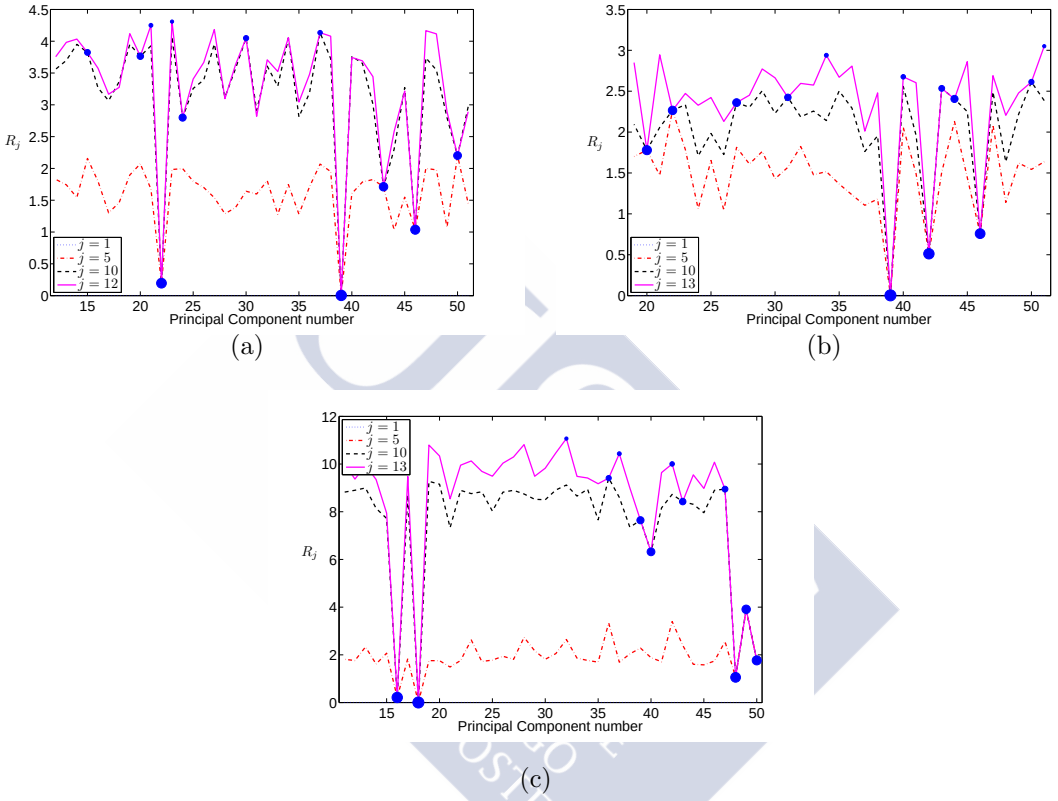

Figure 3.11: Baseline Phase: The ratio R_j computed for different iterations in each one of which a new principal component is added. The blue solid circles designate the principal component chosen for maximizing the ratio R_j at each step (in decreasing size according to the order in which they have been chosen). (a) PSD based method, (b) FRF based method, and (c) AR based method.

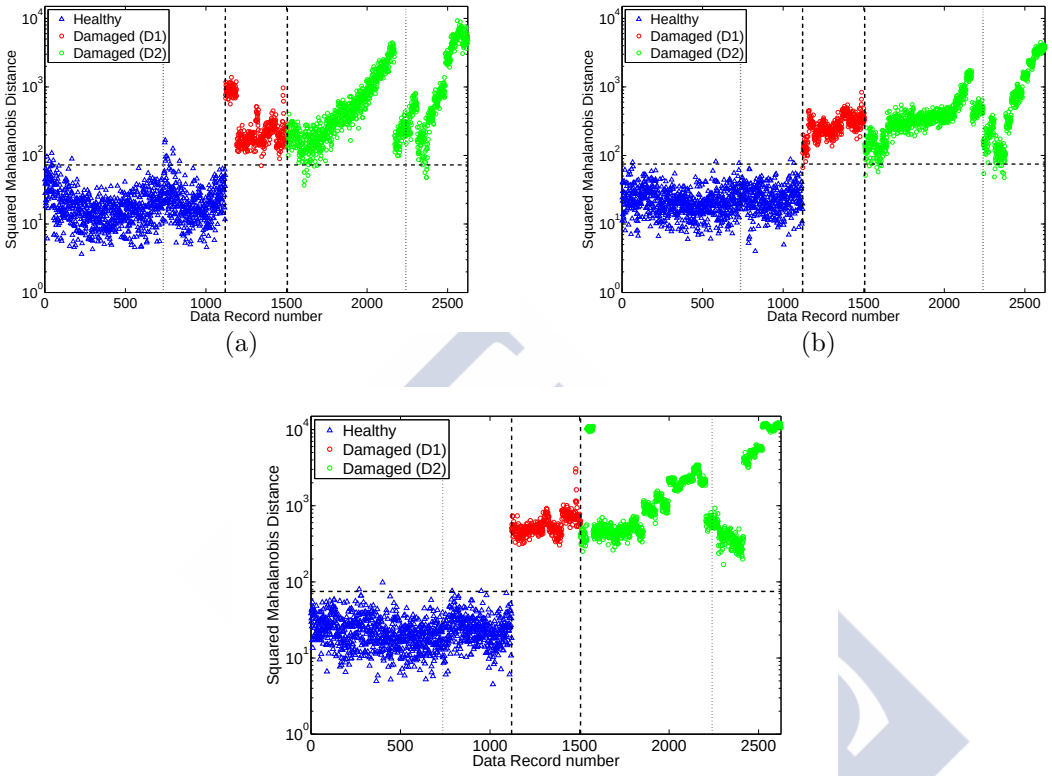

Figure 3.12: Inspection Phase – all methods: Damage detection results for data records from the inspection phase based on sensor position Y2 (false alarm probability $\alpha = 10^{-10}$). The first 1120 data records (blue triangles) correspond to the healthy condition, the next 385 record (red circles) correspond to damage 1, whereas the remaining 1120 records (green circles) correspond to damage 2. Dashed vertical lines distinguish the three different conditions, whereas dotted vertical lines separate the data records without water sprayed (first 735) from the ones with water sprayed (next 385). The threshold corresponding to the selected α is designated by the dashed horizontal line. (a) PSD based scheme with $n_0 = 12$ principal components, (b) FRF based scheme with $n_0 = 13$ principal components, (c) AR based scheme with $n_0 = 13$ principal components.

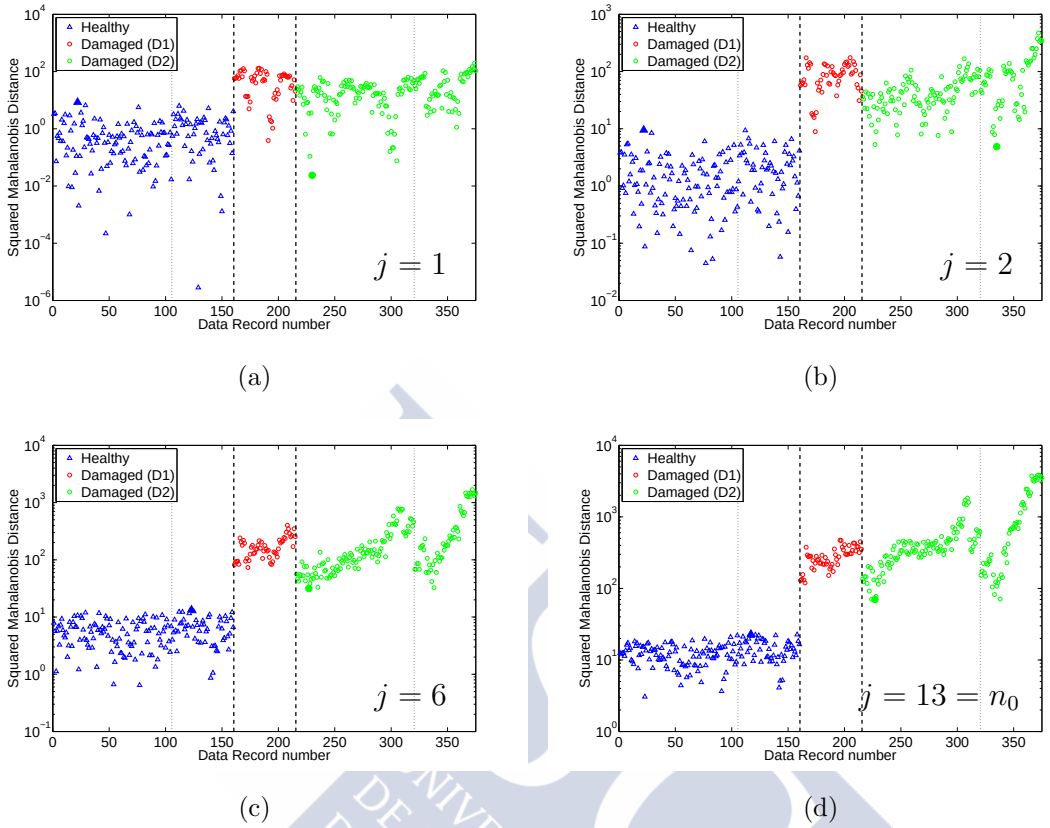

Figure 3.13: FRF based method – baseline phase (pictorial representation of Steps 5–6 in selecting the principal components to be included): Squared Mahalanobis distance from the various ("healthy" and "damaged") data records to the "healthy" set. The first 160 data sets (blue triangles) correspond to the healthy blade (the first 105 without water sprayed, the next 55 with water sprayed, separated by dotted vertical lines). The next 55 (red circles) correspond to damage 1 and the last 160 (green circles) to damage 2 (also here the first 105 without water sprayed, the next 55 with water sprayed, separated by dotted vertical lines). The three main groups are distinguished by dashed vertical lines. The data record corresponding to the maximum distance among all "healthy" data records to the reference set Θ_0 is designated by a solid blue triangle. The data record corresponding to the minimum distance among all "damaged" data records to the reference set Θ_0 is designated by a solid red or green circle. (a) One principal component included, (b) two principal components included, (c) intermediate step with six principal components included, (d) final selection of $n_0 = 13$ principal components.

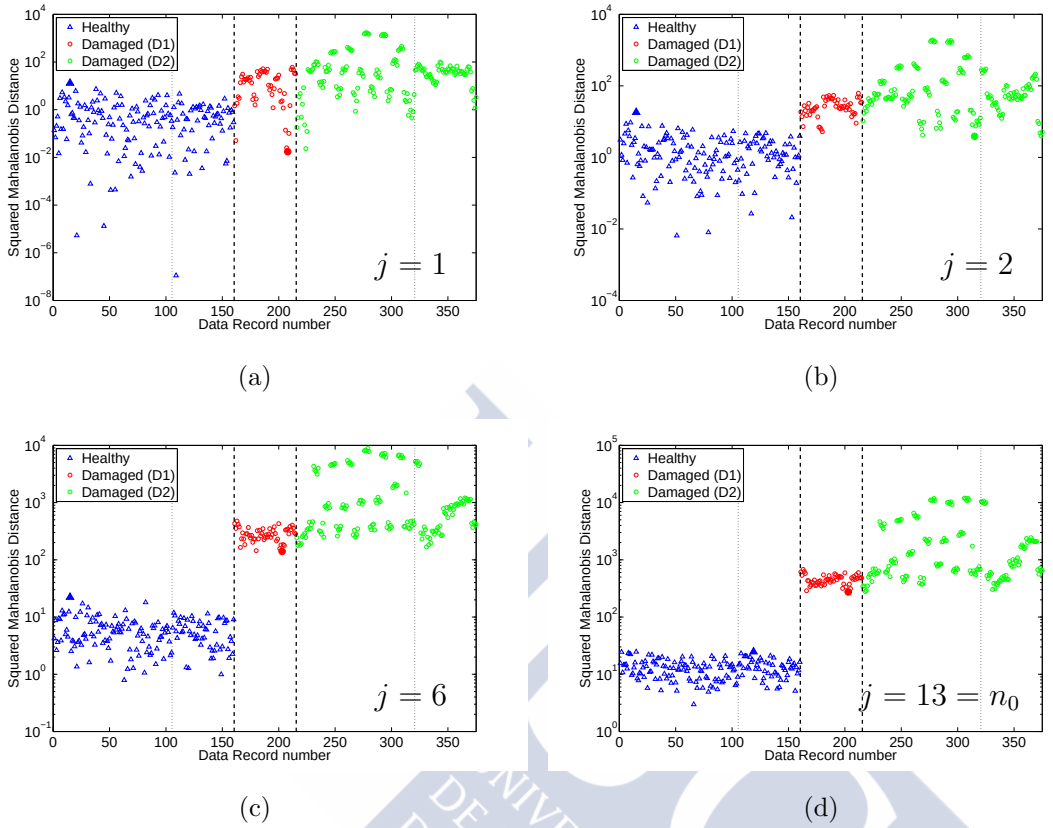

Figure 3.14: AR parameter based method – baseline phase (pictorial representation of Steps 5–6 in selecting the principal components to be included): Squared Mahalanobis distance from the various ("healthy" and "damaged") data records to the "healthy" set. The first 160 data sets (blue triangles) correspond to the healthy blade (the first 105 without water sprayed, the next 55 with water sprayed, separated by dotted vertical lines). The next 55 (red circles) correspond to damage 1 and the last 160 (green circles) to damage 2 (also here the first 105 without water sprayed, the next 55 with water sprayed, separated by dotted vertical lines). The three main groups are distinguished by dashed vertical lines. The data record corresponding to the maximum distance among all "healthy" data records to the reference set Θ_0 is designated by a solid blue triangle. The data record corresponding to the minimum distance among all "damaged" data records to the reference set Θ_0 is designated by a solid red or green circle. (a) One principal component included, (b) two principal components included, (c) intermediate step with six principal components included, (d) final selection of $n_0 = 13$ principal components.

3.4 Conclusions

The problem of vibration–based damage detection under varying environmental conditions and uncertainty was considered, and a novel supervised PCA–type statistical methodology, employing data records from the healthy and damaged states of the structure under various conditions, was postulated. Unlike standard PCA–type methods in which a feature vector corresponding to the least important eigenvalues is formed in a single step, the methodology uses damaged–state data records to *sequentially* form a feature vector by appending a transformed scalar element at a time under the condition that it *optimally*, among all remaining elements, improves damage detectability. This leads to the formulation of feature vectors with optimized sensitivity to damage, and thus high overall damage detectability.

Three particular methods – incarnations of the methodology – were postulated within this framework: two non–parametric based on the PSD and FRF, and one parametric, based on AR modelling. Their laboratory validation and comparative assessment was based on an experimental case study focusing on damage detection on a scale wind turbine blade under varying temperature and the potential presence of sprayed water.

Damage detection performance was based on hundreds of experiments and was shown to be excellent, even with a single response sensor and a bandwidth of $20 - 2000$ Hz. The undetected damage and false alarm rates were minimal (mostly close to zero, with maximum values of around 3%) for all three methods and for any one of four response sensors.

USC
UNIVERSIDADE
DE SANTIAGO
DE COMPOSTELA

Chapter 4

Vibration–based damage diagnosis in wind turbine blades

4.1 Introduction

Damage detection, localization and characterization is collectively referred to as *damage diagnosis*. In vibrating structures including aerospace, mechanical, civil, and marine structures, damage diagnosis is of paramount importance for reasons associated with dynamic performance, operation, safety, and proper maintenance [27, 34].

In the *present chapter* the feasibility of damage diagnosis (detection and localization) is examined based on a single pair of limited and low bandwidth ($0 - 600\ Hz$) force excitation and vibration acceleration response signals. A data–based, statistical time series type, methodology is employed, with damage detection using a Frequency Response Function (FRF) based scheme, and damage localization based on a Functionally–Pooled AutoRegressive with eXogenous excitation (FP–ARX) scheme. The experiments are performed using a lab–scale blade and damage simulated by local mass addition at different locations (10 used in the baseline phase and additional 6 used exclusively for validation in the inspection phase).

The rest of this chapter is organized as follows: The damage diagnosis methodology is presented in section 4.2. The set–up, the damage scenarios and the experiments are presented in section 4.3. Damage diagnosis (detection and localization) results are presented in section 4.4, while the conclusions are summarized in section 4.5. A final section 4.6, with some extra figures is included.

4.2 The damage diagnosis methodology

The data–based, statistical time series type, methodology employs a Frequency Response Function (FRF) magnitude based scheme for damage detection [38], and a more elaborate Functionally–Pooled AutoRegressive with eXogenous excitation (FP–ARX) based scheme [95, 69] for damage localization.

From an operation viewpoint, the methodology consists of two phases: a *baseline (learning) phase* taking place only once (initially), and an *inspection phase* which is the actual diagnosis phase taking place periodically, continuously, or on demand. In the baseline phase a number of excitation and vibration response signal records corresponding to various health states of the blade are employed, while a single such pair representing the blade in its current (unknown health state) is used in each test case in the inspection phase. The two phases are described in the sequel.

4.2.1 Baseline phase

(a) Damage detection. Damage detection is based on changes caused by damage on the FRF magnitude. It requires the availability of both the force excitation and vibration response signals and uses the FRF magnitude, $|H(j\omega)|$, as its *characteristic quantity* (feature) – note that j stands for the imaginary unit, ω for frequency in rad/s, and $|\cdot|$ designates complex magnitude. The main idea is the comparison of the FRF magnitude $|H_u(j\omega)|$ of the current (unknown) state of the structure to that of the healthy structure $|H_h(j\omega)|$ [39].

The Welch–based FRF magnitude estimator is employed (Matlab function *tfestimate.m*). This estimator approximately follows (for long data records, $N \to \infty$) Gaussian distribution with mean coinciding with the true FRF magnitude and a specific variance [12, p. 338] that may be estimated based on the signal records [12, p. 196].

(b) Damage localization. In the baseline phase damage localization requires the modeling of the structural dynamics under damage at various locations, via a Functionally–Pooled AutoRegressive with eXogenous input (FP–ARX) type model [95]. Specifically an FP–ARX model is estimated based on a number of experiments, each one corresponding to damage at a specific location on the structure. In this study the blade is approximated as one–dimensional, hence each damage location is characterized by a single coordinate k in the range $[k_{\min}, k_{\max}]$ via the discretization $\{k_1, \ldots, k_M\}$.

The set of baseline experiments then provides a corresponding set of excitation–

response signal pairs (each signal being N samples long):

$$x_k[t], y_k[t], \qquad \text{with } t = 1, \ldots, N, \qquad k \in \{k_1, \ldots, k_M\}. \tag{4.1}$$

Based on this data set, a mathematical model representing the structural dynamics under any potential damage location is obtained in the form of an FP–ARX model. An FP–ARX$(n_a, n_b)_p$ model has the following structure:

$$y_k[t] + \sum_{i=1}^{n_a} a_i(k) \cdot y_k[t-i] = \sum_{i=0}^{n_b} b_i(k) \cdot x_k[t-i] + e_k[t], \tag{4.2a}$$

$$e_k[t] \sim \text{ iid } \mathcal{N}(0, \sigma_e^2(k)), \qquad k \in [k_{\min}, k_{\max}], \tag{4.2b}$$

$$a_i(k) \triangleq \sum_{j=1}^{p} a_{i,j} \cdot G_j(k), \qquad b_i(k) \triangleq \sum_{j=1}^{p} b_{i,j} \cdot G_j(k), \tag{4.2c}$$

with n_a, n_b designating the AutoRegressive (AR) and eXogenous (X) orders, respectively, $x_k[t]$, $y_k[t]$ the excitation and response signals, respectively, and $e_k[t]$ the innovations (one–step–ahead prediction error) signal that is a zero–mean white (serially uncorrelated) with variance $\sigma_e^2(k)$, uncorrelated with the corresponding excitation signal, but potentially cross–correlated with its counterparts from different experiments.

As Equation (4.2c) indicates, the AR and X parameters $a_i(k)$ and $b_i(k)$ are modeled as explicit functions of k by belonging to a $p-$dimensional functional subspace spanned by the (mutually independent) functions $G_1(k)$, $G_2(k)$, $\ldots$, $G_p(k)$ (*functional basis*). The functional basis presently consists of selected polynomials, like Chebyshev, Legendre, Jacobi, and so on. The constants $a_{i,j}$ and $b_{i,j}$ designate the AR and X *coefficients of projection*. It must be noted that the dimension p of the functional subspace could be different for the AR and X part, but in this study they are considered to be equal. A proper FP–ARX model is estimated based on a Least Squares type estimator – details in [95, 69].

4.2.2 Inspection phase

(a) Damage detection. Damage detection is based on the comparison of the FRF magnitude $|H_u(j\omega)|$ of the current (unknown) state of the structure to that of the healthy structure $|H_h(j\omega)|$ [38]. As the true FRF magnitudes are unknown, corresponding Welch–type estimates obtained in the baseline phase, $|\widehat{H}_h(j\omega)|$, and in the inspection (current) phase, $|\widehat{H}_u(j\omega)|$, along with their uncertainties, are used (notice that the hat designates estimator/estimate of the indicated quantity). Setting:

$$\delta|H(j\omega)| = |H_h(j\omega)| - |H_u(j\omega)|,$$

the following hypothesis testing problem is then set up:

$$\begin{array}{ll} H_o: & \delta|H(j\omega)| = 0 \qquad \text{(null hypothesis – healthy structure)} \\ H_1: & \delta|H(j\omega)| \neq 0 \quad \text{(alternative hypothesis – damaged structure).} \end{array} \tag{4.3}$$

The null (H_o – healthy structure), or alternative (H_1 – damaged structure), hypothesis is then accepted at the α (type I or false alarm) risk level (false alarm probability equal to α) through the statistic Z, as follows:

$$\begin{array}{rcl} Z = \left|\delta|\widehat{H}(j\omega)|\right| / \sqrt{2\widehat{\sigma}_o^2(\omega)} \leq Z_{1-\frac{\alpha}{2}} \quad (\forall\, \omega) & \Longrightarrow & H_o \text{ is accepted} \\ \text{Else} & \Longrightarrow & H_1 \text{ is accepted,} \end{array} \tag{4.4}$$

with $Z_{1-\alpha/2}$ designating the standard normal distribution's $1-\alpha/2$ critical point (Figure 4.1).

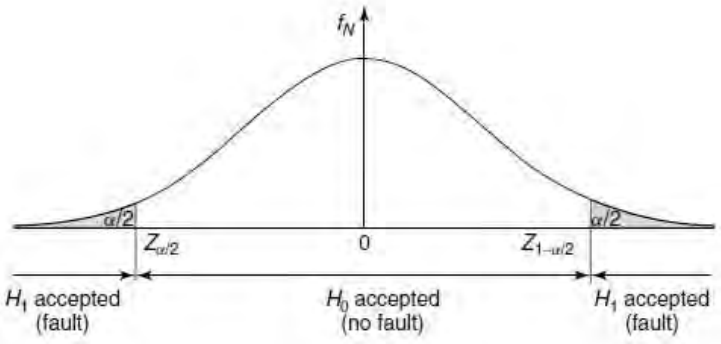

Figure 4.1: Statistical hypothesis testing based on a normal distributed statistic (two–tailed test).

(b) Damage localization. Damage localization is activated whenever the presence of damage is detected. The current excitation – response signals $x_u[t]$, $y_u[t]$, are then used in the following FP–ARX model form which is parametrized in terms of the damage

location k:

$$y_u[t] + \sum_{i=1}^{n_a} a_i(k) \cdot y_u[t-i] = \sum_{i=0}^{n_b} b_i(k) \cdot x_u[t-i] + e_u[t], \tag{4.5a}$$

$$e_u[t] \sim \text{ iid } \mathcal{N}(0, \sigma^2_{e_u}(k)) \tag{4.5b}$$

$$a_i(k) \triangleq \sum_{j=1}^{p} a_{i,j} \cdot G_j(k), \qquad b_i(k) \triangleq \sum_{j=1}^{p} b_{i,j} \cdot G_j(k), k \in [k_{\min}, k_{\max}] \tag{4.5c}$$

The functional parameters of this model (including the coefficients of projection) are those obtained in the baseline phase. The current damage location k and the residual variance $\sigma^2_e(k)$ may be then estimated as:

$$\widehat{k} = \arg\min_k \sum_{t=1}^{N} e_u^2[t], \qquad \widehat{\sigma}^2_{e_u}(\widehat{k}) = \frac{1}{N} \sum_{t=1}^{N} e_u^2[t, \widehat{k}]. \tag{4.6}$$

The Nonlinear Least Squares (NLS) estimator (refer to [77, pp. 327–329] on such estimators) of the first expression is presently realized via constrained nonlinear optimization (Sequential Quadratic Programming – SQP, Matlab function *fmincon.m* – further details in [69]).

4.3 The experimental set–up, the damages and the experiments

The lab–scale wind turbine blade (length 0.71 m including the clamping, maximum width 0.135 m, mass 0.646 kg) is shown in the drawing of Figure 4.2(a). It is clamped as a cantilever on a steel base via 3 bolts (torque 5 N·m) and excited by a shaker (Figures 4.2(b) & 4.3).

Each damage is simulated as a small added mass (6 g, corresponding to 0.9% of the blade mass). Ten evenly spaced (every 6 cm) damage locations are considered along the blade's central axis in the baseline (learning) phase. Six additional locations (four on the central axis and two close to the trailing edge) are considered in the inspection (testing) phase for purposes of methodology validation (*cross validation principle*) – Figure 4.2(a). A detailed description of each damage is provided in Table 4.1.

The excitation is random, stationary, approximately white, force measured via an impedance head (PCB M288D01, sensitivity 98.41 mV/lb). The resulting vibration responses are measured via four lightweight accelerometers located at Points Y1, Y2, Y3,

Damage	*Distance from tip (cm)*	*Location*
Position 1	6	Central axis
Position 2	12	Central axis
Position 2–3	15	Central axis
Position 3	18	Central axis
Position 4	24	Central axis
Position 4 bis	24	Trailing edge
Position 4–5	26	Central axis
Position 5	30	Central axis
Position 5–6	33	Central axis
Position 6	36	Central axis
Position 7	42	Central axis
Position 8	48	Central axis
Position 9	54	Central axis
Position 9 bis	55.1	Near trailing edge
Position 9–10	57	Central axis
Position 10	60	Central axis

Table 4.1: Description of the considered damage locations. The ten baseline locations are shown with white background, whereas the remaining locations are shown with grey shaded background, these are used exclusively in the inspection phase.

and Y4. It should be stressed that only a *single* vibration response is used for damage diagnosis at each time. All signals are collected via two SigLab modules at an initial sampling frequency of $f_s = 5120$ Hz and are subsequently low–pass filtered in the range $0 - 640$ Hz before resampling at $f_s = 1280$ Hz, since enough frequency content is present up to 600 Hz. The resulting signal length is $N = 8192$ samples (6.4 s) – details are provided in Table 4.2.

A total number of 44 experiments are carried out per each health state of the blade (healthy and damaged). For the health states considered in the baseline phase, one is reserved for this baseline phase and the other 43 are used in the inspection phase (notice that no experiments are carried out in the baseline phase for the six additional damage locations) – see Table 4.2.

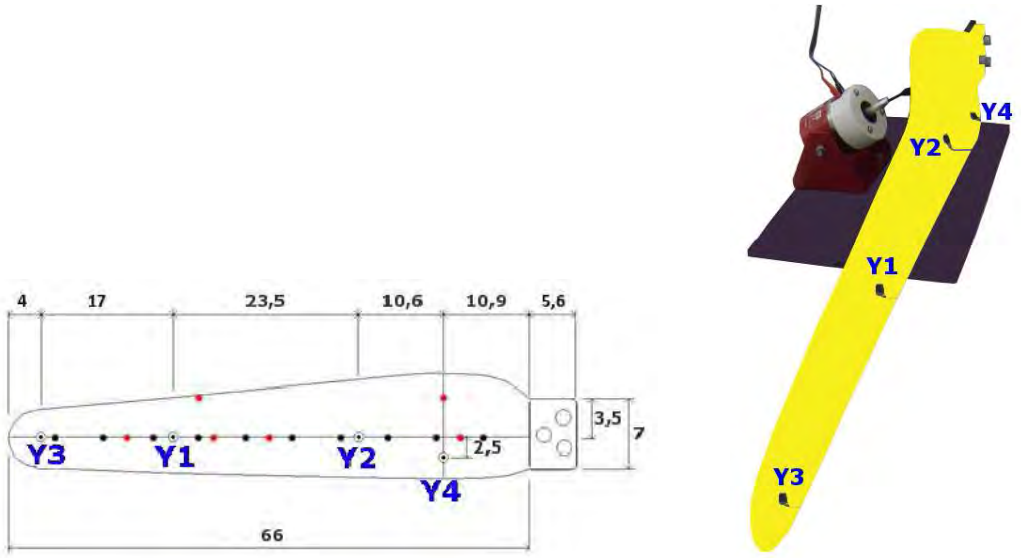

(a) (b)

Figure 4.2: The lab–scale blade. (a) Drawing showing the ten damage locations of the baseline phase (in black) and the six locations of the inspection phase (in red). Y1–Y4 designate the random vibration measurement locations. (b) Photo of the experimental set–up showing the clamping, the shaker, and the acceleration measurement locations.

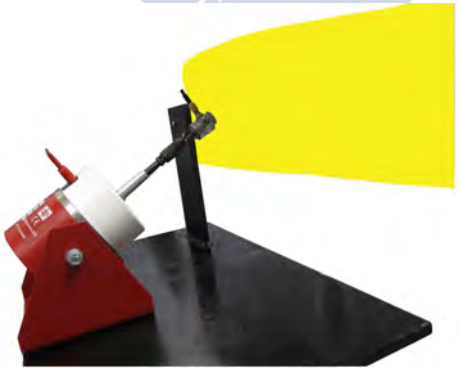

Figure 4.3: Detail of the experimental set-up: the exciter with part of the blade.

Blade Health State	*Number of experiments per damage location*		*Total number of experiments (all locations)*	
	Baseline	*Inspection*	*Baseline*	*Inspection*
Healthy	1	43	1	43
Each damage baseline location	1	43	10	430
Each damage additional location	0	44	0	264
Initial sampling frequency $f_s = 5\ 120$ Hz				
Digital low pass filtering: Chebyshev Type II, 10^{th} order, bandwidth $0 - 640\ Hz$				
Final sampling frequency $f_s = 1280\ Hz$				
Final signal length $N = 8192$ samples (6.4 s)				

Table 4.2: Numbers of experiments and vibration response signal details.

4.4 Damage detection and localization results

In this chapter results obtained from the vibration response sensor Y4 are presented, since for the other three measured positions some detectability problems were observed with the used damage detection methodology.

Before proceeding, comparisons between the estimated FRF magnitude curves for the healthy and damaged blades are presented in Figure 4.4 (estimation details in the upper part of Table 4.3). The purpose of this is to assess the effects of the each specific damage used on the blade dynamics. As seen from the two cases (two damage locations) considered in Figure 4.4, the effects of damage on the dynamics are limited within the considered frequency range. This indicates that the considered level of damage is rather "small", with the detection and localization problems being thus challenging.

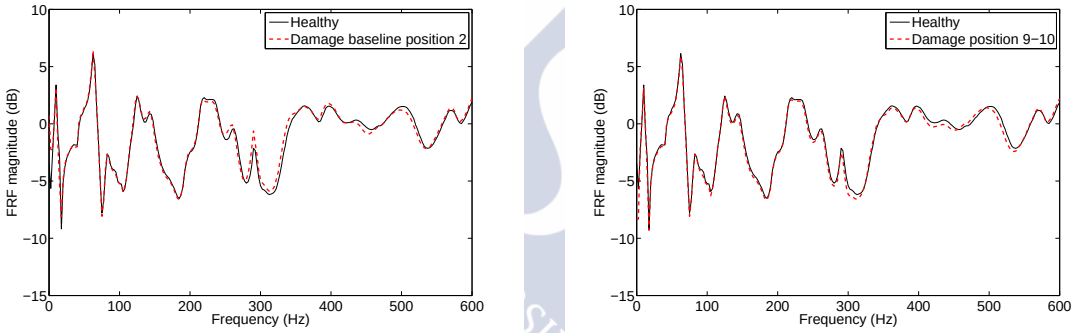

(a) (b)

Figure 4.4: Assessment of the effects of the considered damage on the blade dynamics. FRF magnitude of the healthy blade (solid blue line) compared to that of the damaged blade (dashed red line) for two distinct damage locations: (a) location 2, (b) location 9–10. (Welch–based FRF estimates using the excitation and Y4 vibration response signals).

(a) Baseline phase. The excitation–vibration response (Y4 sensor) blade dynamics are first identified for the healthy structural state. The corresponding non–parametric FRF estimate is obtained via Welch spectral estimation, with the selections indicated in the upper part of Table 4.3. Parametric ARX models, of the ARX(n, n) form for increasing order n, are also fitted to a pair of excitation – response signals of the healthy blade. Model order selection is based on a number of criteria, including the Bayesian Information Criterion (BIC) [77] shown in Figure 4.5(a). The selected model order, $n = 120$, is indicated by a vertical arrow. Model validation results using the model residual (one–

Damage detection (baseline & inspection phases)	
Estimation method	Welch
Window type	Hamming
L (segment length)	1024 samples
Overlap	0 samples
K (number of segments)	8
risk level α	10^{-10}

Damage localization (baseline phase)	
Method	FP–ARX based
Estimated model	FP–ARX(120,120)$_{p=10}$
Projection coefficients	2 400
Estimation method	Ordinary Least squares (OLS)
Samples per parameter	37.6
Condition number	1.6826×10^{12}
Functional basis	Shifted Chebyshev II polynomials $G_1, \ldots, G_{10}$

Table 4.3: Damage detection and localization estimation details.

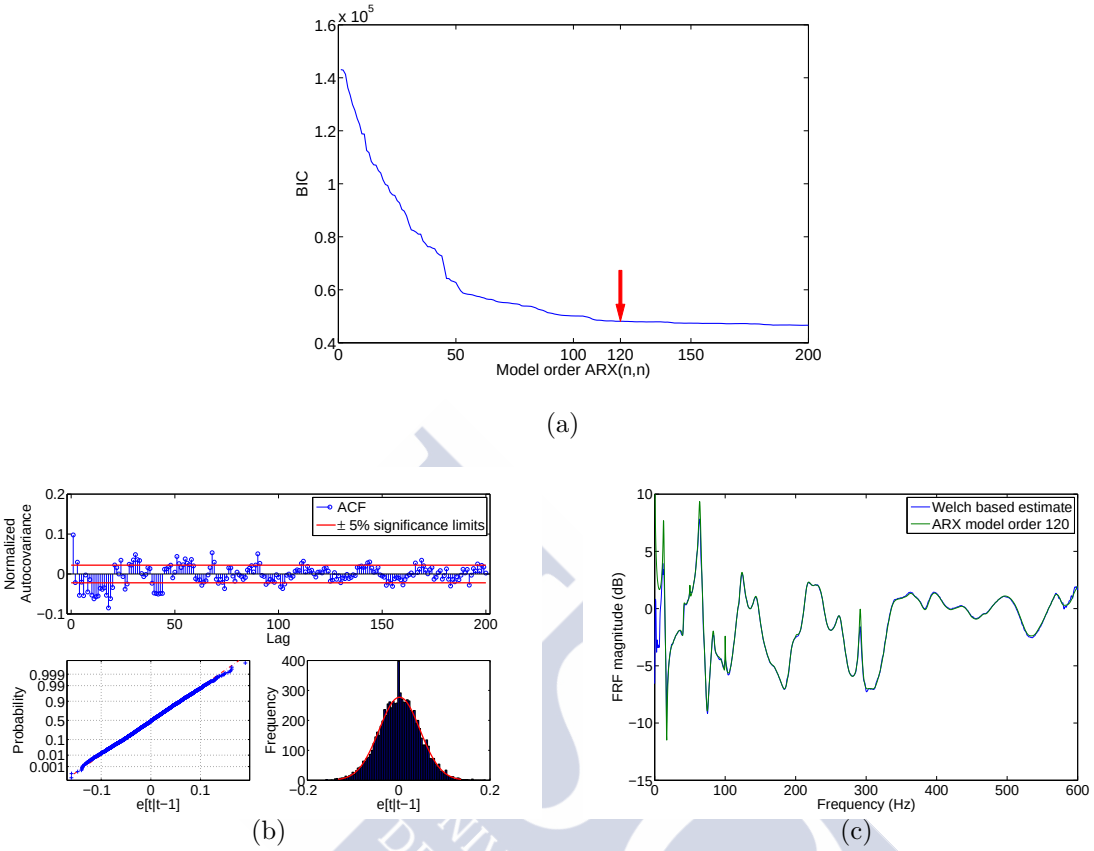

Figure 4.5: Baseline phase – parametric ARX modeling of the healthy structural dynamics: (a) BIC versus ARX model order; (b) whiteness and Gaussianity tests on the model residuals; (c) comparison of the ARX–based FRF magnitude with its non–parametric (Welch–based) counterpart. (Y4 response sensor.)

step–ahead prediction error) sequence (normalized autocovariance or correlogram with 5% significance limits, normal probability plot, and histogram) are shown in Figure 4.5(b). A comparison of the non–parametric Welch based FRF magnitude estimate with that derived from the estimated AR(120) model is presented in Figure 4.5(c), from which very good agreement (except for very low frequencies) is observed.

For damage localization, an FP–ARX model is next estimated based on force excitation and vibration response (sensor Y4) signals obtained from the damaged blade, with the damage located at 10 different baseline locations (those shown in grey shaded background in Table 4.1). Shifted Chebyshev polynomials of the second kind [84, Chapter 18], see Appendix A.1 for more details, are used, with the selected model being an

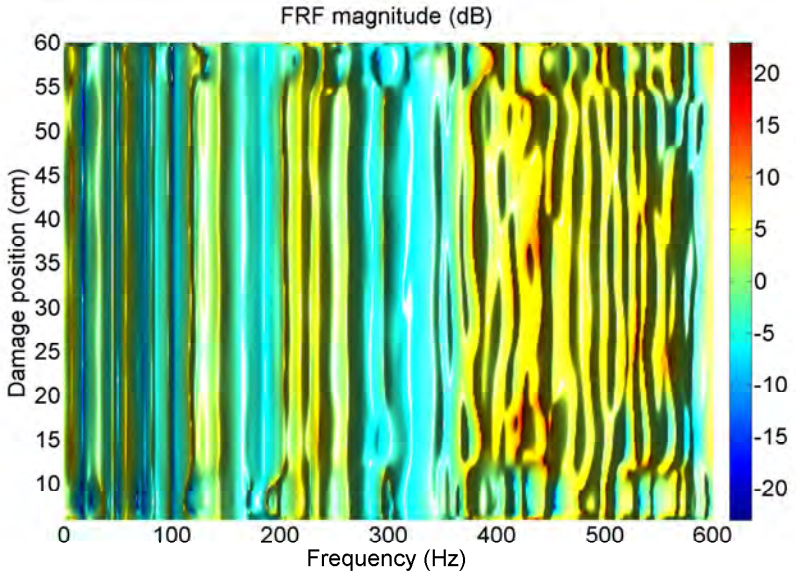

Figure 4.6: Baseline phase: FP–ARX(120,120)$_{p=10}$ model based FRF magnitude versus frequency and damage location.

FP–ARX(120,120)$_{p=10}$. Estimation details are shown in the lower part of Table 4.3.

The FP–ARX(120,120)$_{p=10}$ model based FRF magnitude versus frequency and damage location is depicted in Figure 4.6. Evidently, the FRF magnitude barely depends on damage location at low frequencies, with some dependence observed at higher frequencies.

(b) Inspection phase. Damage detection results are presented in Figure 4.7 for 43 healthy and 694 damage experiments – the reader is referred to Table 4.1 for details on the damage locations and Table 4.2 for explanations on the number of conducted experiments. The results are excellent, with no false alarms or missed damage cases observed.

Damage localization is based on the optimization indicated by Equation (4.6). In order to avoid local extrema, an exhaustive search is first implemented (with a coarse grid), and SQP (Sequential Quadratic Programming) (MATLAB *fmincon.m* function) is subsequently used for refinement around the already obtained initial optimum. Two examples of the cost function indicated in Equation (4.6) are provided in Figure 4.8; the first is a test case corresponding to damage location 2, and the second a test case corresponding to damage location 9–10 (only used in the inspection phase). In both cases the estimated damage location (cost function minimum) is indicated by a red arrow, while the actual damage location is indicated by the dashed vertical line. One may observe that

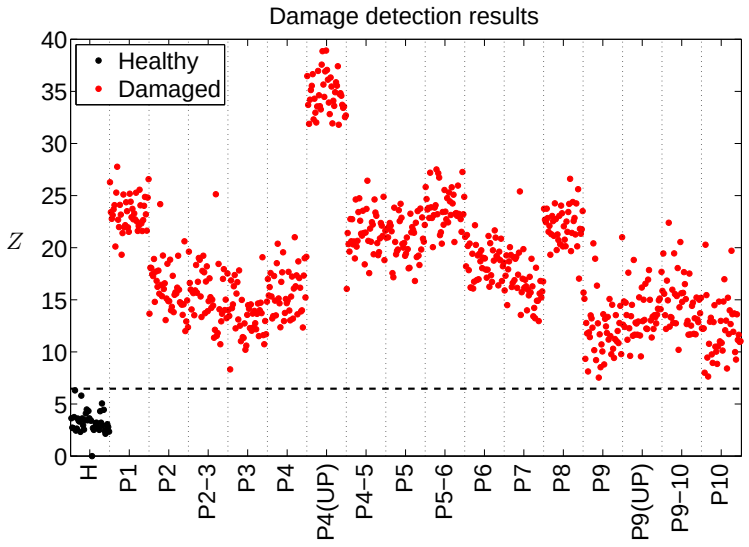

Figure 4.7: Inspection phase – damage detection results via the FRF magnitude based scheme: The test statistic versus the threshold (dashed horizontal line) for 43 healthy cases (black points) and 694 damage cases (red points). A damage is detected if the test statistic exceeds the threshold (risk level $\alpha = 10^{-10}$).

localization is effective in both cases, being perfect in the first case and with a small error in the second.

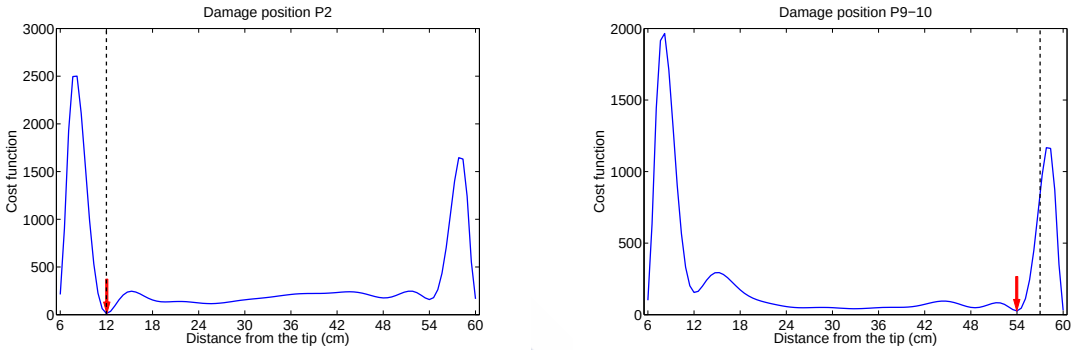

(a) (b)

Figure 4.8: Inspection phase – damage localization results for two test cases: (a) damage location 2, (b) damage location 9–10. In each case the cost function of Equation (4.6) versus damage location (in cm) is depicted. The estimated damage location corresponds to the cost function minimum, and is indicated by a red vertical arrow. The actual damage location is indicated by a dashed vertical line.

Summary localization results are presented in Figure 4.9 for a total number of 694 inspection experiments. The actual damage locations are indicated by dashed horizontal lines, while their estimated counterparts are indicated by black dots (data records also used in the baseline phase), blue triangles (on the blade's central axis and only used in the inspection phase), and red squares (off the blade's central axis and only used in the inspection phase). The results are quite accurate overall, with errors being lower than 5 cm in the vast majority of the cases. The damage localization errors are also depicted in Figure 4.10.

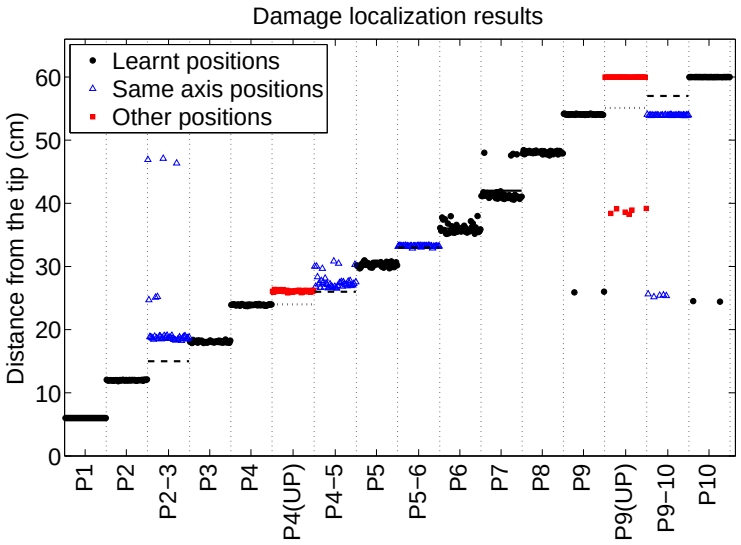

Figure 4.9: Inspection phase – summary damage localization results. Actual damage locations are indicated by dashed horizontal lines. Estimated locations are indicated by black dots (locations used in the baseline phase), blue triangles (on the blade's central axis and only used in the inspection phase), red squares (off the blade's central axis and only used in the inspection phase). [A total of 694 experiments.]

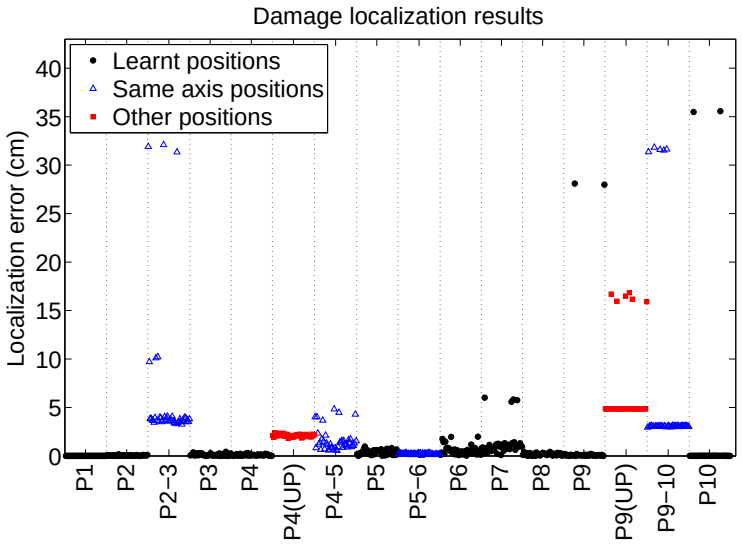

Figure 4.10: Inspection phase – summary damage localization errors. Localization errors are indicated by black dots (locations also used in the baseline phase), blue triangles (locations on the blade's central axis and only used in the inspection phase), red squares (locations off the blade's central axis and only used in the inspection phase). [A total of 694 experiments.]

4.5 Concluding remarks

The problem of damage diagnosis for wind turbine blades was considered via a single pair of force excitation and vibration response signals employed in the inspection phase. A data–based, statistical time series type methodology was employed, with damage detection using a Frequency Response Function based scheme, and damage localization a Functionally–Pooled AutoRegressive with eXogenous excitation (FP–ARX) based scheme. A high number of experiments was performed on a lab–scale blade and damage simulated by local mass addition at different locations. Despite the fact that a low frequency bandwidth $0-600Hz$ was employed, the results of the study indicated the feasibility of damage detection and localization. Damage detection was flawless, while damage precise localization was quite effective, with errors not exceeding 5 cm in the vast majority of the cases. The price to be paid for damage precise localization is the number of experiments required for identifying the Functionally–Pooled model in the baseline (learning) phase of the methodology. These experiments could be, alternatively, conducted numerically, using a high fidelity finite element model in the baseline phase.

4.6 Appendix A - Extra figures

In this section a 3D extra representations of Figure 4.6 is included in Figure 4.11 to make clearer the behavior.

Additionally along the document some reference figures for particular positions of the damage have been shown. In this last section, full detailed figures referred to all positions are shown regarding the FRF magnitude, Figures 4.12, 4.13 and 4.14, and the cost function representation, Figures 4.15, 4.16 and 4.17.

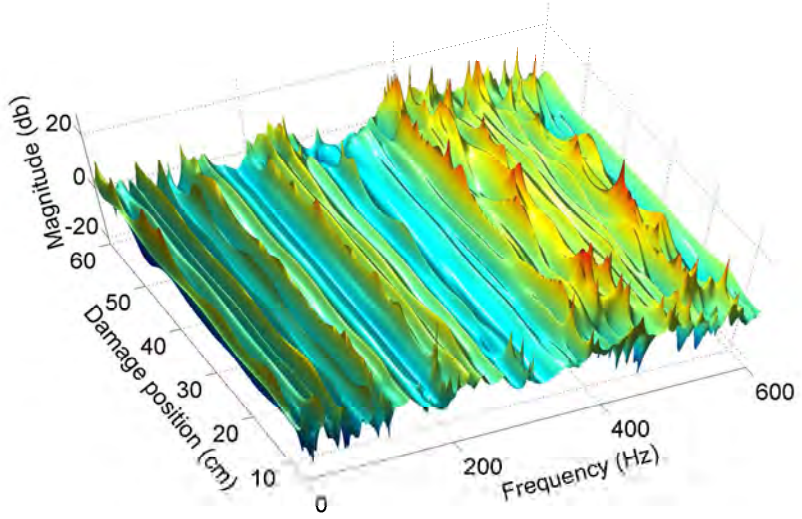

Figure 4.11: 3D FRF magnitude representation with respect to frequency and damage position.

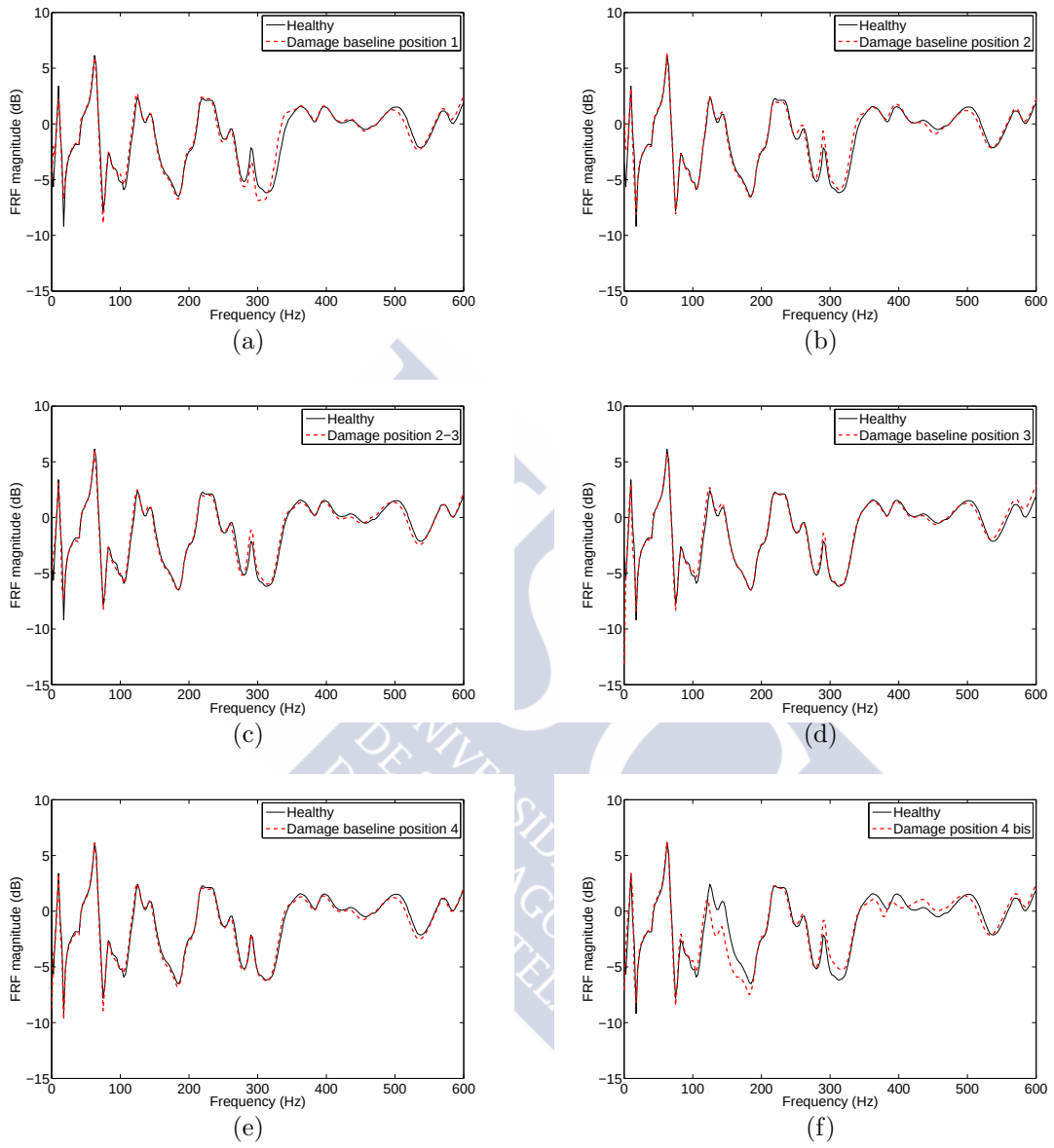

Figure 4.12: FRF magnitude representation. The black continuous line represents the healthy case, whereas the red dashed line represents a damaged case: (a) damage position 1 (baseline), (b) damage position 2 (baseline), (c) damage position 2–3 (inspection), (d) damage position 3 (baseline), (e) damage position 4 (baseline), (f) damage position 4bis (inspection).

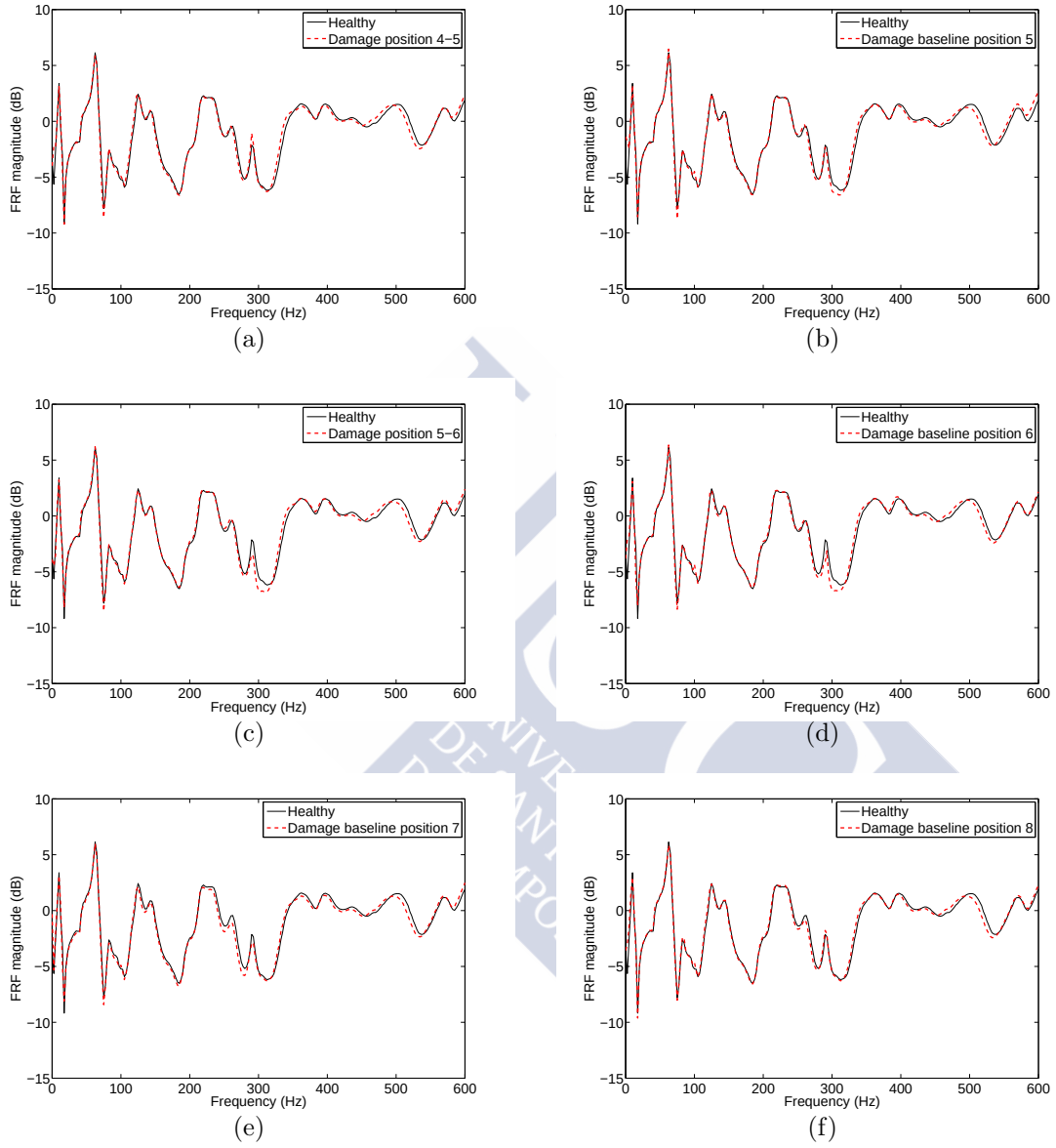

Figure 4.13: FRF magnitude representation. The black continuous line represents the healthy case, whereas the red dashed line represents a damaged case: (a) damage position 4–5 (inspection), (b) damage position 5 (baseline), (c) damage position 5–6 (inspection), (d) damage position 6 (baseline), (e) damage position 7 (baseline), (f) damage position 8 (baseline).

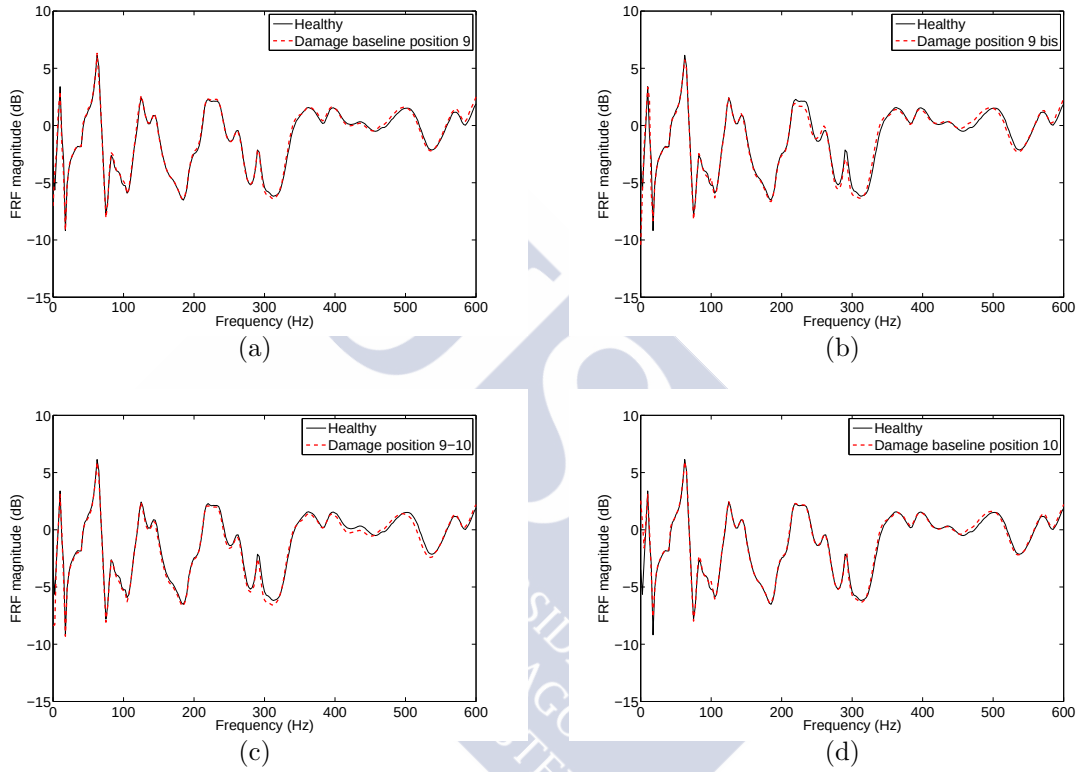

Figure 4.14: FRF magnitude representation. The black continuous line represents the healthy case, whereas the red dashed line represents a damaged case: (a) damage position 9 (baseline), (b) damage position 9bis (inspection), (c) damage position 9–10 (inspection), (d) damage position 10 (baseline).

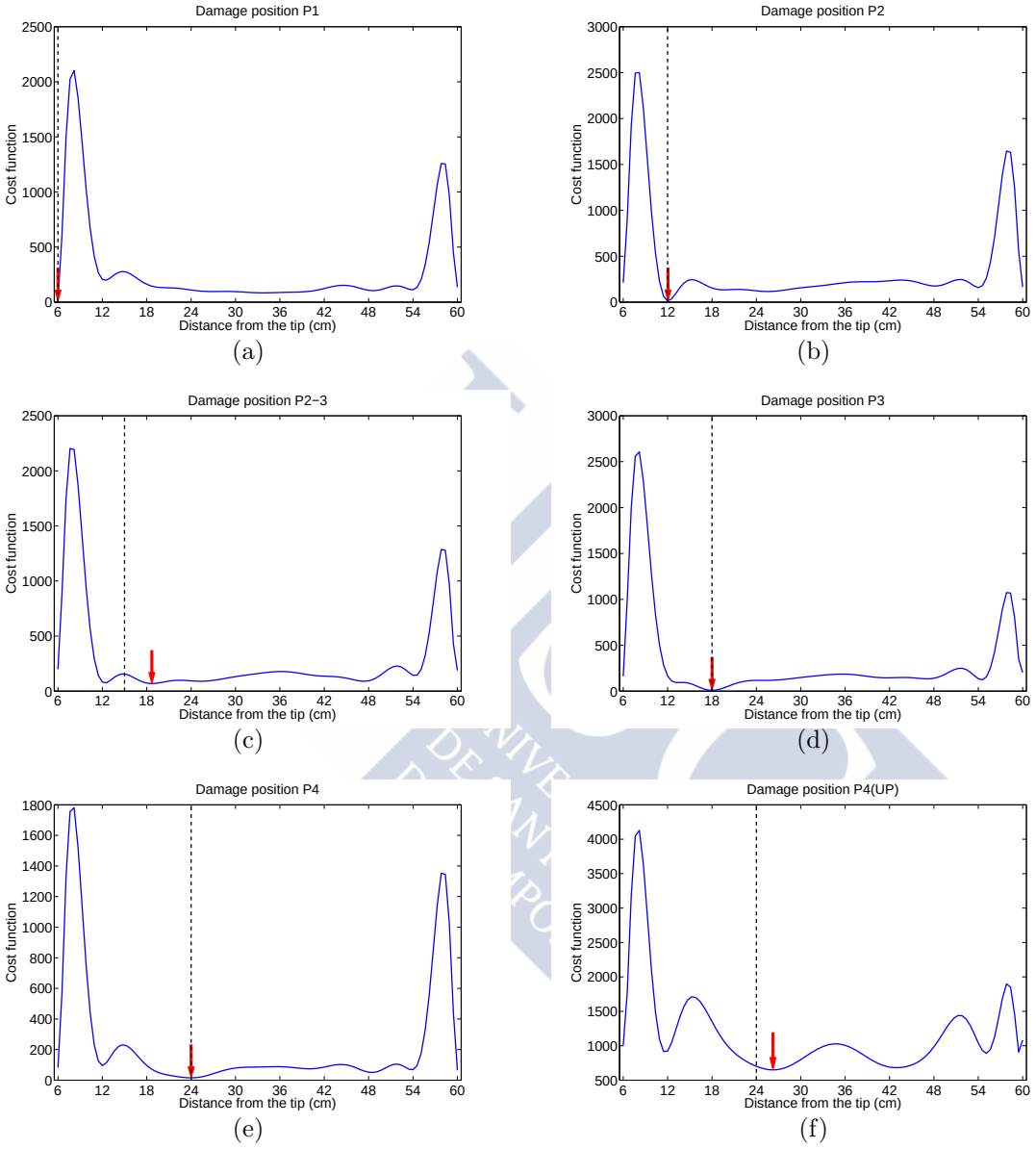

Figure 4.15: Cost function representation. The black vertical dashed line indicates the true position of the damage, the red arrow the minimum value obtained after exhaustive search and Matlab *fmincon.m*: (a) damage position 1 (baseline), (b) damage position 2 (baseline), (c) damage position 2–3 (inspection), (d) damage position 3 (baseline), (e) damage position 4 (baseline), (f) damage position 4bis (inspection).

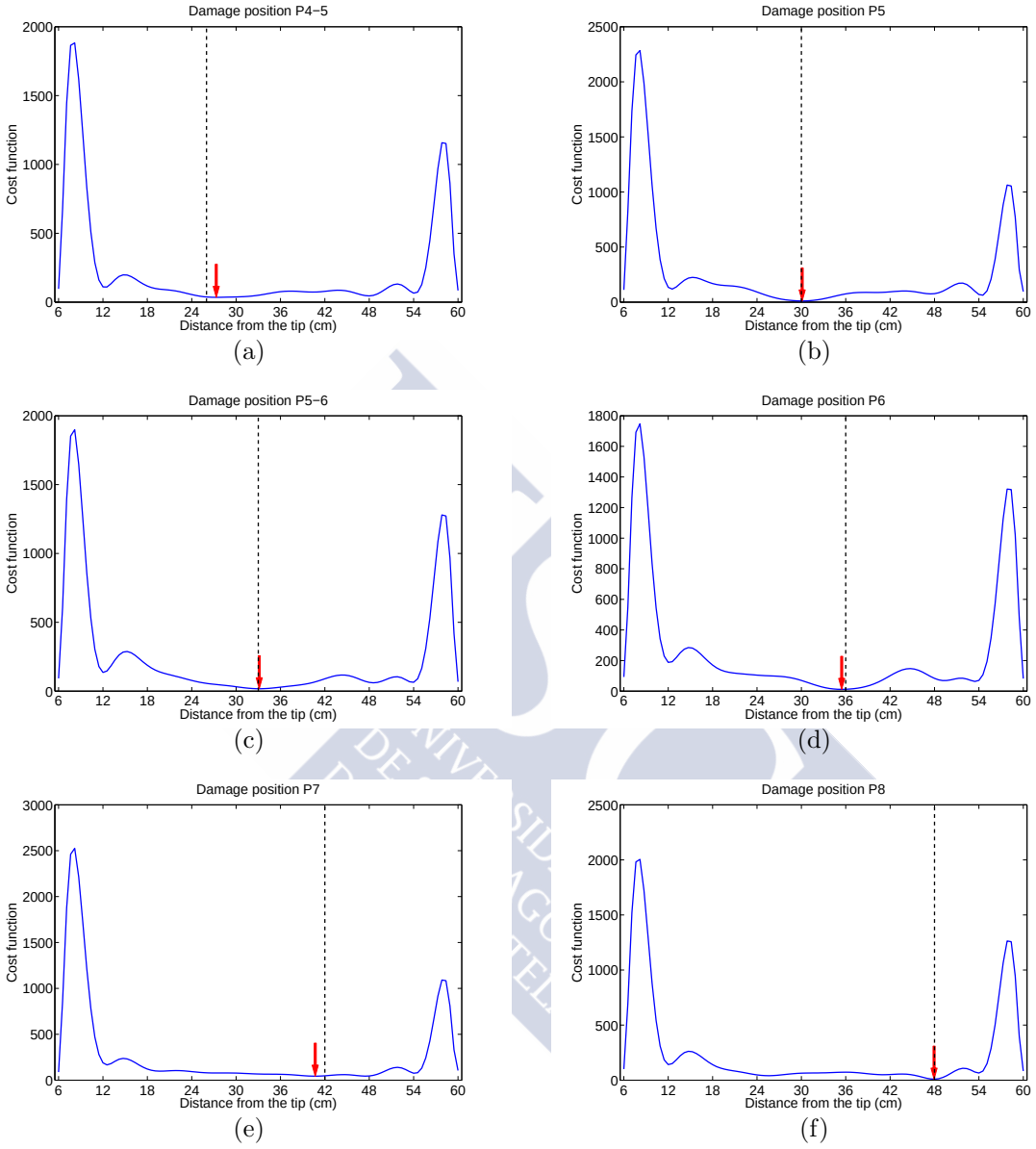

Figure 4.16: Cost function representation. The black vertical dashed line indicates the true position of the damage, the red arrow the minimum value obtained after exhaustive search and Matlab *fmincon.m*: (a) damage position 4–5 (inspection), (b) damage position 5 (baseline), (c) damage position 5–6 (inspection), (d) damage position 6 (baseline), (e) damage position 7 (baseline), (f) damage position 8 (baseline).

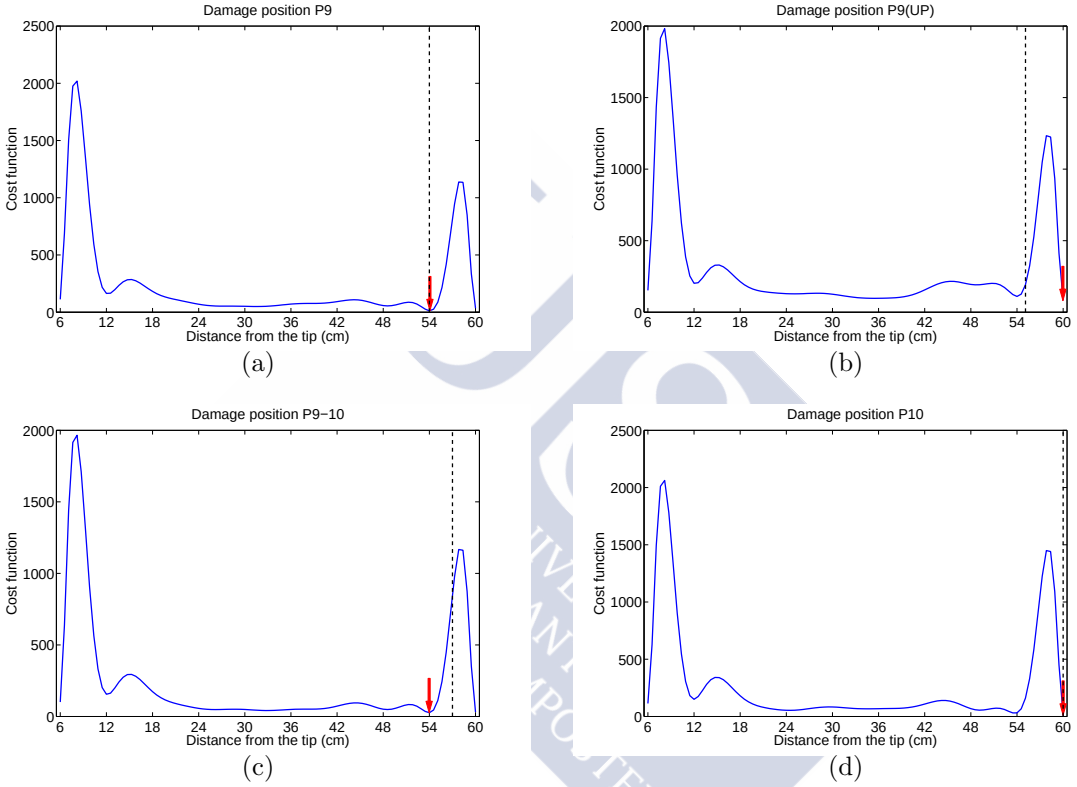

Figure 4.17: Cost function representation. The black vertical dashed line indicates the true position of the damage, the red arrow the minimum value obtained after exhaustive search and Matlab *fmincon.m*: (a) damage position 9 (baseline), (b) damage position 9bis (inspection), (c) damage position 9–10 (inspection), (d) damage position 10 (baseline).

Chapter 5

Multiple coherence via parametric models for non–stationary signals: application to an elevator

5.1 Introduction

In this chapter some examples of non–stationary signals in different laboratory situations and real applications will be presented in the context of multiple coherence computations.

Three techniques previously introduced in Section 1.2, namely:

- STFT: Short Time Fourier transform.
  Non–parametric both in time and in frequency.
- Unstructured TAR: Unstructured Time dependent AutoRegressive.
  Non–parametric in time and parametric in frequency.
- FS–TAR: Functional Series Time dependent AutoRegressive.
  Parametric both in time and in frequency.

will be detailed, used and compared in the sequel.

The three presented techniques will be compared first analyzing univariate artificially generated signals, and after computing coherences in different scenarios:

- Numerical simulation and experimental replication (in a semi–anechoic chamber) of a two source case to understand coherence computations in a simple example. In this case one of the sources will be moving with respect to the receptor point and the other one fixed, see Figure 5.1.

- An application in the framework of a real elevator. Several microphones and accelerometers were placed at different noise sources and paths and the noise and vibration in the cabin (receptor) was measured. In this case, the cabin is moving with respect to some of the sources of noise, which may cause non–stationarity in the signals involved. The main goal is to identify the main source/path contributions in different cases.

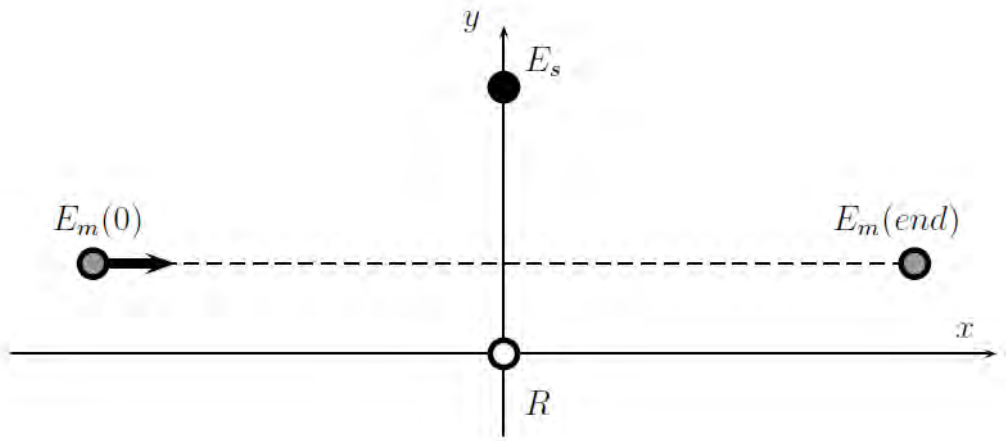

Figure 5.1: Configuration with a static noise source E_s and a moving one E_m, receptor at point R; $x - y$ projection.

This chapter is organized as follows: in section 5.2 the main theoretical tools that will be used along the chapter are presented, section 5.3 is devoted to experimental results, finally section 5.4 outlines the conclusions and future work.

5.2 Theoretical background

The use of the multiple coherence method, requires to perform a spectral analysis of the signals involved in both the univariate and the multivariate cases. This will be presented in this section.

5.2.1 Univariate case

Let us consider a given random process $\{x[n]\}_{n=-\infty}^{+\infty}$. In this way, the **power spectral density** (PSD) is defined by:

$$P_{xx}(f) = T_s \sum_{k=-\infty}^{+\infty} r_{xx}[k]\ e^{-i2\pi f T_s k}, \tag{5.1}$$

where

$$r_{xx}\left[k\right] = \mathcal{E}\left\{x^*\left[n\right] x\left[n+k\right]\right\}, \tag{5.2}$$

is the **autocorrelation function**, T_s is the sampling period and $\mathcal{E}$ is the expected value operator. So the PSD is in fact the discrete Fourier transform (multiplied by factor T_s), denoted by $\mathcal{F}$, of the autocorrelation function:

$$P_{xx}(f) = T_s \mathcal{F}\{r_{xx}\left[k\right]\}. \tag{5.3}$$

The PSD describes the power distribution for each frequency of $x[n]$ and, as such, is real and non negative.

Note at this point that, for these quantities to be well defined, it is necessary for the process considered to be wide sense stationary (WSS) (see [60]) since the correlation functions are supposed to depend only on the time lag k but not on the time instant.

In a general non–stationary case, the autocorrelation function is not only a function of the time lag k, but it also depends on n, that is, $r_{xx}\left[n,k\right]$. For this reason, a natural extension of the PSD to the non–stationary case would be given by:

$$P_{xx}(f,n) = T_s \sum_{k=-\infty}^{+\infty} r_{xx}[n,k]\ e^{-i2\pi f T_s k}. \tag{5.4}$$

This definition corresponds to the concept of "frozen" power spectral density [87], also known as rational relief of Grenier [50] in some special cases, that can be found in the literature. Note that other extensions of the PSD to the non–stationary case exist [88, 55], but they are less convenient for the scope of this work.

Next, two different approaches to obtain the PSD will be presented: the first one corresponds to methods that are unstructured (in time) – splitting the signal into time blocks that will be considered stationary – whereas the second one handles the time dependency in a different way by assuming a structured (in time) parameter evolution – represented by a functional basis.

Unstructured methods

The methods considered in this section assume that the involved signals are "locally" stationary, assumption somehow consistent with the definition in Equation (5.4). In consequence, they split the signal into time blocks that will be analyzed using techniques that are valid for stationary analysis. What is important to bear in mind is the fact that the frequency resolution obtained will be directly related to the size of the blocks considered; in fact, the larger the blocks, the better the frequency resolution obtained. However, there is a tradeoff between the frequency and the time resolution since a reduced number of blocks implies a very poor time resolution. This is related to the uncertainty principle, known as the *Heisenberg–Gabor limit* in this context. An overlap can be considered that helps us to have more blocks, and thus additional time resolution. Two different methods that are generally used for stationary signals are distinguished: FFT and AR methods.

From this point till the end of the section, and for practical reasons, finite length signals $\{x[n]\}_{n=0}^{N-1}$ will be considered.

STFT method

When methods based in the direct calculus of the Fourier transform are used in each block, the Short Time Fourier Transform (STFT) is obtained. There are several ways to estimate the PSD of a signal (see [61]). One of the most widely used is the Blackman–Tukey estimator (BT). Given a discrete realization of the random process $\{x[n]\}_{n=0}^{N-1}$ (time series), the BT estimator is defined as:

$$\widehat{P}_{\mathrm{BT}}(f) = T_s \sum_{k=-(N-1)}^{N-1} \widehat{r}_{xx}[k]\; e^{-i2\pi f T_s k}, \tag{5.5}$$

where $\widehat{r}_{xx}[k]$ is an estimator of the autocorrelation function, given by:

$$\widehat{r}_{xx}[k] = \begin{cases} \dfrac{1}{N} \displaystyle\sum_{n=0}^{N-1-k} x^*[n]x[n+k], & \text{for } k = 0, 1, \ldots, N-1, \\ \\ \widehat{r}^*_{xx}[-k], & \text{for } k = -(N-1), -(N-2), \ldots, -1. \end{cases} \tag{5.6}$$

Note that the computational cost of this procedure is of $O(N \log N)$ operations, since the approximation of the autocorrelation function (5.6) and the computation of (5.5) can be done using the Fast Fourier Transform (FFT) algorithm. This should be done for all the blocks, but this task can be easily parallelized (since the blocks are independent), reducing the computational cost of the method.

Note that comparing (5.1)–(5.2) with (5.5)–(5.6) two approximations have been made:

i) the expectation is replaced by averages in time, simplification that is justified under the assumption of ergodicity of the signals (see [79]).

ii) the averages in (5.6) have less terms for large values of k, due to the finite amount of data. In fact, it is as completing the available data with zeros, where the data is missing.

This second point is in general an incorrect assumption and it can be seen as multiplying the original infinite length signal by a rectangular window. This has some implications in the frequency resolution, such as the phenomenon of leakage (which is a broadening to nearby frequencies when the real power of a signal is concentrated in a very narrow bandwidth). In addition the narrowest spectral response is limited by the width of the main lobe of the Fourier transform of the selected window. To reduce its effects different windows, such as Hamming, Hann, Blackman, Triangular, etc, with better spectral properties can be used when calculating this estimator, see [106]. In this work the Hann window has been selected.

Also note that this estimation method has a high variability so it is necessary to make some additional time averages in the blocks that have been made, leading to an additional loss in time resolution.

Unstructured TAR method

In order to overcome some of the inconveniences of the STFT method, such as the leakage and the truncation through a multiplication window, parametric methods can be used. This methods replace the original signal by another one having a special structure depending on a few parameters and whose PSD is easily computable. An important example is the AutoRegressive model.

In an autoregressive model the signal is approximated by the linear difference equation with real coefficients:

$$x[n] + \sum_{i=1}^{n_a} a_i \; x[n-i] = u[n], \tag{5.7}$$

where $x[n]$ is the output sequence of a filter (of order n_a) which models the observed data, and $u[n]$ is the conducting noise, which will be supposed to be a white noise with zero mean and variance σ_u^2.

To obtain the coefficients a_i, with $i = 1, \ldots, n_a$ and the variance of the white noise σ_u^2 from a finite series of data, several techniques can be used, such as the Ordinary Least

Squares method or the Maximum Likelihood method. All of them in the end must solve a linear set of equations often called the Yule–Walker equations. Due to the particular structure of the matrix involved in the linear system (which is Toeplitz) the computational cost of this method is $O(n_a^2)$ operations using the Levinson algorithm. Note that this order n_a will be related to the length of the signal, but will not be higher than half this length and in general it will be much lower (see [61]). Again this has to be done independently for each considered block, and it is a parallelizable task.

It can be checked that the PSD of a signal with this structure is totally described in terms of the model parameters (see [60]) through the equation:

$$P_{\mathrm{AR}}(f) = \frac{T_s \sigma_u^2}{\left| 1 + \sum_{i=1}^{n_a} a_i \; e^{-i 2\pi f T_s i} \right|^2}, \tag{5.8}$$

where the frequency f takes values from $-1/(2T_s)$ to $1/(2T_s)$.

Analyzing this expression, it can be seen that this method is well suited for signals having peaks in the PSD (they will be approximated by the zeroes of the denominator in Equation (5.8)), but not valleys (places where the PSD almost vanishes). For this to be possible it would be needed to include in the model some extra terms to have an AutoRegressive Moving Average (ARMA) model (see [60]).

One critical aspect when using this type of methods is the choice of the order n_a. If the order is too low then a very softened approximation of the PSD will be obtained. An intuitive approach would be to construct a sequence of autoregressive models with increasing orders, until the prediction error reaches a minimum. However, since this error is monotonically decreasing with the order of the model, this procedures would always lead to the model with the highest order. In addition, a high order might produce spurious peaks on the approximated PSD. This is why a penalization for the inclusion of a new parameter in the error criteria needs to be included. Based on this, in [61] the authors outline different criteria for selecting this order, such as the Final Prediction Error (FPE), Akaike Information Criterion (AIC) or the Bayesian Information Criterion (BIC). In this work, FPE criterion has been chosen in the selection of the best model order.

When analyzing a non–stationary signal, as it has already been said, the signal will be divided into blocks and each of them is analyzed with this technique. As a first option it is possible to allow each block to select a different order and according to it calculate the involved parameters. A second option would be to fix an order for all the blocks and then calculate the coefficients for this order. The second alternative may present some

advantages over the first one, since the order of the model should be only computed once (but the best one for all the signal should be chosen). As a drawback of this second alternative, if the PSD has some stiff variation in time it can happen that a higher order is needed for some particular blocks (associated to the time instants in which this occur) that is not necessary for the whole signal, leading to spurious peaks on the remaining time regions of the PSD. In this application, due to the non–stationarity of the signals involved, each block is allowed to have a different order.

To fix ideas and to compare this approach to the one that will be presented in the next subsection, let us assume that n_a is fixed for all the blocks. Let us assume that the signal is divided in J blocks of length L (without overlap). Then for every time n in block j ($j \in \{1, \ldots, J\}$):

$$x[n] + \sum_{i=1}^{n_a} a_i^j \; x[n-i] = u[n]. \tag{5.9}$$

So the full signal can be expressed as:

$$x[n] + \sum_{i=1}^{n_a} a_i[n] \; x[n-i] = u[n], \tag{5.10}$$

where

$$a_i[n] = a_i^j, \text{ if } n \in \{(j-1)L + 1, jL\}. \tag{5.11}$$

It is important to notice that there is a time evolution of the parameters. The AR parameters are thus piece–wise constant functions in time.

FS–TAR methods

In order to improve the time evolution of the AR parameters, to decrease the number of involved parameters, and to handle the time dependency in a more natural way, a TAR model with a deterministic parameter evolution can be considered. This means that the parameters will evolve in a structured form, represented by functions belonging to specific functional subspaces (see [87]). This is a more elaborated method, known as Functional Series Time–dependent AutoRegressive (FS–TAR) method. It has the general form:

$$x[n] + \sum_{i=1}^{n_a} a_i[n] \; x[n-i] = u[n], \qquad u[n] \sim NID(0, \sigma_u^2[n]), \tag{5.12}$$

with n designating discrete time, $x[n]$ the non–stationary vibration response signal, $u[n]$ the conducting non–stationary noise innovations characterized by zero mean and time

varying (TV) variance $\sigma_u^2[n]$, and $a_i[n]$, the model's TV AR parameters, which will be detailed in the sequel. NID$(0, \sigma_u^2[n])$ stands for normally independently distributed random variables with the indicated mean and variance.

Deterministic parameter evolution TAR models impose deterministic structure on the time evolution of their parameters. This is achieved by postulating model parameters as deterministic functions of time belonging to specific functional subspaces. So, the AR parameters and the innovations variance, are expanded on the selected functional subspaces:

$$\mathcal{F}_{AR} := \text{span}\left\{G_{b_a(1)}[n], \ldots, G_{b_a(p_a)}[n]\right\}, \tag{5.13}$$

$$\mathcal{F}_{\sigma_u^2} := \text{span}\left\{H_{b_s(1)}[n], \ldots, H_{b_s(p_s)}[n]\right\}. \tag{5.14}$$

Each functional subspace consists of a set of basis functions selected from a suitable family (such as a polynomial or a trigonometric family, rational functions,...). Through proper selection of the functional spaces, FS–TAR models may represent various types of evolution in the dynamics, including slow and fast evolutions. In this work Legendre polynomials have been chosen for the AR coefficients, see Appendix A.2 for more details. In the case of the variance approximation, an approximation using high order polynomials might lead to a non–positive approximation due to the Runge phenomenon (see [104], p. 186). In this work, as a novelty, Bernstein polynomials [78], see Appendix A.3, for more details, are proposed for this approximation leading to a non–negative approximation.

The AR and variance space dimensionalities are indicated as p_a, p_s, respectively, while the indices $b_a(j)$ $(j = 1, \ldots, p_a)$ and $b_s(j)$ $(j = 1, \ldots, p_s)$ designate the specific basis functions of the particular family that are included in each space. In this work, $b_a(j) = j - 1$ and $b_s(j) = j - 1$, which means that polynomials up to order $p_a - 1$ and $p_s - 1$ are selected. It should be noted that some intermediate functions could not be needed, so an extra work for selecting the specific functions could be done, but this is not done in this case.

The time varying AR parameters and the innovations variance of an FS–TAR $(n_a)_{[p_a,p_s]}$ model are then expressed as:

$$a_i[n] := \sum_{j=1}^{p_a} a_{i,j} G_{b_a(j)}[n], \qquad \sigma_u^2[n] := \sum_{j=1}^{p_s} s_j H_{b_s(j)}[n], \tag{5.15}$$

with $a_{i,j}$ (respectively s_j) designating the AR (respectively the innovations variance) projection coefficients. A specific model structure $\mathcal{M}_{FS}$ is defined by the model orders n_a, and the functional subspaces $\mathcal{F}_{AR}$, $\mathcal{F}_{\sigma_u^2}$:

$$\mathcal{M}_{FS} := \left\{ n_a, \mathcal{F}_{AR}, \mathcal{F}_{\sigma_u^2} \right\}.$$

Let us give some further details on the estimation of all the coefficients appearing in the model. The following notation is introduced:

$$\begin{aligned} \theta &= [\vartheta^T, \mathbf{s}^T]^T \in \mathbb{R}^{(p_a \cdot n_a + p_s)\times 1}, \\ \vartheta &= [a_{1,1}, \ldots, a_{1,p_a} | \ldots | a_{n_a,1}, \ldots, a_{n_a,p_a}]^T \in \mathbb{R}^{p_a \cdot n_a \times 1}, \\ \mathbf{s} &= [s_1, \ldots, s_{p_s}]^T \in \mathbb{R}^{p_s \times 1}. \end{aligned} \tag{5.16}$$

The obtention of the coefficients ϑ is made via an ordinary least squares method. Rewriting Equation (5.12):

$$x[n] = -\sum_{i=1}^{n_a} \sum_{j=1}^{p_a} a_{i,j} G_{b_a(j)}[n] x[n-i] + u[n] \Leftrightarrow x[n] = \phi_A^t[n] \cdot \vartheta + u[n], \tag{5.17}$$

with:

$$\begin{aligned} \phi_A[n] = \; & \big[-G_{b_a(1)}[n]x[n-1], \ldots, -G_{b_a(p_a)}[n]x[n-1] | \ldots | \\ & -G_{b_a(1)}[n]x[n-n_a], \ldots, -G_{b_a(p_a)}[n]x[n-n_a] \big]^T. \end{aligned} \tag{5.18}$$

So the ordinary least squares estimator is given by the solution of:

$$\left(\frac{1}{N} \sum_{n=1}^{N} \phi_A[n] \phi_A^t[n] \right) \widehat{\vartheta} = \left(\frac{1}{N} \sum_{n=1}^{N} \phi_A[n] x[n] \right). \tag{5.19}$$

After this vector has been obtained $\mathbf{s}$ needs to be estimated. First the vector $u[n]$ is calculated for $\widehat{\vartheta}$:

$$u[n, \widehat{\vartheta}] = x[n] + \sum_{i=1}^{n_a} \sum_{j=1}^{p_a} \widehat{a}_{i,j} G_{b_a(j)}[n] x[n-i], \tag{5.20}$$

and estimate its variance, by performing the sliding window operation given in:

$$\widehat{\sigma}_u^2[n] = \frac{1}{2M+1} \sum_{\nu=n-M}^{n+M} u^2[\nu, \widehat{\vartheta}], \tag{5.21}$$

which is now projected in the space $\mathcal{F}_{\sigma_u^2}$ and estimate the p_s coefficients $\widehat{s}_1, \ldots, \widehat{s}_{p_s}$. An important novelty of this work relies on how this estimation is done. Since the function $\sigma_u^2[n]$ is a positive function, for some applications (as coherence computations) it will be important that its estimation remains also positive. By using standard polynomial basis

functions, such as Legendre, it is difficult to ensure positivity of this estimation for all times. This could be done by including some restrictions in the estimation process, but there would be too many if this has to be done for every time instant; if done for only some of them, there is no guarantee that the approximation is always positive. This would also be computationally expensive and could lead to an overconstrained system that would imply an overestimation of the variance (not to have negative values). An alternative approach is presented in the sequel. The variance will be estimated via the Bernstein polynomials of order p_s of this variance function. Given a function, $f(x)$ in the closed interval $[0, 1]$ its Bernstein polynomial of order m is given by:

$$B_m(x) = B_m^f(x) = \sum_{k=0}^{m} f\left(\frac{k}{m}\right)\binom{m}{k} x^k (1-x)^{m-k}, \tag{5.22}$$

where $\binom{m}{k} = \dfrac{m!}{k!(m-k)!}$ is the binomial coefficient. These polynomials have important properties regarding uniform convergence to the original function [78]. An immediate change of variable should initially be done if a different interval is to be considered.

The function to be approximated in this case is only available for some discrete points but the approximation can still be done with a good selection and averaging from the discrete points available. The fact that the polynomials are positive for all $x \in [0, 1]$ and the way in which the specific coefficients are chosen (values of the original function that are also positive) assures that the approximation is also positive. So several advantages are obtained with this selection of the basis functions:

- Once the order p_s has been determined, which corresponds to Bernstein polynomials up to order $p_s - 1$, no computational cost is associated with the obtention of the coefficients $\widehat{s}_1, \ldots, \widehat{s}_{p_s}$ since they are specific values of the determined $\widehat{\sigma}_u^2[n]$.
- The approximated variance remains positive.
- It is a good approximation of the function (although the convergence can be slow). As long as there are no very stiff variations on the variance to be approximated, an order not to high will be enough.

Concerning the computational cost, Equation (5.19) is solved via an Ordinary Least Squares algorithm. In fact, this involves the computation of a pseudo–inverse (or the inverse of a $n_a \cdot p_a \times n_a \cdot p_a$ matrix which is an expensive part, above all for high orders), and a matrix–vector product. Then the residual noise and its variance are computed. Finally

σ_u^2 is interpolated in the appropriate subspace $\mathcal{F}_{\sigma_u^2}$, but with the selected procedure this involves no computational cost, once the order p_s has been chosen.

In analogy to the PSD for the Unstructured TAR case (5.8) and according to the model (5.12), once all the appearing parameters have been determined, the non–stationary PSD (defined by (5.4)) for this process is given by:

$$P_{\mathrm{TAR}}(f,n) = \frac{T_s \sigma_u^2[n]}{\left| 1 + \sum_{i=1}^{n_a} a_i[n]\ e^{-\boldsymbol{i} 2\pi f T_s i} \right|^2}, \tag{5.23}$$

with $a_i[n]$ and $\sigma_u^2[n]$ given as in Equation (5.15).

5.2.2 Multivariate case

In an analogous way to the univariate case, the **cross power spectral density** (CPSD) is defined by:

$$P_{xy}(f) = T_s \sum_{k=-\infty}^{+\infty} r_{xy}[k]\ e^{-\boldsymbol{i} 2\pi f T_s k}, \tag{5.24}$$

where r_{xy} is now the **cross correlation function**:

$$r_{xy}[k] = \mathcal{E}\{x^*[n] y[n+k]\}. \tag{5.25}$$

The CPSD is in general complex. The modulus of the CPSD indicates whether frequency components in $x[n]$ are associated with large or small amplitudes at the same frequency in $y[n]$, and the phase indicates the phase lag or lead of $x[n]$ with respect to $y[n]$ for a given frequency component.

In practice, several signals, say M, will be analyzed at the same time. In that case the following matrix would be needed:

$$\mathbf{P}(f) = \begin{pmatrix} P_{x_1x_1}(f) & P_{x_1x_2}(f) & \cdots & P_{x_1x_M}(f) \\ P_{x_2x_1}(f) & P_{x_2x_2}(f) & \cdots & P_{x_2x_M}(f) \\ \vdots & \vdots & \ddots & \vdots \\ P_{x_Mx_1}(f) & P_{x_Mx_2}(f) & \cdots & P_{x_Mx_M}(f) \end{pmatrix} \tag{5.26}$$

Unstructured methods

STFT method

The extension of the techniques described in section 5.2.1 to the calculation of estimators of the CPSD is straightforward. Thus, similarly to that used when describing the Blackman–Tukey estimator, the CPSD estimator between $x[n]$ and $y[n]$ can be introduced as:

$$\widehat{CP}_{\mathrm{BT}}(f) = T_s \sum_{k=-(N-1)}^{N-1} \widehat{r}_{xy}[k]\ e^{-\boldsymbol{i}\pi f T_s k}, \tag{5.27}$$

where $\widehat{r}_{xy}[k]$ is a cross correlation estimator which can be easily generalized using (5.6) and (5.25). The same remarks made for the univariate case apply now to this estimator.

Unstructured TAR method

Calculating cross power spectral densities using autoregressive techniques requires a generalization of the ideas introduced in the previous sections to deal with vectorial processes.

Let us assume that there are M different signals $\mathbf{x}[n] = [x_1[n], \ldots, x_M[n]]^t$; the aim of this section is to explain how to obtain the PSD and CPSD of all the signal combinations, i.e. the matrix given in Equation (5.26).

Similarly to the case of a single signal, the AR model for N signals is defined by:

$$\mathbf{x}[n] + \sum_{i=1}^{n_a} \mathbf{A}_i\ \mathbf{x}[n-i] = \mathbf{u}[n], \tag{5.28}$$

where $\mathbf{A}_i$ are now $M \times M$ matrices defining the autoregressive parameters, and $\mathbf{u}[n]$ is an $M \times 1$ vector which represents the conducting noise of the process, which is assumed to be a WSS process. Assuming (as in the case of a single signal) that the conducting process is a white noise with a constant covariance matrix denoted by $\mathbf{\Sigma}_u$, then the PSDs and CPSDs of the output vector process are given by, see [102]:

$$\mathbf{P}_{\mathrm{AR}}(f) = T_s \widetilde{\mathbf{A}}^{-1}(f) \mathbf{\Sigma}_u \widetilde{\mathbf{A}}^{-H}(f), \tag{5.29}$$

defined for $|f| \leq 1/(2T_s)$, where:

$$\widetilde{\mathbf{A}}(f) = \mathbf{I} + \sum_{i=1}^{p} \mathbf{A}_i\ e^{-\boldsymbol{i}2\pi f T_s i}. \tag{5.30}$$

Just as in the univariate case, the analysis will be made dividing the signal in time blocks and performing this procedure block by block.

FS–VTAR methods

Functional Series Vector Time–dependent AutoRegressive (FS–VTAR) models [102] constitute conceptual extensions of their conventional (stationary) Vector AR counterparts, in that their parameters and the innovations covariance matrix are explicit functions of time, by belonging to functional subspaces spanned by selected functions (basis functions). Thus, an FS–VTAR $(n_a)_{[p_a,p_s]}$ model, with n_a denoting its AutoRegressive (AR) orders, p_a (respectively p_s) the AR (respectively the innovations covariance matrix) functional basis dimensionalities, respectively, is of the form:

$$\mathbf{x}[n] + \sum_{i=1}^{n_a} \mathbf{A}_i[n]\ \mathbf{x}[n-i] = \mathbf{u}[n], \qquad \mathbf{u}[n] \sim \text{NID}(\mathbf{0}, \mathbf{\Sigma}[n]) \tag{5.31}$$

with n designating normalized discrete time, $\mathbf{x}[n] \in \mathcal{M}_{M\times 1}$ the non–stationary vibration response (vector) signal, and $\mathbf{u}[n] \in \mathcal{M}_{M\times 1}$ the innovations (residual) sequence which is uncorrelated and characterized by zero–mean and time–dependent non–singular (and generally non–diagonal) covariance matrix $\mathbf{\Sigma}[n] \in \mathcal{M}_{M\times M}$. $\mathbf{A}_i[n] \in \mathcal{M}_{M\times M}$ are the model's AR time–dependent parameter matrices, while NID$(\cdot,\cdot)$ stands for Normally Independently Distributed with the indicated mean and covariance.

Each element of the model parameter matrices $\mathbf{A}_i[n]$, and $\mathbf{\Sigma}[n]$ belong to functional subspaces $\mathcal{F}_{AR}$ and $\mathcal{F}_{\mathbf{\Sigma}}$ with basis as in (5.13) and (5.14) where the indices $b_a(j)$, $(j = 1,\ldots,p_a)$, and $b_s(j)$ $(j = 1,\ldots,p_s)$ denote the functions that are included in each basis. These functions may be selected as before. The elements of the time–dependent model parameter matrices, along with the innovations time–dependent covariance matrix, may be thus expressed as:

$$\mathbf{A}_i[n] = \begin{pmatrix} a^i_{1,1}[n] & \cdots & a^i_{1,M}[n] \\ \vdots & \ddots & \vdots \\ a^i_{M,1}[n] & \cdots & a^i_{M,M}[n] \end{pmatrix} = \{a^i_{l,m}[n]\}^M_{l,m=1}, \tag{5.32}$$

$$\text{where } a^i_{l,m}[n] := \sum_{j=1}^{p_a} a^{i,j}_{l,m} G_{b_a(j)}[n],$$

$$\mathbf{\Sigma}[n] = \begin{pmatrix} s_{1,1}[n] & \cdots & s_{1,M}[n] \\ \vdots & \ddots & \vdots \\ s_{M,1}[n] & \cdots & s_{M,M}[n] \end{pmatrix} = \{s_{l,m}[n]\}^M_{l,m=1}, \tag{5.33}$$

$$\text{where } s_{l,m}[n] := \sum_{j=1}^{p_s} s^j_{l,m} H_{b_s(j)}[n],$$

with $a_{l,m}^{i,j}$ (respectively $s_{l,m}^{j}$) designating the AR (respectively innovations covariance matrix) projection coefficients.

A specific model structure $\mathcal{M}$ is defined by the model orders and the functional subspaces:

$$\mathcal{M} := \{n_a, \mathcal{F}_{AR}, \mathcal{F}_{\mathbf{\Sigma}}\} \tag{5.34}$$

and a FS–VTAR model is parameterized in terms of $a_{l,m}^{i,j}$ and $s_{l,m}^{j}$.

The obtention of the coefficients is made via the ordinary least squares method in its multivariate form in this case. Equation (5.31) needs to be adapted to the standard form of a multivariate least squares problem, so as to determine the matrices involved in the estimation in an analogous way as it was done in the univariate case [102].

As before the functional family chosen for the estimation of the coefficients is the Legendre polynomials, while for the variance estimation, it is the Bernstein polynomials. Now the variance is, for each time instant, a positive definite matrix. With this family selection, it is assured that the estimated variance is also positive definite. The coefficients are, as before, specific matrices from the estimated variance, which implies they are themselves positive definite, and since the Bernstein polynomials are positive for every time instant, a positive definite matrix is obtained in the approximation.

5.2.3 Ordinary and multiple coherence

For the purpose of coherence calculation, multivariate models as those described in the previous section need to be considered. The calculation of coherences is useful to separate the contribution of different sources [86] and to obtain the predominant source in some applications. In previous studies [49], the authors have already performed studies in this direction using unstructured methods in time (like the two first methods presented above). Now the fully parametric (FS–TAR) method will also be used for coherence computations.

First of all the concepts of ordinary coherence and multiple coherence will be introduced. The **ordinary coherence** between two signals $x[n]$ and $y[n]$ is defined by:

$$\gamma_{xy}^2(f,n) = \frac{|P_{xy}(f,n)|^2}{P_{xx}(f,n)P_{yy}(f,n)} \in [0,1]. \tag{5.35}$$

Ordinary coherence is then a statistical indicator which indicates whether or not a given input and output are correlated (i.e. linearly related). It has values between 0 and 1, with 1 indicating a perfectly linear relationship between the input and the output, and 0 indicating a complete lack of correlation. From this definition it can be seen that it is

important for the power spectral density (or its estimation) in the denominator not to become 0. This is one of the reasons why it is crucial that the variance does not oscillate from positive to negative values and so the Bernstein polynomials are very useful for this application.

For cases in which there are many inputs and one or more outputs, it is sometimes worth or necessary estimating the degree of correlation existing between one group of selected inputs $X[n] = \{x_1[n], \ldots, x_M[n]\}$ and one output $y[n]$. This can be done with the multiple coherence, defined as:

$$\gamma^2_{Xy}(f,n) = \frac{P^H_{Xy}(f,n) P^{-1}_{XX}(f,n) P_{Xy}(f,n)}{P_{yy}(f,n)}, \tag{5.36}$$

where P_{Xy} is the M dimensional vector of the CPSD between inputs X and the output y, P_{XX} is the $M \times M$ dimensional matrix of the PSD and CPSD of the series of inputs and P_{yy} is the PSD of the output.

Multiple coherence also takes values between 0 and 1. A value of 1 indicates that all the inputs considered as a group are linearly related to the output, while a value of 0 indicates that none of the inputs are correlated to the output. Also here it becomes clear the importance of the positive definiteness of the variance matrix and the utility of the Bernstein polynomials.

For practical implementations, as a first step, possible sources of noises need to be identified and they will have to be measured, as well as the considered output. A clear and important limitation of the coherence is that, if two inputs are coherent among them, their contributions to the output will not be distinguishable. This will happen for many practical applications since it will be difficult to isolate all the possible sources. For this reason, coherence among all the inputs will have to be computed and coherent inputs will need to be grouped so that their contribution to the output will be computed as the whole group. Another difficulty arises in this case, since for coherent sources the matrix P_{XX} is ill–conditioned, this is why a pseudo inverse needs to be computed instead of the standard inverse.

5.3 Coherence computations: Numerical and experimental results

The ultimate goal in this section is the calculation of coherences. As it has already been shown, for this, PSD and CPSD of the signals involved need to be obtained. So, first of all

an univariate analysis will be performed with some artificial signals constructed to have a specific time–variant PSD expression. For this signal, its PSD will be "known" a priori, so this allows to validate the methods. Then, to introduce coherence calculations, a *simple* example with only two input sources will be presented in two frameworks, a numerical and an experimental one carried out in a semianechoic chamber. For this example the three previously presented methods, namely FFT, Unstructured TAR and FS–TAR, will be used and compared. Finally some elevator measurements will be analyzed, starting with a univariate analysis of the acceleration signal in the z direction on top of the drive machine of the elevator, and then analyzing a *more elaborate* coherence calculation example considering the full elevator system.

5.3.1 Univariate analysis of numerical and laboratory signals

In this first subsection an artificial analytical signal will be constructed in such a way that its PSD evolve with time in a known way, to be able to validate the methods. For this purpose an analytical signal made up as a sum of two locally AR signals will be used. The evolution of the coefficients has been chosen in such a way that the frequency in which they have a peak evolves with time in a desired form. It is well known that the roots of the AR polynomial must be inside the unit circle so the roots of the first signal have been defined to vary linearly:

$$0.9\ \left(\frac{\sqrt{2}}{2}+i\frac{\sqrt{2}}{2}\right)\longrightarrow 0.9\ \left(-\frac{\sqrt{2}}{2}-i\frac{\sqrt{2}}{2}\right)$$

$$0.9\ \left(\frac{\sqrt{2}}{2}-i\frac{\sqrt{2}}{2}\right)\longrightarrow 0.9\ \left(-\frac{\sqrt{2}}{2}+i\frac{\sqrt{2}}{2}\right)$$

with an extra constant real root of 0.5. For the second signal the roots have been chosen to vary linearly:

$$0.9\ \left(-0.99+i\sqrt{1-0.99^2}\right)\longrightarrow 0.9\ \left(0.99+i\sqrt{1-0.99^2}\right)$$

$$0.9\ \left(-0.99-i\sqrt{1-0.99^2}\right)\longrightarrow 0.9\ \left(0.99-i\sqrt{1-0.99^2}\right)$$

with the same extra real root of 0.5. The coefficients can be obtained directly from the defined roots and a linear interpolation of them in time is considered.

In this way, the first signal has the following expression:

$$y[n]+\overline{a}_1[n]x[n-1]+\overline{a}_2[n]x[n-2]-0.405x[n-3]=u[n],$$

with

$$\begin{aligned}\overline{a}_1[n] &= \frac{-2.5456n + 0.7728n_0 + 1.7728n_1}{n_0 - n_1},\\ \overline{a}_2[n] &= \frac{1.2728n + 0.1736n_0 - 1.4464n_0}{n_0 - n_1},\end{aligned}$$

and the second one:

$$z[n] + \widetilde{a}_1[n]x[n-1] + \widetilde{a}_2[n]x[n-2] - 0.405x[n-3] = v[n],$$

with

$$\begin{aligned}\widetilde{a}_1[n] &= \frac{3.564n - 2.282n_0 - 1.282n_1}{n_0 - n_1}.\\ \widetilde{a}_2[n] &= \frac{-1.782n + 1.701n_0 + 0.081n_1}{n_0 - n_1},\end{aligned}$$

where $n_0 = 0$ is the initial time, $n_1 = 30$ the final time, with a sampling frequency $f_s = 3333$ Hz, and u and v two white noises with zero mean and variance 1. The final signal considered is $x[n] = y[n] + z[n]$.

In Figure 5.2 the PSD of this signal with the three different methods is shown. For the FS–TAR method the Legendre polynomials basis has been chosen. The three methods give similar results, but there exist some differences. The STFT method, Figure 5.2(a) has a high variability in both time and frequency, whereas the Unstructured TAR method, Figure 5.2(b) has high variability in time, but the variability in frequency is reduced. The last method FS–TAR, Figure 5.2(c) presents smoother results, which might be an advantage in cases where an automatic detection of resonance frequencies is needed for example.

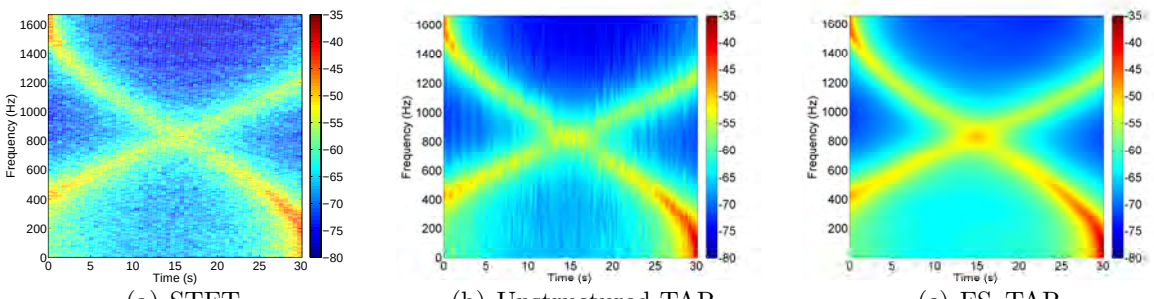

(a) STFT (b) Unstructured TAR (c) FS–TAR

Figure 5.2: PSD obtained in a numeric case with the different methods.

Now it will be shown how the evolution of the parameters is, in the case of the first four coefficients of the previous signal considering the Unstructured TAR and the FS–TAR

method and compare them. The order n_a for all the time blocks in the Unstructured TAR method and for the FS–TAR method will be fixed. In this case the order will be 15. The time evolution will be analyzed for different values of the dimension p_a in the second case. For each value of the dimension p_a, the first p_a Legendre polynomials of orders from 0 up to $p_a - 1$ will be considered.

In Figures 5.3(a), 5.4(a), 5.5(a) and 5.6(a) the evolution of the parameters when the Unstructured TAR method is used is shown, while in figures 5.3(b), 5.4(b), 5.5(b) and 5.6(b) the evolution with the FS–TAR method is presented for different values of the order p_a. It is seen that for the Unstructured TAR method there exists a high variability of the coefficients from one block to another, this is why also a smoothed result is shown too, obtained through a moving average filter to show the tendency clearer. For the FS–TAR method it is observed that as the dimension of the space increases the approximation gets better. In fact (although it is not very evident in the figures) at some moment the evolution gets stabilized, and even if the order is increased, the approximation does not change.

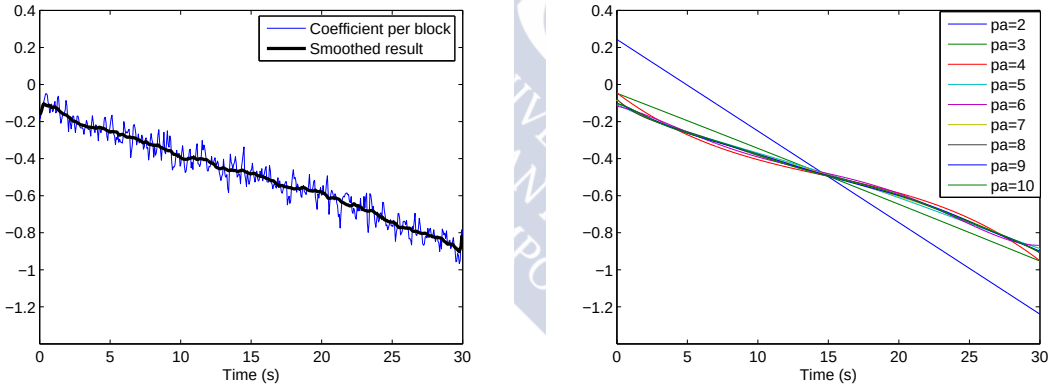

(a) Unstructured TAR (b) FS–TAR

Figure 5.3: Variation of the first coefficient.

Now the same numerical signal will be used in an experimental environment. For this a loudspeaker is placed in a semianechoic chamber and the emitted signal at a receptor point is measured. The sketch in figure 5.8 (which corresponds to the next experience to be analyzed) shows the location of the loudspeaker used (the one in the top left corner) and the receptor location (point M). Again the PSD of this signal will be analyzed with the three techniques. Results can be seen in Figure 5.7. From these, similar conclusions to the previous numerical ones can be drawn. Comparing Figures 5.2 and 5.7 it is seen that qualitatively the results are very similar, although quantitatively they are not exactly the

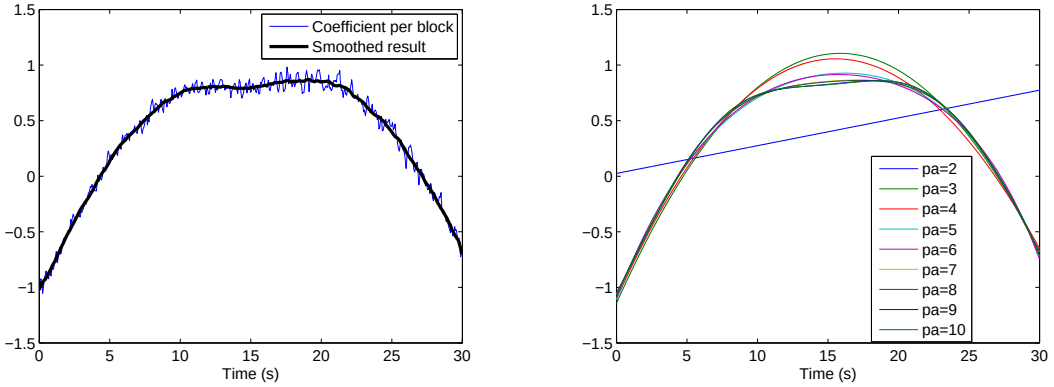

(a) Unstructured TAR (b) FS–TAR

Figure 5.4: Variation of the second coefficient.

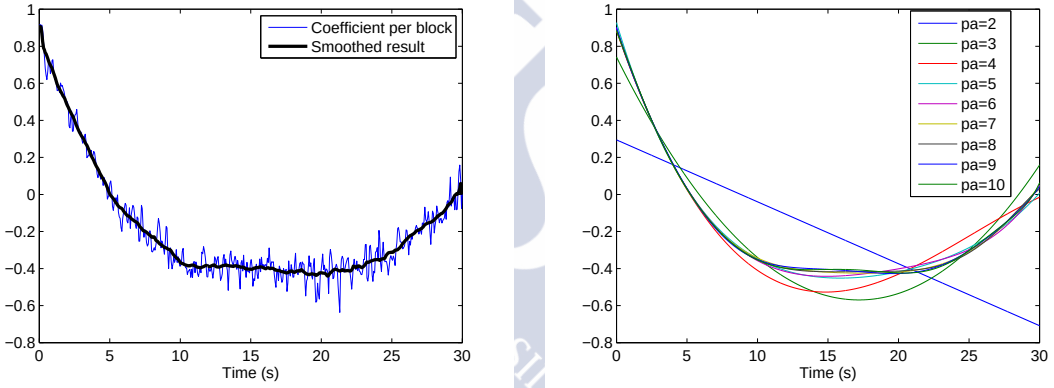

(a) Unstructured TAR (b) FS–TAR

Figure 5.5: Variation of the third coefficient.

same. This is due to the fact that the amplitudes of the sources in the experiment are not the same as those in the numerical case. A noticeable difference between figures 5.2 and 5.7 is that there exist some frequency bands with higher (respectively lower) PSD values. This might come from some reflections that occur in the semianechoic chamber (even if the walls and ceiling do not reflect acoustic waves, this is not the case for the floor, so some reflections can be observed).

5.3.2 Experience with a moving source: numerical case

Now a *simple* numerical example to show the basics of the coherence computation is presented. The example considers only two input sources, and one receptor point. The experience corresponds to the working scenario in Figure 5.8. In the next subsection

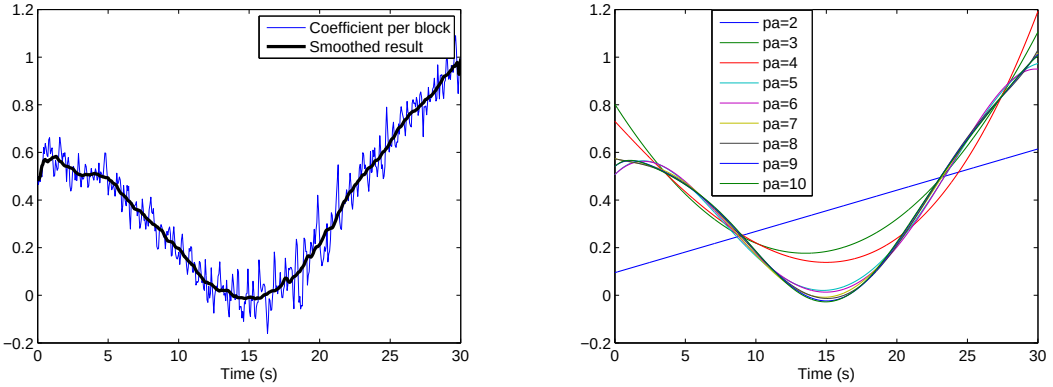

(a) Unstructured TAR (b) FS–TAR

Figure 5.6: Variation of the fourth coefficient.

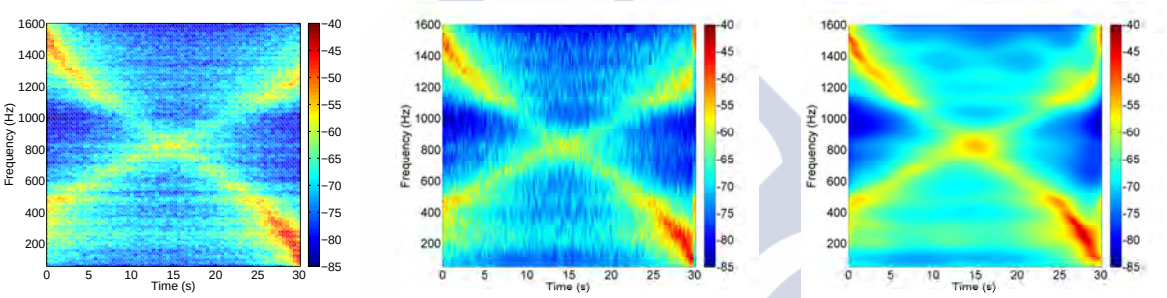

(a) STFT (b) Unstructured TAR (c) FS–TAR

Figure 5.7: PSD obtained in a experimental case with the different methods.

the same example will be considered but performing it experimentally in a semianechoic chamber, a picture taken from the bottom left corner of the sketch can be seen in Figure 5.9. All the characteristics of the numerical case have been chosen to make it analogous to the experimental one.

In Figure 5.8 the following notations have been used:

- A denotes a static source of noise.
- B denotes a moving source of noise.
- M denotes the receptor.
- $|\circ$ denotes a microphone.
- ⓝ denotes a tachometer.

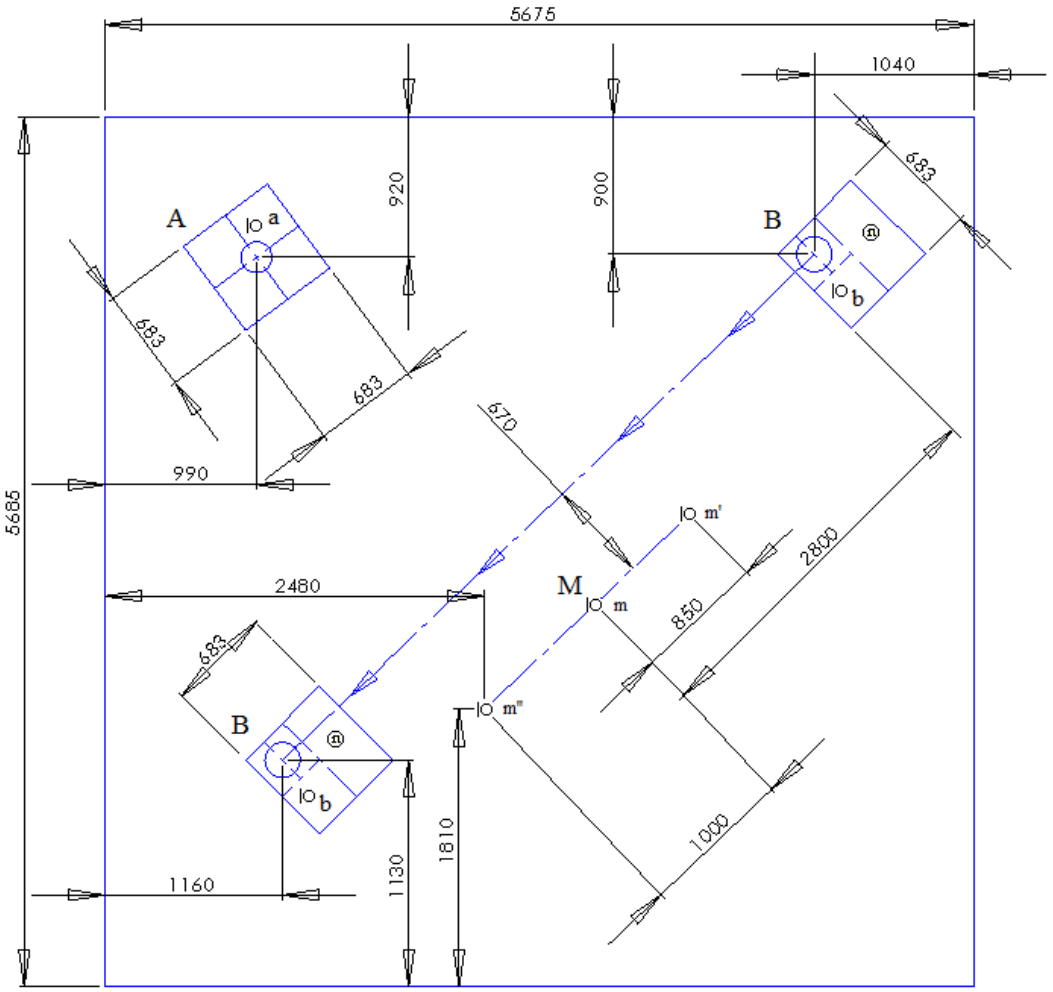

Figure 5.8: Sketch of the working scenario.

There are two different noise sources coming from loudspeakers A and B: the first one is static and located at the top left corner of the chamber; the second one moves across the diagonal of the chamber at a low speed (below 0.2 m/s). The signals to be emitted have been generated through Matlab in such a way that the moving source emits a signal with an ARMA structure having a peak at 150 Hz and the static source emits a white noise. The input signals to be analyzed, by analogy with the experimental case considered in the next section, are the sound pressure measured by two microphones, $|\circ\ a$ and $|\circ\ b$ near each loudspeaker (at a distance of 150 mm). Even if both emitted signals are WSS, the coherences will not be stationary. The evolution in time of the coherences will be

Figure 5.9: Picture of the working scenario.

due to the movement of one of the sources with respect to the receptor. The output is the signal measured at point M, microphone $| \circ \ m$, which is 1.25 m high and located at approximately 2.8 m from the initial position of the moving source. In the picture from Figure 5.9 the moving source is approximately in front of the receptor point.

To numerically obtain the signal received at the receptor point M (and at the microphones near each loudspeaker) a transfer function is needed, that given the signal emitted allows to compute the sound pressure that will be measured at some other point. Since one of the sources is moving with respect to point M, this movement will need to be accounted for when calculating this transfer function, in order to obtain the signal which will be received by the receptor. In Figure 5.10 the two contributions to the output are represented (the one coming from the moving source in Figure 5.10(a), and the one coming from the static source in Figure 5.10(b)) together with the total received signal (in Figure 5.10(c)).

The coherences obtained with the three methods are shown in Figures 5.11, 5.12 and 5.13. In all Figures the coherence is represented as a function of frequency (in the $x-$axis) and position of the moving source ($y-$axis). Even if the usual plot would be time

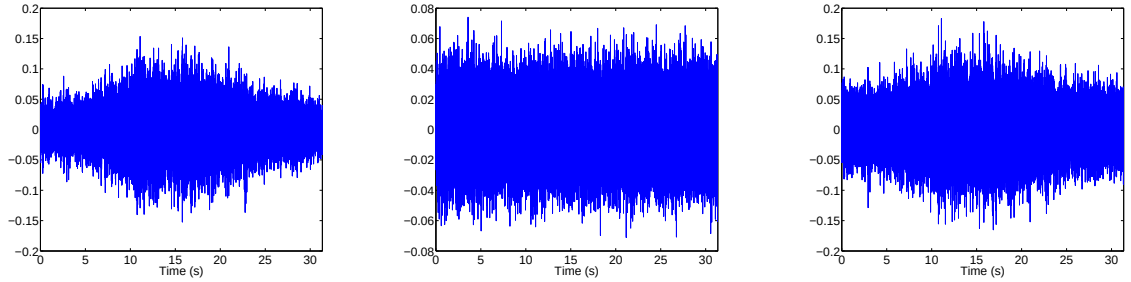

(a) Due to the moving source (b) Due to the static source (c) Total received signal

Figure 5.10: Signals received at the receptor point.

– frequency, the position has been chosen. This is due to the fact that this experience will be then reproduced in a semi–anechoic chamber. In this case the moving source is a cart that will be moved by hand, so the speed will not be constant. Actually, from one experience to the next one the speed will probably slightly vary. For all this, the plot with position in the y axis will allow an easier interpretation and comparison of results. In this numerical case the speed of the moving source has been set equal to the one measured (by a tachometer) in the experience that will be shown next.

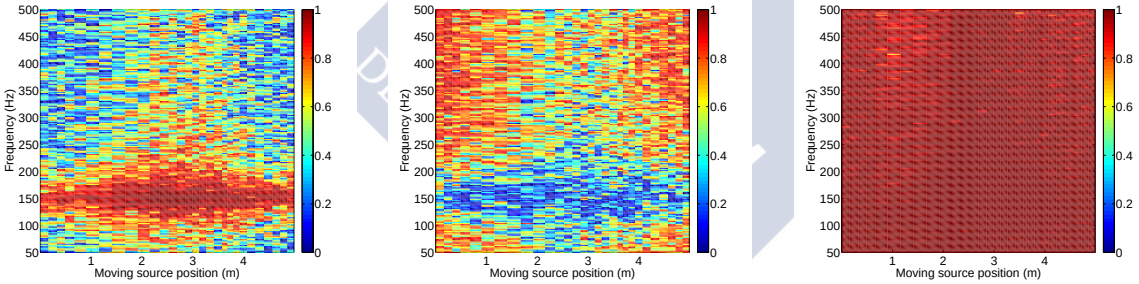

(a) Ordinary coherence from the moving source (b) Ordinary coherence from the static source (c) Multiple coherence

Figure 5.11: Coherences from the numeric case with the STFT method.

Figures (a) show the ordinary coherence between the signal emitted by the moving source and the signal measured at the receptor point. In these ones, it is seen how at frequencies around 150 Hz, the coherence is very high for all times, as expected. In the rest of the frequency range it is observed that for the central time instants the coherence is higher since, at that moment, the moving source is closer to the receptor than the static source. Figures (b) show the ordinary coherence between the signal emitted by the static source and the receptor. Here a complementary behavior to the one described above is seen. Finally figures (c) show the multiple coherence between both signals and the signal

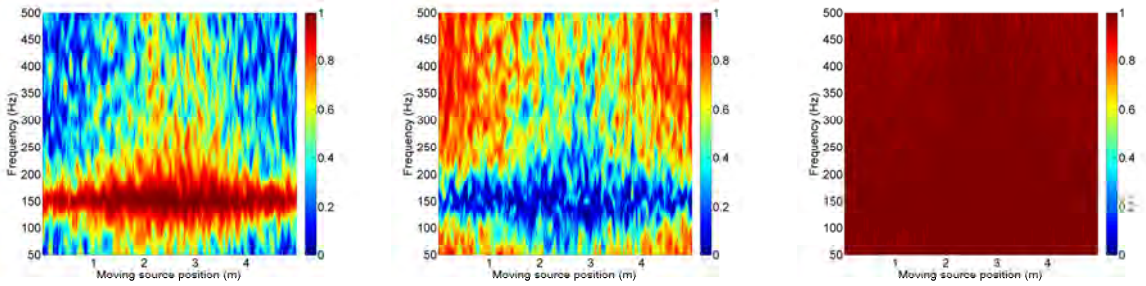

(a) Ordinary coherence from the moving source (b) Ordinary coherence from the static source (c) Multiple coherence

Figure 5.12: Coherences from the numeric case with the Unstructured TAR method.

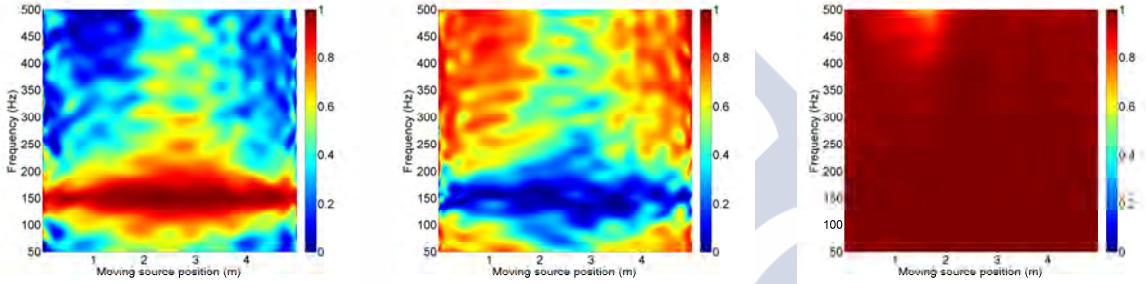

(a) Ordinary coherence from the moving source (b) Ordinary coherence from the static source (c) Multiple coherence

Figure 5.13: Coherences from the numeric case with the FS–TAR method.

at the receptor point. Theoretically this last coherence should be equal to 1 since just these two sources of noise are present. Comparing the three different methods considered, consistent results with all of them are observed. As in the case where univariate PSDs were shown, the high variability, in both time and frequency, of the STFT method, Figure 5.11, is present. For the Unstructured TAR method, Figure 5.12, a better frequency and time resolution is obtained, although still a high variability in time is present. The FS–TAR method, Figure 5.13, shows smoother results and better time and frequency resolution. For some cases this smoothing that occurs with this last method might be a problem, since it will not be possible to accurately capture a transitory event. It must also be noted that the basis functions selected are Legendre polynomials, so if the expected result has a stiff behavior (close to a discontinuity), it will not be appropriately modeled.

5.3.3 Experience with a moving source: experimental case in a semianechoic chamber

Now the aim is to reproduce the previous numerical results by performing the *same* experiment in a semianechoic chamber. Since the cart is being moved by hand the speed will not always be uniform along the experience. Additionally if several experiences are performed, what can be actually compared (and give some information) is the position of the cart not the time variable. To be able to know the position of the moving source at each time instant a tachometer was placed at the bottom of the cart traveling with the moving source. The time–frequency coherences will be then represented as position–frequency plots (the position is the so called scheduling parameter, directly related to the time variable). It must be noted that, for this document, the speed that was considered for the moving source in the numerical case was exactly the one obtained by the tachometer in the experience here presented.

Figure 5.14(a) shows the PSD of this input signal for the case of the moving source (measured by the microphone); the peak at 150 Hz is clearly seen, but also a small peak at 75 Hz appears even if the emitted theoretical signal did not have this peak. This can be due to some reflections in the chamber. Figure 5.14(b) shows the PSD of the input signal for the static source (measured by the microphone); it is almost flat, as it should happen for a white noise, even if the magnitude is not completely constant for all the frequency range. Since both emitted signals are WSS their PSDs are shown just as a function of frequency.

For this experience signals, have been acquired with a sampling frequency of 8192 Hz. Since the frequency range of interest is from 50 to 500 Hz (where the microphones are able to correctly measure and the loudspeakers have the best performance), a resampling was performed to get a final sampling frequency of 1638.4 Hz. The total measurement time is 31.35 s, which makes a total number of samples of 51359.

Let us show the results obtained for the coherences with the three methods described in the previous section in this case. Figures 5.15(a), 5.16(a) and 5.17(a) show the ordinary coherence between the signal emitted by the moving source and the signal measured at the receptor point obtained with the STFT, the Unstructured TAR and the FS–TAR methods respectively. In these ones, it can be seen how at frequencies around 150 Hz, the coherence is very high for every position of the cart, as expected. In the rest of the frequency range it is observed that for positions around 2.8 m the coherence is higher, corresponding to the situation where the moving source is contributing more to the signal

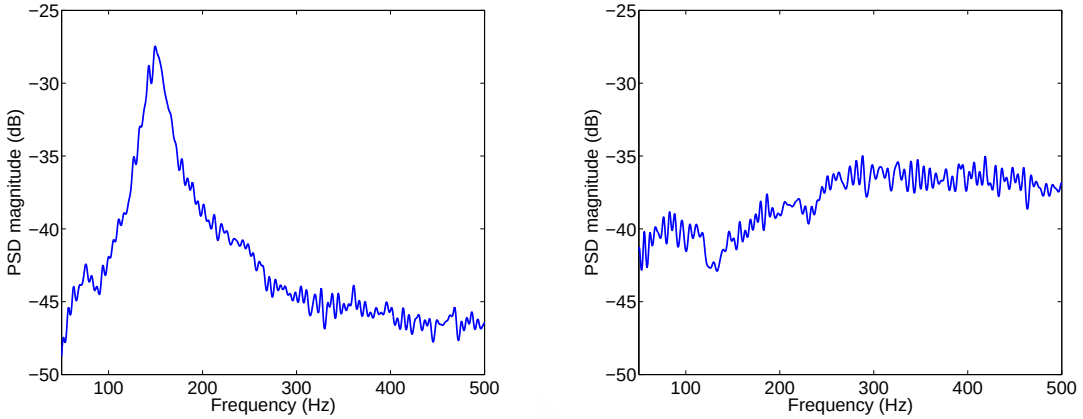

(a) (b)

Figure 5.14: PSD of the signals measured by the microphones next to each loudspeaker: (a) by the moving source, (b) by the static source.

received in the receptor than the static source. This is observed in the figures, since the maximum coherence of this moving source is observed around this position. Figures 5.15(b), 5.16(b) and 5.17(b) show the ordinary coherence between the signal emitted by the static source and the receptor obtained with the STFT, the Unstructured TAR and the FS–TAR methods respectively. Here a complementary behavior to the one described above can be observed. Finally Figures 5.15(c), 5.16(c) and 5.17(c) show the multiple coherence between both input signals and the signal at the receptor point obtained with the STFT, the Unstructured TAR and the FS–TAR methods respectively. Theoretically this last coherence should be equal to 1 since the only two sources of noise are being considered. In a laboratory experience this will not always be exactly true, but the fact that it was performed in a semi–anechoic chamber should help. It is actually seen how this coherence is really close to 1 for all methods.

It can also be seen that probably due to some reflections in the chamber, not only the frequency of 150 Hz has a high coherence in the case of the static source, but also at around 75 Hz, a high coherence is obtained. Comparing the three different methods considered, consistent results are obtained with all of them and the same comments as in the numerical experience are suitable.

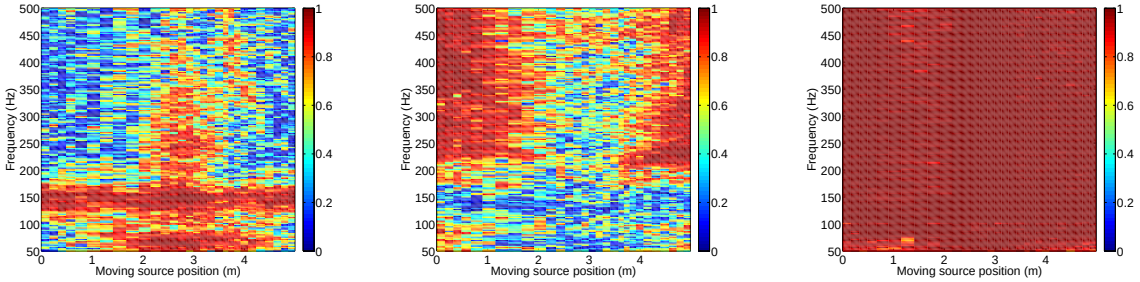

(a) (b) (c)

Figure 5.15: Coherences from the experimental case with the STFT method. (a) Ordinary coherence from the moving source; (b) ordinary coherence from the static source; (c) multiple coherence.

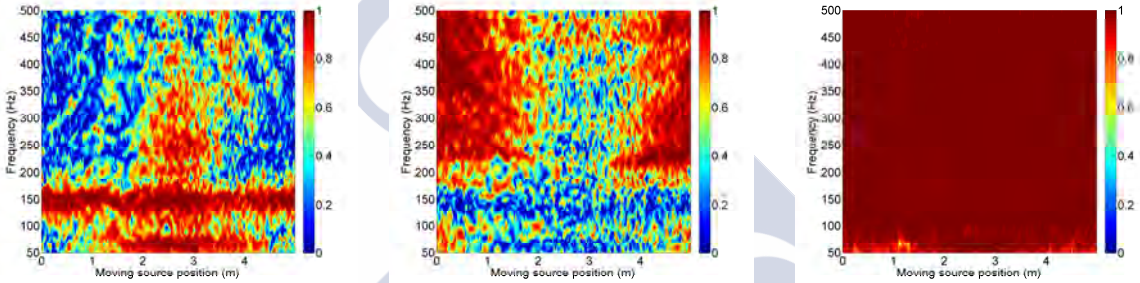

(a) (b) (c)

Figure 5.16: Coherences from the experimental case with the Unstructured TAR method. (a) Ordinary coherence from the moving source; (b) ordinary coherence from the static source; (c) multiple coherence.

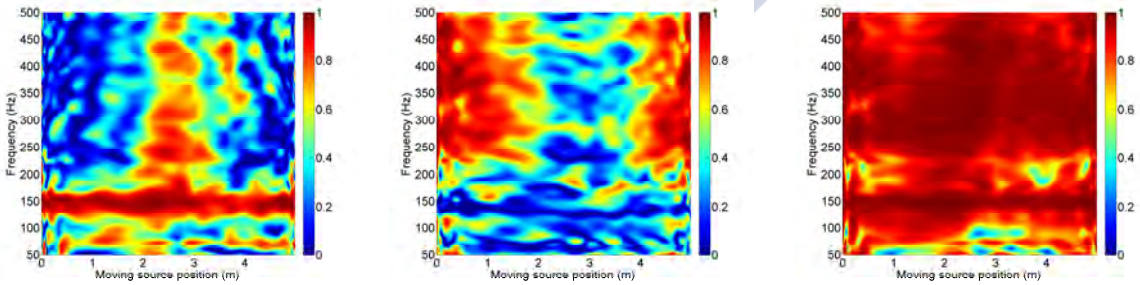

(a) (b) (c)

Figure 5.17: Coherences from the experimental case with the FS–TAR method. (a) Ordinary coherence from the moving source; (b) ordinary coherence from the static source; (c) multiple coherence.

5.3.4 Elevator signals analysis

Once a simple example for coherence computations has been presented a more elaborated one will be analyzed. In this section measurements coming from a real elevator measurement will be analyzed. First of all the object under study (elevator) will be presented. After this, a univariate analysis of only one signal is performed. Finally the full elevator system will be considered for coherence computations.

Presentation of the object under study

The elevator under investigation is operated by means of a drive machine (Permanent Magnet Synchronous Motor), ① in Figure 5.18. When operating, the drive machine pulley grips the hoist ropes (suspension cables) ② and moves the cabin ⑥ and counterweight ⑨. Both cabin and counterweight motion are directed by shoes ⑦ sliding along the guide rails ⑧ mounted along the sides of hoist way ⑩. The source of energy in the system is the drive machine. Its energy is mainly used to move the system but a part of it is dissipated producing vibrations and noise. This is the primary source for vibrations and noise. That energy propagates via different paths to the cabin and excites secondary sources causing vibrations and noise.

The elevator movement has three speed regions:

1. Initial acceleration region.
2. Constant speed region.
3. Final deceleration region.

The experience to be analyzed is a case in which the cabin is moving down from the 4th–top floor (where the drive machine is located) to the bottom one. The total measurement time is 25.2 seconds, but it will be divided into three zones according to the speed regions previously explained. The acceleration region corresponds to the range from the 1st till the 7th second of measurement; the constant speed region will include from the 4th second till the 18th; finally the deceleration region includes from the 17th till the 25th second. There is some overlap between regions to observe the transitions, and since the initial region was quite short, it includes part of the nominal speed region too. The sampling frequency used in the acquisition of the data was 16384 Hz, but a resample has been applied, since the interest of the work is in lower frequencies, so that the final sampling frequency is 2048 Hz.

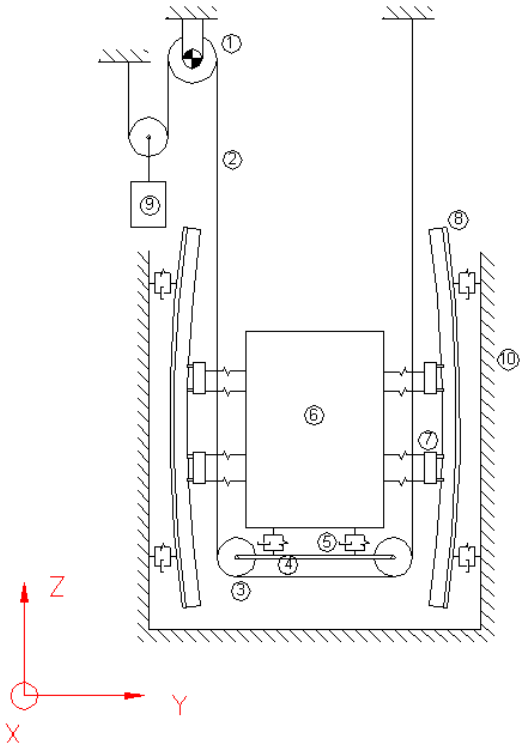

Figure 5.18: Sketch of the elevator under investigation: ① drive machine; ② hoist ropes (suspension cables); ③ sling pulleys; ④ beam supporting the cabin; ⑤ elastic elements; ⑥ cabin; ⑦ guide shoes; ⑧ guide rails; ⑨ counterweight; ⑩ hoist way.

The maximum speed of the cabin is 1 m/s. The deceleration does not happen at once, but in two steps, in between both of them that cabin stays for a few seconds at a lower speed, known as approximation speed. It is clear that the more non–stationary regions are the first and the third one, but even in the constant speed region, the cabin is moving apart from some of the noise sources, which may cause some non–stationarity.

For the application of the multiple coherence method the different sources need to be identified. In this case the knowledge of the object under study is used for the identification of the possible sources and paths. In this case the potential noise sources are:

- Cabin–related sources (moving together with the cabin):

  1. Rail–shoe system (4 systems: top left, top right, bottom left and bottom right).

2. Beam pulleys under the cabin (2 systems: beam left and beam right).

- Elevator well–related sources (fixed in the upper part of the well):

1. Drive machine.
2. Resistor.
3. Current inverter.
4. Speed limiter system.

Several microphones and accelerometers have been located near the identified sources (to be used as inputs), besides a microphone and an accelerometer (triaxial) were located inside the cabin, that will be the output (four possible outputs are available), see Figure 5.19. A tachometer was also used to measure the speed at which the elevator is traveling, even if its resolution is not very high, so for example the approximation speed cannot be properly captured. The total number of channels in the measurement is 44. The first 4 are the ones to be considered as output, from the other 40, 39 of them will be considered as inputs and the extra one corresponds to the tacho. These 39 inputs come from the 8 accelerometers (triaxial) and 15 microphones.

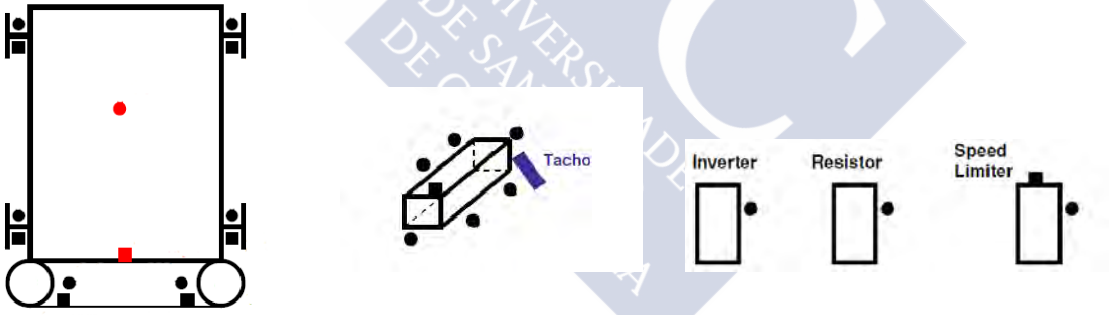

(a) (b) (c)

Figure 5.19: Measurement positions in the elevator analysis. Squares denote accelerometers and circles microphones. In red the receptor points, in black the noise sources and in blue the tachometer. (a) Cabin related sources, (b) drive machine, (c) other sources in the well.

Univariate analysis: acceleration signal from the drive machine of an elevator

In this more realistic experience, which includes a big number of inputs and outputs and longer signals, the computational cost has a more important role. An initial univariate

case will be studied in this subsection to evaluate this cost and decide the best way to tackle the bigger problem.

The signal considered, is the z direction of the accelerometer located on top of the drive machine. This choice is made because this is a signal with a rich frequency content and an important non–stationary behavior. Again, the three techniques will be applied and compared. Some limitations from the FS–TAR method, as applied in the scope of this paper will be presented. It can be seen that by reducing the time interval under study, the time dependency can be captured.

The drive machine has some theoretical characteristic frequencies related to the rotor speed that will be perfectly seen in the constant speed region. The main frequency for this specific drive machine is 31.83 Hz, but also all its harmonics are present, being the most important ones the 6^{th} at 190.98 Hz and the 24^{th} at 763.92 Hz. In the deceleration region there is a period in which the elevator moves at a lower speed (approximation speed), so that the final stop does not happen from the nominal speed but from a lower speed to increase comfort. In this region, the rotor speed is much lower (approximately divided by 12) so the frequencies observed are the ones indicated before also divided by the same factor. It must be noted that for the drive machine to maintain this low speed is more difficult and this is why oscillations can be seen when restricting the analysis to this specific part.

Figure 5.20 shows the results for the three techniques considering the full signal. It can be seen in Figure 5.20(c) that the last behavior in the approximation speed region is not perfectly captured for the FSTAR method, but can still be identified. The main problem is that the signal length limits the number of parameters that can actually be used, so a higher order is not always possible (an ill–conditioned matrix is obtained). To better capture these oscillations, above all with the FS–TAR method, an analysis of just the last seconds of the signal can be analyzed (even if the order problem will still exist, since now the signal is shorter). Results of this analysis are presented in Figure 5.21. Now the oscillations appear much clearer for the three methods and some tendencies are better seen for the FS–TAR method than for the other two methods, Figure 5.21(c).

Coherence computation from full system

Selection of the outputs considered It is clear that both noise and vibration in the elevator cabin play an important role in the trip comfort, see [57]. Concerning vibration, the z axis is the one which produces more discomfort at lower amplitudes of vibration,

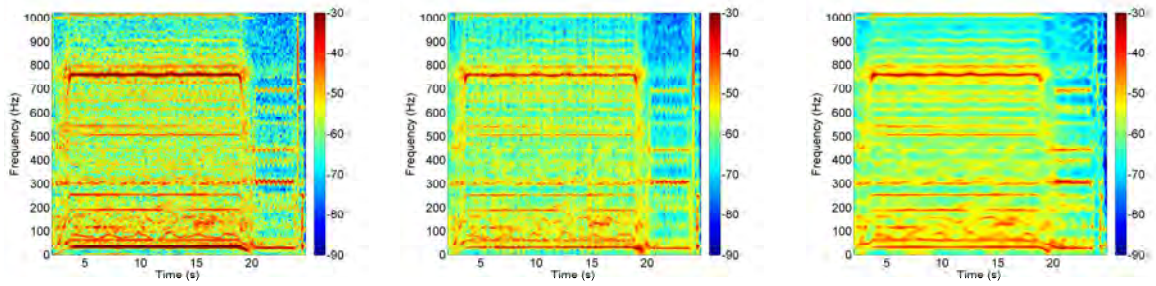

(a) (b) (c)

Figure 5.20: PSD in dB of the full signal from an elevator drive machine with three methods: (a) STFT, (b) Unstructured TAR and (c) FS–TAR.

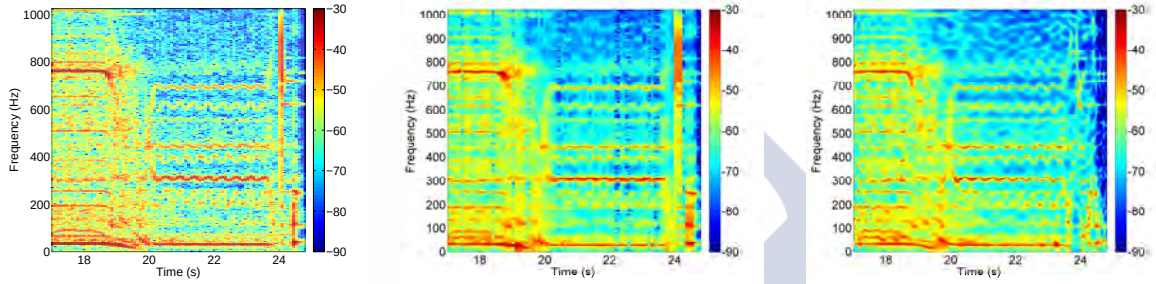

(a) (b) (c)

Figure 5.21: PSD in dB of the deceleration part signal from an elevator drive machine with three methods: (a) STFT, (b) Unstructured TAR and (c) FS–TAR.

see [51], Chapter 3. For this reason the outputs that will be considered are:

- Microphone in the cabin.
- z direction of accelerometer in the cabin.

It has to be taken into account that also the x and y directions are important in the comfort, but the study will be just limited to the z direction. Another reason to choose only the z axis is that, for the case of an elevator, this is the one with higher values of the acceleration since the movement is in this direction.

Preliminary considerations An initial check that will be made is the computation of the coherence from all inputs (the 39 channels) with the output, so that it is clear that the received output is actually caused by the measured inputs. For this to be true the coherence should be close to 1. This previous computation will give an idea of the *best result* that can be obtained. For this case, the computations have only been done with the Unstructured TAR method, the FS–TAR method presents some difficulties when a

model for 40 signals needs to be obtained. The results are shown in Figure 5.22 for the microphone case and in Figure 5.23 for the accelerometer case. In both cases Figures (a) show the results in the acceleration region, Figures (b) in the nominal speed region and finally Figures (c) in the deceleration region (for all coherence results in this section, this standard will apply).

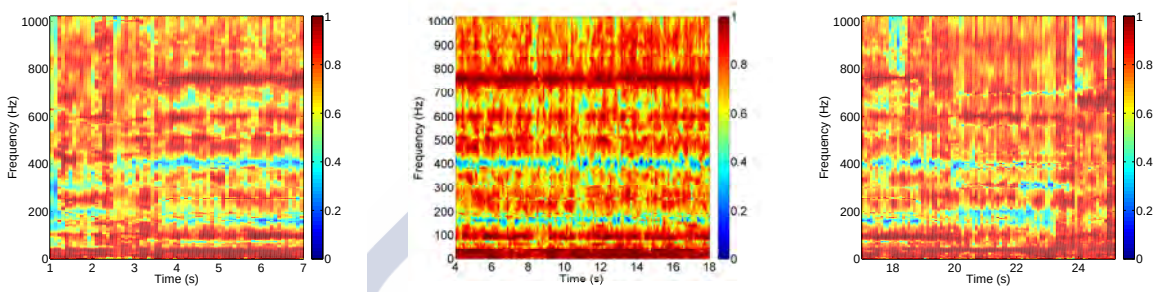

(a) (b) (c)

Figure 5.22: Coherences from all the inputs and the microphone for the three speed regions considered: (a) acceleration; (b) nominal speed; (c) deceleration.

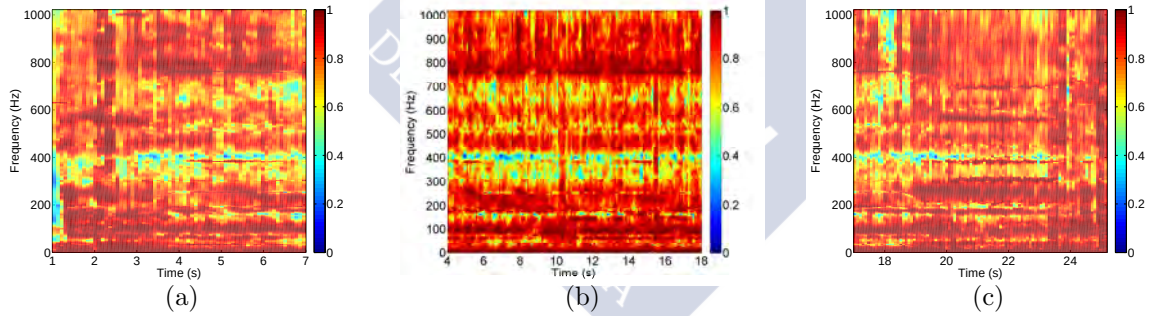

(a) (b) (c)

Figure 5.23: Coherences from all the inputs and the accelerometer (direction z) for the three speed regions considered: (a) acceleration; (b) nominal speed; (c) deceleration.

It can be seen that coherence is not exactly one for any of the cases. Some frequency ranges do not present a very high coherence, for example around 400 Hz, this can be due to some non linearities or to some non–measured source of noise or vibration. It is also clear that coherence is higher for the accelerometer case than for the microphone. It has to be taken into account that this is a very complex system in which there may be some other additional sources which cannot be actually measured. So taking everything into account, coherence of all the outputs is close enough to one.

Channel grouping As stated before, when the channels are coherent among them it will not be possible to separate their contributions. This will be the case for some particular frequencies (coming from the drive machine) that will be present in all the measured channels. Apart from this particular frequencies, some of the channels have very high coherence in almost all the frequency range and for all times. They will need to be grouped and their contribution will be considered together. For simplicity in the presentation of results and for consistency of the results, big groups with high enough coherence among them will be considered.

To start the analysis, once the inputs and the output have been identified, all the coherences between all inputs need to be computed due to the need to group the coherent ones. So, for each input pair a matrix (time–frequency) coherence is obtained. Some specific frequencies can be analyzed separately, for example some theoretic frequencies from the drive machine, as the ones seen in the previous subsection, since these will be present in almost all channels. For the frequency range of interest and/or for some time interval a mean value of the coherence is obtained. Once this has been done, a threshold is settled and groups will be computed with those inputs that have a high enough coherence. For the considered case the matrix of this mean coherence between all the input channels can be seen in Figure 5.24. A postprocessing is also sometimes needed to get more representative groups and also, in this case, for simplicity in the representation of results. For this reason the results will be presented distinguishing the three speed regions, and considering in all the same group division.

Some channels are not coherent among them and initially they should be considered separately. In this application these channels that are not grouped do not present a big coherence with the output so they will be discarded. This is the case of the six microphones in beam pulleys and rail shoe system. Once this six channels have been discarded, four big groups are considered:

1. **Group 1:** Left rail–shoe system: both accelerometers, all directions (6 channels).

2. **Group 2:** Right rail–shoe system: both accelerometers, all directions (6 channels).

3. **Group 3:** Beam pulleys and speed limiter: three accelerometers, all directions (9 channels).

4. **Group 4:** Motor and microphones from resistor, inverter and speed limiter: 9 microphones and the drive machine accelerometer (12 channels).

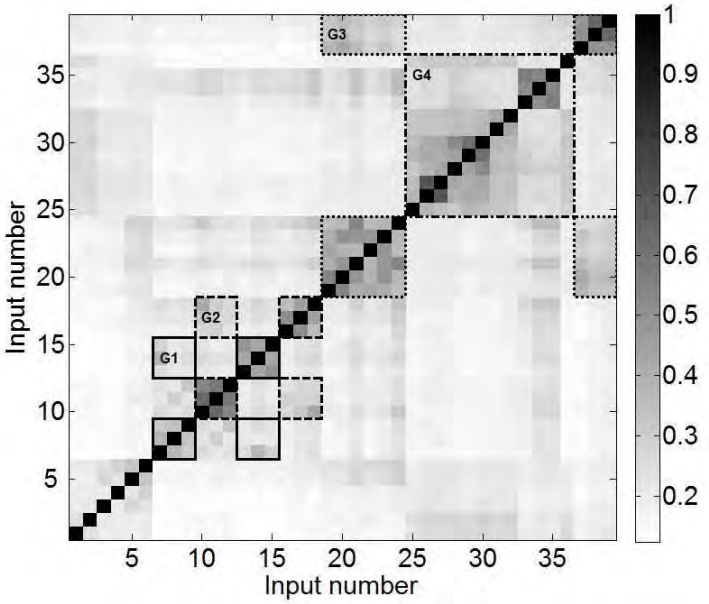

Figure 5.24: Representation of the division in groups.

Coherence results Now equivalent Figures for the four identified groups and the two outputs will be shown (in the three speed regions). Due to the big amount of Figures to be shown, not all the methods will be used in all the cases. All the Figures are shown for the Unstructured TAR method and some examples for G1 are shown for the STFT and the FS–TAR method. Figure 5.25 and Figure 5.26 present results for group 1 with the Unstructured TAR method, while Figure 5.27 and Figure 5.28 present the same results for the STFT and the FS–TAR methods respectively (only for the accelerometer output). The STFT results in this particular case are not good, it is clearly observed the high variability and the low resolution for this method. The FS–TAR method presents better results, even if it can be seen that for the first time instants and in some cases also for the last ones, the behavior is not very clean. Figure 5.29 and Figure 5.30 present results for group 2, Figure 5.31 and Figure 5.32 present results for group 3 and finally Figure 5.33 and Figure 5.34 present results for group 4.

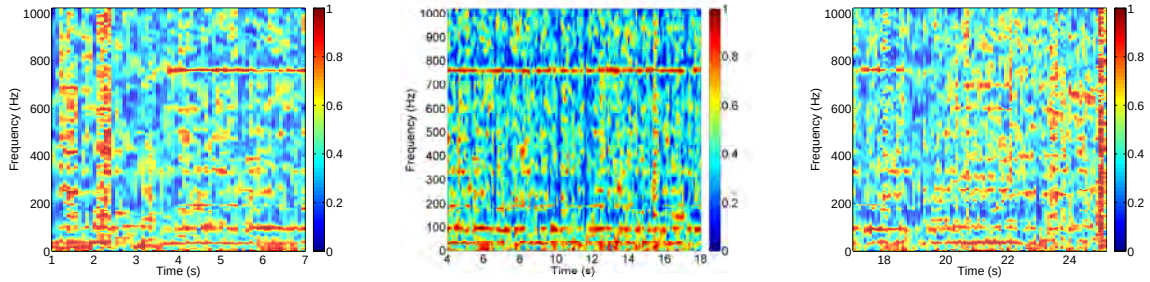

(a) (b) (c)

Figure 5.25: Coherences from inputs in group 1 and the microphone with the Unstructured TAR method for the three speed regions considered: (a) acceleration; (b) nominal speed; (c) deceleration.

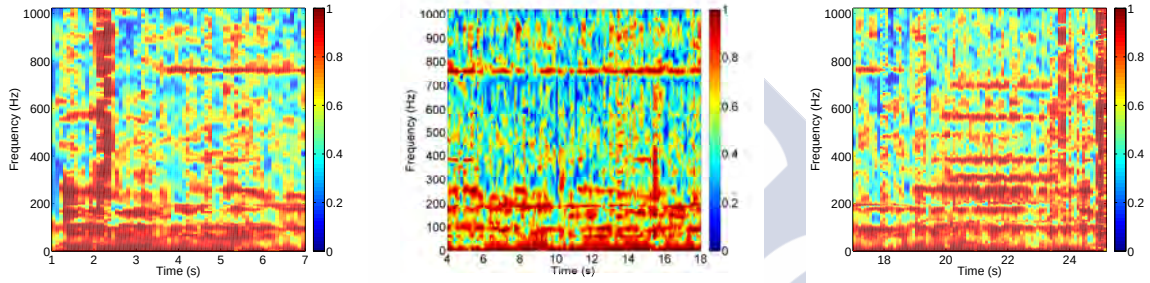

(a) (b) (c)

Figure 5.26: Coherences from all inputs in group 1 and the accelerometer (z direction) with the Unstructured TAR method for the three speed regions considered: (a) acceleration; (b) nominal speed; (c) deceleration.

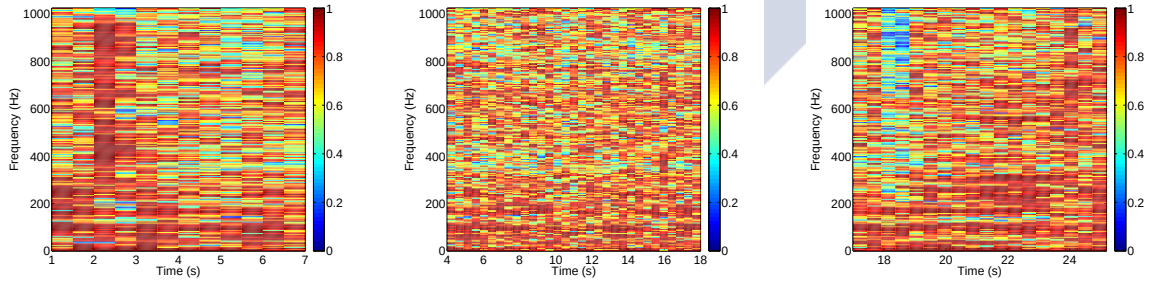

(a) (b) (c)

Figure 5.27: Coherences from all inputs in group 1 and the accelerometer (z direction) with the STFT method for the three speed regions considered: (a) acceleration; (b) nominal speed; (c) deceleration.

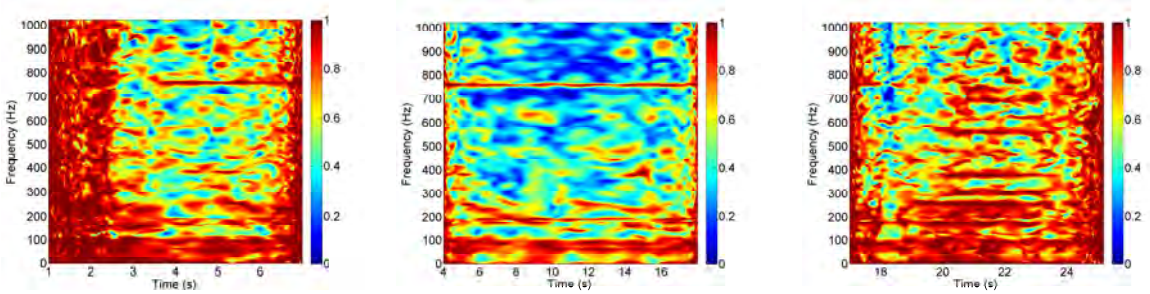

(a) (b) (c)

Figure 5.28: Coherences from all inputs in group 1 and the accelerometer (direction z) with the FS–TAR method for the three speed regions considered: (a) acceleration; (b) nominal speed; (c) deceleration.

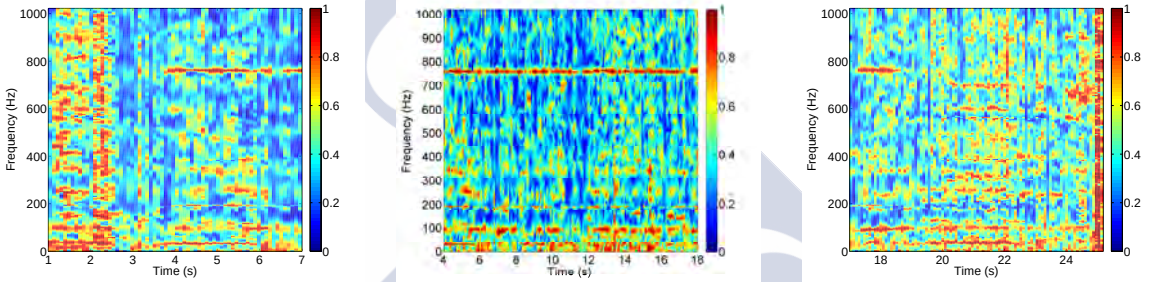

(a) (b) (c)

Figure 5.29: Coherences from inputs in group 2 and the microphone with the Unstructured TAR method for the three speed regions considered: (a) acceleration; (b) nominal speed; (c) deceleration.

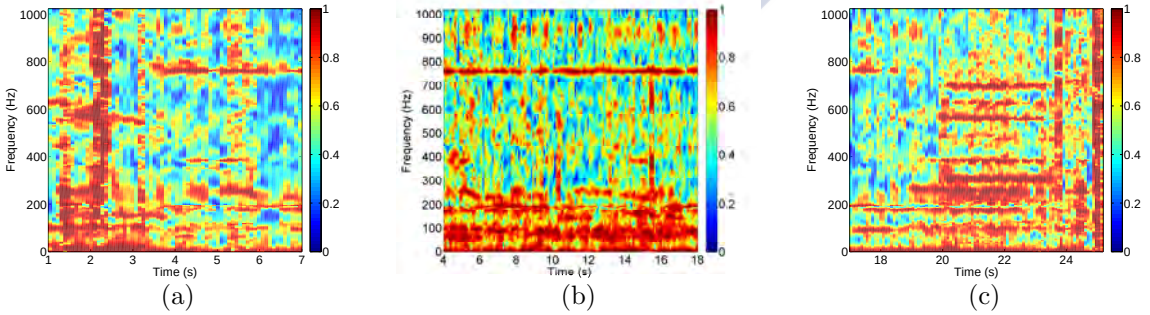

(a) (b) (c)

Figure 5.30: Coherences from all inputs in group 2 and the accelerometer (z direction) with the Unstructured TAR method for the three speed regions considered: (a) acceleration; (b) nominal speed; (c) deceleration.

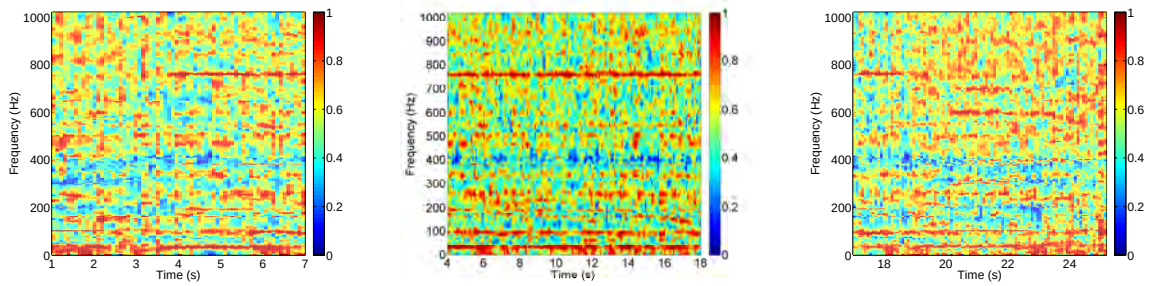

(a) (b) (c)

Figure 5.31: Coherences from inputs in group 3 and the microphone with the Unstructured TAR method for the three speed regions considered: (a) acceleration; (b) nominal speed; (c) deceleration.

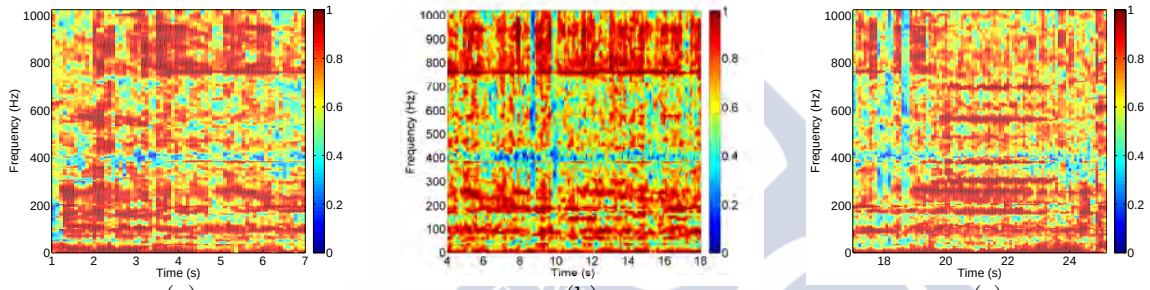

(a) (b) (c)

Figure 5.32: Coherences from all inputs in group 3 and the accelerometer (z direction) with the Unstructured TAR method for the three speed regions considered: (a) acceleration; (b) nominal speed; (c) deceleration.

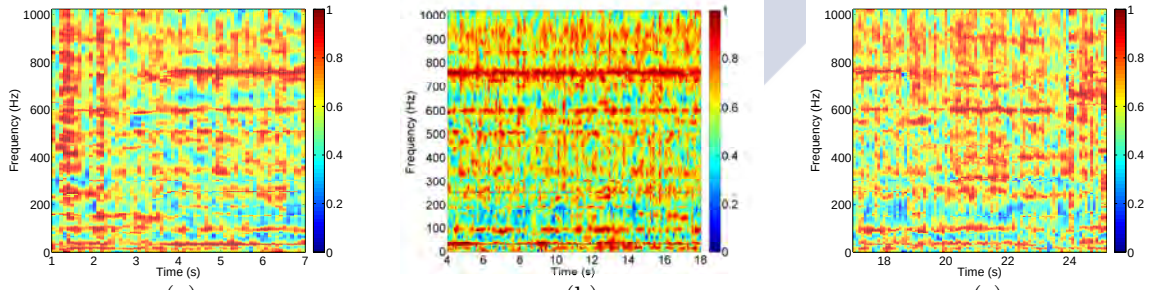

(a) (b) (c)

Figure 5.33: Coherences from inputs in group 4 and the microphone with the Unstructured TAR method for the three speed regions considered: (a) acceleration; (b) nominal speed; (c) deceleration.

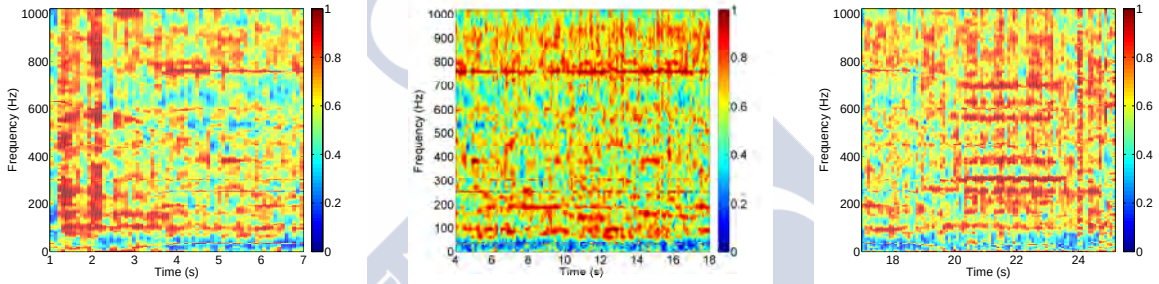

(a) (b) (c)

Figure 5.34: Coherences from all inputs in group 4 and the accelerometer (z direction) with the Unstructured TAR method for the three speed regions considered: (a) acceleration; (b) nominal speed; (c) deceleration.

Results for all the groups are summarized in the following:

- The first two groups associated with the rail–shoe system, Figures 5.25–5.30 do not have a very high coherence with any of the outputs (except for low frequencies in the accelerometer case, Figure 5.26 and 5.30).
- Group 3 presents higher coherence, being the predominant one for the case of the accelerometer, see Figure 5.32. This group is associated with the beam pulleys.
- For the microphone, it is the group 4 the one with the main contribution, see Figure 5.33. This group is the one related with the drive machine.

This difference has a natural interpretation, since the beam pulleys will cause more vibration than noise in the cabin, whereas all the inputs related to the drive machine will actually cause noise received in the cabin. As it has already been seen before, the total coherence of all inputs in the microphone was lower than the one in the accelerometer, and this is also observed in these results. This is related to the fact that structure–borne contributions are greater than air–borne contributions. In fact, also for this it is not observed a decrease with time of the coherence, even if the cabin is moving apart from some of the noise sources.

It is also clear that some of the theoretical frequencies from the drive machine are actually present in all the channels, so their contribution cannot be actually separated. Since their origin is already clear, this is not a big issue.

5.4 Conclusions

In this chapter three different techniques, namely the STFT, the Unstructured TAR and the FS–TAR methods have been used to obtain coherences between non–stationary signals. The STFT method has a high variability, both in time and in frequency, this leads to a reduced time resolution due to the necessity of making time averages. The Unstructured TAR method presents some advantages over the STFT methods having better time (no need of averages) and frequency (as it is parametric) resolution. The last method, the FS–TAR, is parametric both in time and in frequency giving an estimate with less variance than the previous ones and better spectral and temporal resolution. The selection of the basis functions is crucial when the signal has some sharp transition, if polynomials are chosen, the results will be smoothed which may not be the true underlying behavior.

A specific novelty of the present chapter is the use of the Bernstein polynomial family for the variance estimation. With this selection the estimation of the variance becomes easier (there is no need to compute the coefficients) and the properties of positiveness (univariate case) and positive definiteness (multivariate case) are immediately obtained. Another important issue for parametric methods is the model order selection. It must also be noted that when big groups are considered the FS–TAR method may not be an appropriate option due to the high computational cost and the importance of this order selection that may lead to erroneous results.

Concerning the computational cost, the STFT is the fastest method of the three, and it could be even parallelized (time blocks can be treated independently) and get better results. The Unstructured TAR method has a higher computational cost, although this can also be improved by parallelizing the code. Finally the FS–TAR method is the slowest method of the three, it needs to be taken into account that no optimization was made in the code for computing the parameters, so it is possible that a considerable improvement on the computational burden can be achieved.

The methods presented have been applied in the context of coherence computations. Two experimental experiences have been analyzed:

- The first one was performed in a semianechoic chamber involving only two sources, a static and a moving one. For this case stationary signals are emitted and the non stationarity of the coherences comes from the movement of one of the sources. The expected results are obtained, the moving source contributes more when it is nearer to the receptor.

- The second experience involves a true elevator system. Big groups with high coherence among its channels have been analyzed and two outputs have been considered: a microphone and the z direction of an accelerometer, located both in the cabin. For the microphone it was obtained that the predominant group is the related to the drive machine, whereas for the accelerometer, it is the one from the beam pulleys (which causes more vibration).

The importance of the introduction of the time variable was assessed with both experiences, where stationary methods would have not been able to give appropriate results. A real complex system was also analyzed with this coherence technique being able to obtain the predominant sources and paths in different cases.

USC
UNIVERSIDADE
DE SANTIAGO
DE COMPOSTELA

Chapter 6

Conclusions and future work

In this thesis two different problems have been addressed. The first of them involves damage detection and identification in the field of wind turbines. The second of them involves coherence computations of non–stationary signals, in particular in the case of elevator measurements. Conclusions will be divided in these two big groups.

6.1 Damage detection and identification: application in the wind turbine field

Several problems have been addressed in this context considering as test cases:

- A lab–scale wind turbine tower with and without jacket (off–shore).
- A lab–scale blade.

Precisely the problems tackled have been:

1. Vibration–based damage detection and identification via AR parametric modeling was considered in Chapter 2. A lab–scale wind turbine tower, with and without jacket was considered for damage detection and identification. In particular, several conclusions were obtained from these experiments:
    - Damage can be detected with the selected methodology, even if the false alarm and missed damage rates are not zero for all the cases.
    - It was observed that the y (fore–aft) direction was the best for damage detection.

- Damage can also be identified in the case where a learning process is possible.

2. Vibration–based damage detection under varying environmental conditions and uncertainty was considered in Chapter 3. In this field several conclusions were drawn:

   - A novel supervised PCA–type statistical methodology was postulated which aims at high detection performance even with a very limited number of sensors, low frequency and limited bandwidth.
   - It employs data records from the healthy and damaged states under various conditions, and a sequential procedure to select the transformed scalar element that should be added to the feature vector.
   - Their laboratory validation and comparative assessment was based on an experimental case study focusing on damage detection on a scale wind turbine blade under varying temperature and the potential presence of sprayed water.
   - Results obtained are characterized by almost no false alarms and undetected damage rate below 3%.

3. Vibration–based damage localization was considered in Chapter 4. In particular, conclusions may be summarized in:

   - A supervised damage localization methodology based on a FP–ARX model was used to locate the damage (added mass) on a lab–scale wind turbine blade.
   - For positions used in the baseline phase, errors below 2cm are obtained.
   - For not trained positions, localization errors are very low: below 5cm for almost all data records, even for those positions not in the central axis of the blade.

6.1.1 Future research

Even if the results shown in this document have very high success rates it must be noted that, when it comes to reach level 2 (identification/localization of the damage) or to account for several environmental and operational conditions, *supervised* methods have been used. It is clear that supervised methods have obvious disadvantages for practical implementations, since not always damaged data records are available in real applications. In some cases due to the cost, or in others due to the difficulties to foresee in advance the possible damages that can occur, it is likely that one cannot have available damaged data records.

Some possibilities to overcome this problem would include:

- Consider replacing measured data records by numerically obtained ones, to use in the baseline. The main problem in this case is to have an accurate model that still remains accurate when applying a damage. In general to validate a model it is also needed to have the structure in the same condition and perform some Operational Modal Analysis (OMA) or other procedures to update the model in different conditions.

- For the case of different environmental and operational conditions it could be tested if a subsequent bigger damage would have also been detected with the selected feature vector.

6.2 Multiple coherence computations: application to an elevator

Non–stationary signals have been broadly studied in the literature and several time–frequency representations involving different models have been presented.

In this thesis, Chapter 5, three of them, namely: the STFT, the Unstructured TAR and the FS–TAR have been analyzed and compared. In particular they have been used for coherence computations in a simple laboratory case and also in a more complex real elevator system. Multiple coherence has not been used previously in such a complex system with the aim of identifying predominant sources and paths of noise and vibration.

Additionally, Bernstein polynomials were introduced in the computation of coefficients where AutoRegressive estimation was used. In particular for coherence computations the positiveness or positive definiteness of the variances involved is of crucial importance. Due to their properties, Bernstein polynomials have several advantages with respect to other possibilities, in particular:

- Coefficients do not need to be computed since they are explicitly values from the function to be approximated on a equispaced grid.

- Since they are positive in all the interval, and since the coefficients are positive numbers (univariate case) or positive definite matrices (multivariate case)–as they are values of the function to be approximated–the approximated versions also maintain these properties.

In particular in the elevator application it was obtained that for the microphone output the predominant group is the related to the drive machine, whereas for the z direction (vertical) of the accelerometer output, it is the one from the beam pulleys (which causes more vibration). It was checked that the structure–borne contributions have more influence in the noise and vibration received in the cabin. This fact also explains why the relative movement of the cabin with respect to the noise sources does not imply a decrease in the coherence when the cabin is moving apart from them.

6.2.1 Future research

There are some limitations in the applied techniques, above all when the objective is to analyze a very big system with many inputs considered. The first of them is the computational cost which becomes too high, mainly when the FS–TAR method is used. Another drawback arises when the signal has steep changes.

In this sense some improvements could be:

- Whenever possible the code could be parallelized.
- Some computational techniques to speed up the obtention of the coefficients could be analyzed.
- Use of splines or other functional basis with better properties depending on the particular application under study.

Appendix A

Polynomial families

In this appendix the main polynomial families used along this document are briefly described.

A.1 Chebyshev polynomials

The polynomials used in this study are the shifted Chebyshev polynomials of the second kind (Type II Chebyshev polynomials), which belong to the broader family of Chebyshev orthogonal polynomials, see [84, Chapter 18], [2]. These polynomials in their original form (to be evaluated in the interval $[0, 1]$) obey the following recurrence relation:

$$\begin{aligned} &U_0^*(x) = 1; \qquad U_1^*(x) = 4x - 2; \\ &U_{n+1}^*(x) = (-2 + 4x)U_n^*(x) - U_{n-1}^*(x), x \in [0, 1] \subset \mathbb{R}. \end{aligned} \tag{A.1}$$

Hence, the first five shifted Chebyshev polynomials of the second kind are:

$$\begin{aligned} U_0^*(x) &= 1 \\ U_1^*(x) &= 4x - 2 \\ U_2^*(x) &= 16x^2 - 16x + 3 \\ U_3^*(x) &= 64x^3 - 96x^2 + 40x - 4 \\ U_4^*(x) &= 256x^4 - 512x^3 + 336x^2 - 80x + 5. \end{aligned}$$

For the particular application of chapter 4, the interval $[k_{\min}, k_{\max}]$ in which the minimum needs to be found is mapped to the interval $[0, 1]$.

A.2 Legendre polynomials

The Legendre polynomials [84, Chapter 14], [4] may be defined in several different ways, but only its recursive definition will be given here.

$$\begin{aligned} &P_0(x) = 1; \qquad P_1(x) = x; \\ &(n+1)P_{n+1}(x) = (2n+1)xP_n(x) - nP_{n-1}(x), x \in [-1,1] \subset \mathbb{R}. \end{aligned} \tag{A.2}$$

Hence, the first five Legendre polynomials are:

$$\begin{aligned} P_0(x) &= 1 \\ P_1(x) &= x \\ P_2(x) &= \frac{1}{2}(3x^2 - 1) \\ P_3(x) &= \frac{1}{2}(5x^3 - 3x) \\ P_4(x) &= \frac{1}{8}(35x^4 - 30x^2 + 3). \end{aligned}$$

A.3 Bernstein polynomials

The $n+1$ Bernstein basis polynomials of degree n are defined as [1], [20, Chapter VI]:

$$b_{\nu,n}(x) = \binom{p}{n} x^{\nu}(1-x)^{n-\nu}, \qquad \nu = 1, \ldots, n,$$

where $\binom{p}{n} = \dfrac{p!}{n!(p-n)!}$ is the binomial coefficient.

A linear combination of Bernstein polynomials:

$$B_n(x) = \sum_{\nu=0}^{n} \beta_\nu b_{\nu,n}(x),$$

is called a Bernstein polynomial or polynomial in Bernstein form of degree n. The coefficientes β_ν are known as Bernstein coefficients.

The first few Bernstein polynomials are:

$$\begin{aligned} &b_{0,0}(x) = 1 \\ &b_{0,1}(x) = 1 - x, \qquad b_{1,1}(x) = x \\ &b_{0,2}(x) = (1-x)^2, \quad b_{1,2}(x) = 2x(1-x), \quad b_{2,2}(x) = x^2 \\ &b_{0,3}(x) = (1-x)^3, \quad b_{1,3}(x) = 3x(1-x)^2, \quad b_{2,3}(x) = 3x^2(1-x), \quad b_{3,3}(x) = x^3. \end{aligned}$$

Given a function, $f(x)$ in the closed interval $[0, 1]$ its Bernstein polynomial of order p is given by:

$$B_p(x) = B_p^f(x) = \sum_{n=0}^{p} f\left(\frac{n}{p}\right) \binom{p}{n} x^n (1-x)^{p-n},$$

These polynomials have important properties regarding uniform convergence to the original function [78, 20].

USC
UNIVERSIDADE
DE SANTIAGO
DE COMPOSTELA

Appendix B

Resumen extenso

En aplicaciones reales, las series temporales aparecen constantemente. El presente trabajo está dedicado al análisis de varias metodologías de estas series temporales. En particular la tesis se orienta principalmente en dos campos:

- *Monitorización de la salud estructural* (SHM, por sus siglas en inglés *Structural Health Monitoring*): se han utilizado métodos paramétricos y no paramétricos para la detección de daños (Capítulo 2), también en el caso de variación de las condiciones medioambientales (Capítulo 3) y, además, también se evalúa la localización del daño (Capítulo 4). Para esta aplicación se consideran solamente señales estacionarias. Las estructuras elegidas en el que se han testeado los métodos están relacionados con el campo de la energía eólica. En particular, se han utilizado una torre a escala de laboratorio (Capítulo 2) y palas de aerogenerador a escala (Capítulos 3 y 4).

- Análisis de *señales no estacionarias*, utilizando varias técnicas (paramétricas y no paramétricas) y la aplicación de estas técnicas para obtener coherencias (Capítulo 5). Se presentan algunas aplicaciones numéricas, de laboratorio y en situaciones reales de las metodologías. Los ensayos de laboratorio se simulan primero numéricamente y luego se reproducen en una cámara semianecoica. Finalmente se analiza una aplicación real, en concreto un sistema de ascensor completo.

El resto de este capítulo se organiza de la siguiente manera: en las secciones B.1 y B.2 se introducen y se muestra el estado del arte de la monitorización de la salud estructural y del análisis de señales no estacionarias (incluyendo el cálculo de coherencias) respectivamente, mientras que en la sección B.3 se presenta la organización del resto de la tesis incluyendo los objetivos y contribuciones de cada capítulo.

B.1 Monitorización de la salud estructural

Structural Health Monitoring (SHM) se define como el proceso de adquisición y análisis de los datos de los sensores integrados para evaluar la salud de una estructura. Las principales características inherentes a cualquier sistema SHM es que los sensores tienen que ser integrados, incrustados o permanentemente unidos a la estructura, lo que conduce a la principal ventaja del SHM en comparación con ensayos no destructivos (NDT, por sus siglas en inglés *Non–destructive Testing*): el proceso de inspección puede ser automatizado, sin necesidad de desmontarlos. Esto permite que la estructura sea continuamente monitorizada incluyendo capacidades de procesamiento dentro de la estructura, mientras que por lo general el NDT se realiza periódicamente o bajo demanda. Por lo tanto SHM ofrece grandes ahorros en los costes de mantenimiento (para aviones, puentes y otras infraestructuras).

Según [7] SHM tiene como objetivo dar, en cada momento durante la vida de una estructura, un diagnóstico del "estado" de los materiales constituyentes, de las diferentes partes, y del conjunto de estas partes que constituyen la estructura completa. El estado de la estructura debe permanecer en el dominio especificado en el diseño, aunque esto puede ser alterado por el envejecimiento normal debido al uso, por la acción del medio ambiente, y por sucesos accidentales. Los daños en las estructuras han causado muchos desastres en el curso de la historia como se puede ver en la Figura B.1. Esto ha atraído la atención de la comunidad relacionada con las técnicas de construcción y mantenimiento de estructuras, tales como puentes [108].

Figure B.1: Ejemplo de evento catastrófico: turbina eólica rota.

Según [14] SHM es la integración en una estructura de sensores y dispositivos (actuadores) que permitan registrar condiciones de carga para analizar, localizar y predecir los posibles daños, de manera que los ensayos no destructivos (NDT) se convierten en una

parte integral de la estructura o del material.

En vista de las definiciones anteriores se hace evidente que SHM implica la detección de *daño*, pero ¿qué se entiende por daño? Según [35] en términos generales, el daño puede ser definido como los cambios introducidos en un sistema que afectan negativamente su rendimiento actual o futuro. Implícito en esta definición esta el concepto de que un daño no es significativo sin una comparación entre dos estados diferentes del sistema, uno de los cuales se supone que representa el estado inicial, y con frecuencia sin daños.

B.1.1 Niveles en la diagnosis del daño

Según Rytter [93] se pueden distinguir cuatro niveles de daño en SHM, estos se muestran en la Tabla B.1.

Nivel	*Descripción*
1	Determinación de la existencia de daño estructural
2	Nivel 1 más identificación/localización del daño
3	Nivel 2 más cuantificación del daño
4	Nivel 3 predicción de la vida restante (prognosis)

Table B.1: Niveles de detección de daño.

El primer nivel analiza la detección del daño (estudia la presencia o ausencia de daño estructural) . El segundo nivel también incluye la identificación (tipo de daño) y la localización del daño detectado. En el tercer nivel, además de la identificación y la localización del daño, se evalúa su extensión, magnitud o severidad, mientras que el cuarto nivel predice, además, la vida útil restante de la estructura dañada.

La mayor parte de los trabajos existentes se centran en los niveles 1 a 3, el cuarto nivel implica en general un conocimiento más profundo y una comprensión física de la estructura bajo estudio, por lo que ha recibido menos atención en la literatura, ya que es el más complicado de lograr. En el ámbito del presente trabajo se abordarán solo los dos primeros niveles.

B.1.2 Detección de daño – Nivel 1

Los métodos de detección de daño tradicionales están basados en ultrasonidos, acústica, corrientes inducidas o principios térmicos [27]. El principal problema es que requieren

acceso a un entorno de la zona potencialmente dañada, por lo que la información respecto a la posible localización del daño necesita ser conocida a priori, lo cual no siempre es posible. En general, estas técnicas han sido validadas a través de vigas simples o estructuras tipo placa, en lugar de las estructuras reales. Además, la mayoría de ellos son caros y requieren una alta inversión de tiempo.

Un enfoque alternativo que trata de superar estas dificultades son los *métodos basados en vibraciones* [37].

Métodos basados en vibraciones

Los métodos de de SHM basados en vibraciones forman una familia tecnológicamente importante. La idea principal de estos métodos es que las pequeñas variaciones en una estructura causan cambios en la respuesta vibratoria que se pueden detectar. Algunos de los métodos basados en vibraciones se basan en las frecuencias naturales [52, 71], otros en formas modales [5, 73] o en energía de deformación modal [64]. Worden *et al* [109] desarrolló un método utilizando el análisis de valores atípicos para la detección de daños. El análisis de Componentes Principales (PCA, por sus siglas en inglés *Principal Component Analysis*) se utilizó en [21] para la detección y localización de daños estructurales. Un novedoso método de análisis basado en el modelo de Kalman se propuso recientemente en [113].

Estos métodos ofrecen una serie de ventajas, sobre todo en el sentido de que no requieren inspección visual, son globales (cubren grandes áreas con solo unos pocos sensores), son capaces de trabajar a nivel de sistema, pueden ser potencialmente utilizados bajo excitación ambiente, se puede automatizar y también tienden a ser efectivos en tiempo tiempo y coste [95, 27, 91].

En la presente subclase se pueden hacer otras clasificaciones adicionales:

- Métodos *paramétricos* frente a *no paramétricos*.
- Métodos que utilizan *solo la respuesta* frente a los métodos que usan ambas *excitación y respuesta*.
- Métodos *supervisados* frente a métodos *no supervisados* (en referencia al hecho de utilizar o no datos de la estructura dañada en la fase de aprendizaje).
- Métodos *escalares* (univariables) frente a *vectoriales* (multivariables).
- Etc.

En el ámbito de este trabajo se considerarán principalmente las tres primeras clasificaciones cubriendo las diferentes opciones. En todos los capítulos referentes a la diagnosis del daño solo se usarán métodos escalares. Merece la pena mencionar también que en la diagnosis del daño solo se tendrá en cuenta la dinámica invariante en el tiempo (bajo condiciones estacionarias) de las estructuras consideradas.

Los métodos basados en vibraciones no paramétricos para SHM se basan, por ejemplo, en estimaciones de la densidad de potencia espectral (PSD, por sus siglas en inglés *Power Spectral Density*) [37, 72], o en funciones de respuesta en frecuencia (FRF, por sus siglas en inglés *Frequency Response Function*) [90]. Los métodos paramétricos se basan en correspondientes representaciones de series temporales. Un ejemplo ampliamente utilizado es el modelo AutoRegresivo [77, 61], que caracterizará la estructura en el estado sano. El daño será detectado mediante la comparación de una característica en un estado desconocido con la correspondiente en el estado sano. Este tipo de métodos han recibido considerable atención en la literatura [37, 82]. Una caso más general mediante métodos AutoRegresivos de Media Móvil (ARMA, por sus siglas en inglés *AutoRegressive Moving Average*) o modelos AutoRegresivos con entradas eXógenas (ARX) se analiza en [101] y [76]. Un método basado en identificación de subespacios y residuos del modelo de espacio de estados se estudia en [9].

Los *métodos estadísticos de series temporales para SHM* forman una clase importante dentro del contexto de métodos SHM basados en vibraciones. Sus tres elementos principales son:

i) Excitación aleatoria y/o señales de respuesta vibracional.

ii) Construcción de modelos estadísticos.

iii) Toma de decisiones en base a inferencia estadística para decidir el estado de salud de la estructura.

Estos métodos involucran dos fases diferentes: inicialmente en una *fase de referencia* (*entrenamiento* o *aprendizaje*), los métodos emplean señales de vibración aleatoria y/o la respuesta a dicha excitación obtenidas de la estructura en su estado sano (a veces también de algunos posibles escenarios dañados) y obtienen un modelo estadístico, paramétrico o no paramétrico, que describe la estructura en el estado considerado. A continuación se extrae una *elemento característico*, para caracterizar la estructura dicho estado (en general sano). En la *fase de inspección* dada una nueva serie temporal, en un estado desconocido, el método usa la toma de decisión estadística para decidir si la

estructura está realmente dañada o sin daño. En algunos casos, también se puede alcanzar una identificación/localización del daño. Otra ventaja de este tipo de métodos es que inherentemente tienen en cuenta ciertas incertidumbres, ya que utilizan herramientas estadísticas.

Los métodos basados en vibraciones pueden ser basados en *datos* [33, 9] o en la *física*, basados en general en modelos de elementos finitos, [27]. En el contexto del presente trabajo solo se tendrán en cuenta los métodos basados en datos. Esto es una ventaja para muchas aplicaciones, ya que un modelo físico no siempre estará disponible y, además, incluso en los casos en que un modelo esté disponible, puede ser computacionalmente muy costoso. Una ventaja adicional es que se generalizan más fácilmente en diferentes contextos y estructuras, debido al hecho de que solo se utilizan señales de respuesta (y tal vez también las señales de excitación) y no son dependientes de la aplicación concreta.

B.1.3 Localización del daño – Nivel 2

La localización del daño se corresponde al nivel 2 de la Tabla B.1 anteriormente presentada.

En el contexto de métodos basados en vibraciones, la localización de daño se ha abordado, en general, a través de modelos complejos y detallados (típicamente modelos de elementos finitos) utilizando las señales de vibración y procedimientos de actualización de modelos (*model updating*). La necesidad de un modelo detallado puede ser un inconveniente para algunas aplicaciones. Además, los daños considerados necesitan ser simulados en los modelos y algunos parámetros identificados para ser actualizados con las mediciones de vibraciones en el caso dañado [98, 59]. En la práctica, tal procedimiento típicamente requiere grandes modelos de elementos finitos y varios sensores para una adecuada actualización de los modelos [10, 22]. En estos casos el daño se localiza dentro de un elemento finito particular.

Dentro del contexto de los enfoques basados en datos, el subproblema de la localización de daño se ha abordado como un problema de clasificación en el que el estructura se divide en un número de regiones o elementos (por ejemplo un elemento finito concreto), y el daño se localiza en alguno de ellos [67, 111]. En [94] se considera el problema de la localización *precisa* del daño, en el sentido de que se considera la topología completa de la estructura y se estiman las coordenadas específicas de la posición del daño a través de un novedoso método basado en un modelo funcional (FMBM, por sus siglas en inglés *Functional Model Based Method*), que también puede ser utilizado para la cuantificación daño o la consideración de condiciones medioambientales cambiantes.

B.1.4 Consideración de condiciones medioambientales y operacionales cambiantes

Una limitación importante de los métodos basados en vibraciones es que los cambios en la dinámica pueden ser también causados por la variación de las condiciones ambientales o por la propia incertidumbre. Esto limita potencialmente el rendimiento y la fiabilidad del diagnóstico de daños [62]. Esto también es cierto para los métodos estadísticos, que aunque representan ciertos tipos de incertidumbre, todavía no tienen en cuenta las condiciones ambientales y las incertidumbres no empleadas durante su fase de aprendizaje (de referencia).

El problema de hacer frente de manera efectiva a diferentes condiciones medioambientales y la incertidumbre es, por tanto, de vital importancia y una barrera de cara a la aplicación de estas tecnologías. El enfoque general para superarla implica, en términos generales, un adecuado "preprocesamiento" de las medidas de vibración en bruto o de la característica seleccionada, con el objetivo de "eliminar" los efectos de la incertidumbre. Tal preprocesamiento puede ser basado en modelos o no basado en modelos, y también se conoce como "normalización de datos" (véase [99] para una visión general).

En la primera clase de métodos (basados en modelos), se supone que las condiciones medioambientales y la incertidumbre son *medibles*, por lo que sus efectos en la dinámica pueden ser correctamente cuantificados y modelados, lo que resulta en su potencial separación de los efectos de los daños. Esto se puede conseguir a través de *métodos multi–modelo*, en los que se obtiene un modelo individual para cada condición específica, y luego éstos se relacionan/vinculan entre sí. Tales métodos establecen relaciones entre los parámetros modales (por ejemplo, frecuencias propias) y las condiciones medioambientales (como la temperatura) por medio de técnicas de regresión o de interpolación [110], fórmulas de corrección [63], modelos ARX [85], o filtros lineales [100]. Se han utilizado también técnicas de *clustering* (agrupación) para diferentes condiciones medioambientales [70]. A diferencia de los métodos multi–modelo, también se han utilizado *métodos globales* (conocidos como *Functionally Pooled models*) [56], capaces de describir los efectos de las condiciones medioambientales medibles en la propia dinámica. La principal limitación de estos métodos se debe al hecho de que las incertidumbres no son siempre medibles, en cuyo caso no pueden ser debidamente tenidas en cuenta.

La segunda clase de métodos (no basada en modelos) se basa en la adecuada manipulación ("preprocesamiento" o transformación) de la magnitud característica seleccionada, de manera que su versión transformada siga siendo sensible al daño, pero insensible a los

cambios en las condiciones ambientales y la incertidumbre. Estos métodos son a menudo más simples que su contrapartida basada en modelos y no requieren que las incertidumbres sean medibles. Incluyen métodos basados en el Análisis de Componentes Principales (PCA) [40, 114, 45, 11], que transforman (proyectan) un vector de características original en un espacio ortogonal en el que los elementos más importantes, que expresa la variabilidad bajo condiciones saludables, se eliminan (por estar relacionados con las condiciones ambientales y otras incertidumbres), mientras que los elementos con menos variabilidad se conservan, ya que se espera que sean aun afectados por el daño. Por supuesto, esto no puede ser generalmente garantizado y, como se muestra en [40], el enfoque no siempre logra un alto rendimiento.

Técnicas similares en filosofía incluyen *Kernel Principal Component Analysis*, que es una variante no lineal del PCA [75, 83], análisis factorial (*factor analysis*) [25] que trata de identificar un subespacio vectorial en la que los efectos ambientales se encuentran y luego proyecta las señales medidas en el subespacio ortogonal, técnicas de promedio (*averaging techniques*) [8] basadas en el método de espacio nulo (*null–space*) en el cual se usa una matriz de Hankel promedio obtenida teniendo en cuenta diferentes condidiones medioambientales, cointegración [19] que intenta encontrar y eliminar las tendencias comunes en señales sanas y dañadas que puedan ser causados por factores ambientales o incertidumbre de operación, un enfoque de selección negativa (*negative selection approach*) que utiliza una analogía con el sistema inmune [105], y un método que emplea una gran cantidad de sensores y filtros espaciales (*spatial filters*) para la obtención de una magnitud característica capaz de diferenciar entre el daño y los cambios ambientales [24]. Típicamente solo los registros de datos sanos se utilizan en la fase de aprendizaje de estos métodos (el caso de *aprendizaje no supervisado*) lo que puede ocasionar limitaciones en su eficacia, mientras que para ciertos métodos puede ser necesaria una gran cantidad de sensores.

B.1.5 Aplicación en el campo de la eólica

El diagnóstico de daños en estructuras de turbinas eólicas es de gran importancia práctica y económica. Sobre todo porque las estructuras, incluyendo la palas, están aumentando de tamaño en un esfuerzo por captar la mayor cantidad de energía del viento como sea posible. La necesidad de monitorizar continuamente el estado de salud de estas estructuras es por lo tanto evidente dado que en general la inspección visual no es una opción eficaz ni viable. Por otra parte, la tendencia actual en este campo es la de situar los parques eólicos en el mar, *offshore*, véase [15]. Una de las ventajas de este cambio de ubicación es

que el viento es más fuerte en las costas y, a diferencia del viento sobre el continente, las brisas marinas puede ser fuertes por la tarde, coincidiendo con el momento en que se está utilizando la mayor cantidad de electricidad, véase la Figura B.2. Una ventaja adicional, dependiendo de su ubicación, es que la contaminación visual ya no es un problema. Los aerogeneradores offshore también pueden estar ubicados cerca de las poblaciones a lo largo de las costas, lo que elimina la necesidad de una nuevas líneas de transmisión terrestres. Sin embargo, las plantas offshore tienen algunos inconvenientes [29, 16]:

- Se deben tener en cuenta las dificultades habituales para aerogeneradores onshore, que incluyen torres altas o grandes fuerzas generadas en el borde de la pala.
- Requisitos de larga vida útil de la estructura y un mínimo porcentaje de tiempo fuera de servicio.
- Los costes, incluyendo los de mantenimiento y operaciones, se incrementan significativamente en comparación con los costes onshore.
- Las condiciones del medio marino son mucho más exigentes.

Estos inconvenientes han aumentado el nivel de interés en la implementación de los diferentes conceptos de SHM en estas estructuras [17].

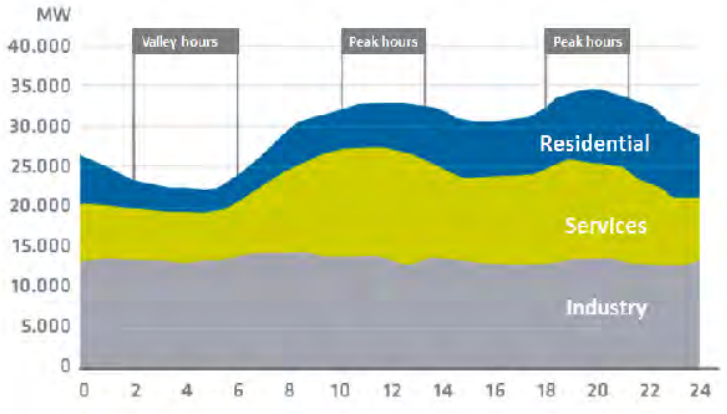

Figure B.2: Distribución de la demanda de energía eléctrica dividida por sectores, [3].

En este campo, la consideración de la variación en las condiciones ambientales y de operación es crucial. Para las turbinas eólicas las condiciones variables pueden deberse al clima (temperatura, humedad), velocidad del viento, velocidad de rotación variable, entre

otras, y pueden conducir a una detección de daño incorrecta si no se han tenido en cuenta adecuadamente.

Entre las diferentes partes de una turbina eólica, la torre no ha recibido demasiada atención en la literatura [54, 23], especialmente si se compara con otras partes como pueden ser las palas. En [13] se usan galgas extensiométricas para la detección de grietas en una torre de aerogenerador, siendo la estrategia más prometedora la que considera como indicador de la presencia de una grieta la diferencia de deformación entre dos galgas adyacentes. La principal limitación de este método es el número de sensores que necesitaría ser instalado.

Es evidente que las palas de la turbina eólica están sujetas a daños, y esto puede incluso provocar a daños en la torre [74, 44]. Los estudios previos [41] se han centrado en los cambios en frecuencias modales bajo diferentes escenarios de daños para una pala de aerogenerador de laboratorio a escala, llegando a la conclusión de que los primeros siete modos pueden ser suficientes para indicar daño. Sin embargo, no se lleva a cabo una detección de daño como tal.

En otro estudio [92], se llevan a cabo ensayos de fatiga en palas a tamaño real, utilizando los resultados para validar una variedad de métodos de SHM, como la emisión acústica, métodos basados en impedancia, o propagación de ondas. En [74] una sección de una pala de aerogenerador de 1 metro se analiza a través de diferentes métodos: propagación de ondas de Lamb, análisis de respuesta en frecuencia y métodos estadísticos de series de tiempo. El daño se simula mediante la adición de un pedazo de masilla en la superficie. Para todos los métodos, el índice de daño (magnitud característica) utilizado se ha obtenido a partir de correlaciones cruzadas entre una señal de referencia y una nueva señal en estado desconocido, bajo condiciones ligeramente variables (posición de la sección de la pala sobre la mesa). Las diferencias debido a los daños en este caso son más grandes que las debidas a las variaciones consideradas, y la detección se lleva a cabo mediante la comparación con una única señal de referencia sana, obteniendo en general buenos resultados.

En [28] se presentan una simulación y un experimento en el que la localización de los daños se realiza utilizando *wavelets*. En el caso experimental, se utiliza una pala de longitud 1,74 m, y el daño se simula mediante la adición de una masa en la superficie (del 2 al 12 % de la masa total). La pala se excita a través de un excitador electromecánico y se utiliza un vibrómetro láser Doppler (con 211 o 290 puntos de exploración) para la obtención de las formas modales. Se calculan las diferencias entre los coeficientes de la transformada *wavelet* en el estado sano y en el estado actual para la localización de daño.

En [107] también se emplean formas modales, usando wavelets 2D para la detección, localización y cuantificación del daño en una simulación de una pala de aerogenerador de 41,2 m. La principal limitación del método parece ser la gran cantidad de puntos de medición requeridos.

B.2 Análisis no estacionario: Método de la coherencia múltiple

En muchas aplicaciones industriales aparecen señales no estacionarias y su análisis teniendo en cuenta esta no estacionaridad es de primordial importancia [42]. Algunos ejemplos aparecen en eventos transitorios como una parada de emergencia o cuando se inicia una motor. Otros ejemplos incluyen puentes con vehículos en movimiento, aerogeneradores [6], aviones y muchos otros. Otro caso importante surge cuando una fuente de ruido se mueve con respecto al receptor, [32], o viceversa, este es el caso del ruido de paso (*pass–by noise*), o el ruido recibido en la cabina del ascensor. En este último caso, la señal medida en la punto receptor puede ser no estacionaria incluso si la señal emitida es estacionario (por ejemplo en amplitud, pero también en su contenido frecuencial, debido al efecto Doppler). En estos casos se hacen necesarias representaciones de tiempo–frecuencia para comprender el contenido de frecuencia de las señales y cómo varía con el tiempo.

B.2.1 Clasificación de métodos tiempo–frecuencia

Los métodos que tratan señales no estacionarias se pueden clasificar en paramétricos o no paramétricos en función del tipo de modelo adoptado. Entre los no paramétricos, que han sido los más utilizados en la literatura, algunos ejemplos son la Transformada de Fourier de Tiempo Corto (STFT por sus siglas en inglés, *Short Time Fourier Transform*) [18], la distribución de Wigner–Ville [55] o el análisis *wavelet* [103]. Los modelos paramétricos como Time depende ARMA [89] o modelos de espacio de estados [65], pertenecen a la segunda clase que, en general, ha recibido menos atención.

En el presente trabajo se presentan y comparan tres métodos particulares. Uno con un enfoque puramente no paramétrico, un segundo paramétrico en frecuencia y no paramétrica en tiempo y un tercero paramétrico tanto en tiempo como en frecuencia.

La idea principal de los dos primeros métodos considerados en elámbito de este trabajo es dividir la señal en bloques de tiempo corto, para así capturar la dependencia

temporal (de forma no paramétrica). Entonces la señal se limita a cada bloque y cada restricción será considerada estacionaria. Para cada bloque estacionario se aplicará una técnica clásica para señales estacionarias. Los procedimientos más convencionales se basan en técnicas que utilizan la Transformada Rápida de Fourier (FFT, por sus siglas en inglés, *Fast Fourier Transform*), y por tanto son no paramétricos (en frecuencia). La aplicación de esta técnica para cada bloque de tiempo es lo que se conoce como STFT. Estos métodos son muy atractivos debido a su eficiencia computacional y a su fácil aplicación. Sin embargo, los estimadores espectrales obtenidos tienen una alta variabilidad. Se han llevado a cabo algunos trabajos para superar esta gran variabilidad [112], mediante la aplicación de varias ventanas y el promediado de resultados, pero el estimador proporciona una limitada resolución temporal y frecuencial. Para superar algunas de las dificultades que aparecen en los métodos basados en la FFT (varianza alta/baja resolución) se puede aplicar un modelo paramétrico a cada bloque. Esto da lugar a una método que es no paramétrico en tiempo y paramétrico en frecuencia. Dentro del campo de la estimación paramétrica, los modelos más populares incluyen métodos AutoRegresivos de Media Movil (ARMA, por sus siglas en inglés, *AutoRegressive Moving Average*) [61, 87]. Estos métodos ofrecen una mejor resolución espectral en comparación con la proporcionada por los métodos basados en la FFT, a pesar de que también implican un alto coste computacional. En este caso se obtiene un modelo ARMA dependiente del tiempo (TARMA) en el que se tiene una variación de los parámetros no estructurada (en cada bloque, los parámetros se calculan independientemente). En el método basado en la FFT aumentar la resolución temporal, reduciendo el tamaño de los bloques, se traduce en una caída de la resolución espectral. En el caso de los métodos ARMA, una reducción de el tamaño del bloque reduce la eficiencia y la fiabilidad estadística del método de estimación, obteniéndose un modelo menos preciso. Sin embargo, en el último método, el modelo puede proporcionar una representación espectral, posiblemente errónea, de infinita resolución frecuencial.

Con el fin de manejar la dependencia temporal de una manera más natural y para disminuir el número de parámetros implicados, se puede considerar un modelo TARMA con una evolución determinista de los parámetros [50]. Esto significa que los parámetros van a evolucionar en una forma estructurada, representada por funciones que pertenecen a un espacio funcional específico [102]. Este es un método más elaborado, conocido como FS–TARMA. La base debe ser seleccionado de acuerdo con las características de la señal bajo estudio, ya que esto predeterminará el tipo de comportamiento que puede ser capturado. Si la señal presenta transiciones rápidas, entonces son más adecuadas funciones a trozos, como se sugiere en [53], de lo contrario, si se usan polinomios o funciones trigonométricas

la dependencia temporal obtenida será más suave. En esto proceso también la varianza necesita ser estimada. Una aproximación de la varianza utilizando polinomios de alto orden podría dar lugar a una aproximación no positiva, debido al fenómeno de Runge (véase [104], p. 186). Para evitar esto, se propone el uso de polinomios de Bernstein, ver Apéndice A.3, [78], para esta aproximación lo que conduce a una aproximación no negativa (lo cual será de importancia crucial en el cálculo de coherencias, como se verá más adelante). Una ventaja de los métodos FS–TARMA con respecto a los no estructurados es el bajo número de parámetros presentes en el modelo. Hay que señalar que el cálculo de estos parámetros es computacionalmente caro, ya que deben ser obtenidos de una vez, al contrario que en el caso no estructurada, donde para cada bloque los parámetros se pueden obtener de una manera independiente. Este tipo de métodos se han utilizado en [31] para identificar características de diferentes vehículos usando los coeficientes de este modelo, o en [32] para eliminar el eco de una señal proveniente de un altavoz en movimiento. En ambas aplicaciones la dinámica variante en el tiempo viene a partir de una fuente de ruido en movimiento (vehículo/altavoz).

Para muchos fines, será necesario trabajar con más de una señal. Un ejemplo importante es el caso de cálculo de coherencia entre las señales. El cálculo de coherencias es ampliamente utilizado en señales de electroencefalogramas (EEG) [66, 81] y en la industria del automóvil [86, 96]. Esta técnica permite obtener el grado de contribución de una fuente de ruido particular, al total ruido recibido en otro punto. En este caso se hace necesario el uso de modelos multivariables, en los que todas las señales se tratan juntas. Trabajos anteriores como [116] ya han introducido un concepto similar de coherencia basada en modelos FS–TAR para ser utilizados en aplicaciones biomédicas. Para los cálculos de coherencia, la alta varianza presente en el método STFT, reduce la relevancia estadística de los estimadores obtenidos, [116].

B.2.2 Aplicación en el campo de la elevación (ascensores)

El confort en un ascensor [57] depende básicamente de variables tales como la *vibración* durante el viaje, así como el *ruido* recibido en la cabina. Hay algunas medidas de referencia que pueden dar una idea de la calidad del viaje y también del estado actual de la instalación (ayudando a las operaciones de mantenimiento) [30]. El ruido recibido en la cabina puede ser transmitido a través de la estructura (lo que significa que es generado por la vibración de la estructura) también conocido como *ruido estructural* (en inglés *structure–borne*), o puede ser transmitido a través del aire, también conocido como *ruido aéreo* (en inglés

air–borne) [43].

En este trabajo, el objetivo es identificar las principales contribuciones tanto a la vibración como al ruido recibido en la cabina del ascensor durante un viaje. Para conseguir esto se registran medidas de diferentes posibles fuentes de ruido y vibración, así como el ruido y la vibración percibida en la cabina del ascensor.

B.3 Objetivos y organización de la tesis

En esta sección se incluyen los temas cubiertos en la presente tesis, junto con sus objetivos y contribuciones. Estos se presentan capítulo a capítulo:

- El Capítulo 2 presenta una implementación de un algoritmo de nivel 1, junto con su posible extensión a un algoritmo de nivel 2. La metodología se aplica en una torre de aerogenerador a escala en dos versiones, con y sin *jacket*. El método usado es un ejemplo de método paramétrico basado en vibraciones (modelo AR) que hace uso del análisis estadístico solo mediante señales de salida de la estructura. Los objetivos y contribuciones específicos son:

  1. Uso de una metodología paramétrica basada en vibraciones en una torre de aerogenerador a escala.
  2. Incluso con un único se sensor se cosiguen resultados de detección con mucha precisión.
  3. Análisis de los diferentes puntos y direcciones de medida.
  4. Se propone un enfoque global sumando los indicadores de daño de cada canal.
  5. Se consigue la identificación del daño basándose en un proceso de aprendizaje supervisado.

- El Capítulo 3 propone una novedosa metodología supervisada, no basada en modelos, de tipo PCA para la detección del daño bajo condiciones medioambientales cambiantes. La metodología propuesta, en tres formas diferentes, se valida en una pala de aerogenerador a escala bajo diferentes temperaturas y condiciones de humedad. Los objetivos y contribuciones específicos son:

  1. Desarrollo de una metodología estadística supervisada, no basada en modelos y de tipo PCA, para la detección de daño.

2. Consecución de un alto rendimiento bajo diferentes condiciones medioambientales e incertidumbre a través de un proceso de aprendizaje mejorado, que involucra el uso de datos sanos y en varios escenarios con daño (aprendizaje supervisado).
3. Validación del método en una pala de aerogenerador a escala.
4. Comparación de las diferentes implementaciones del método: de solo respuesta y de excitación–respuesta, paramétricos y no paramétricos.
5. Funcionamiento con un número bajo de sensores (incluso un solo sensor).
6. Funcionamiento en una banda de frecuencia baja.

- El Capítulo 4 trata el problema de disgnosis del daño en una pala de aerogenerador a escala. Para la detección del daño se propone un método basado en la FRF mientras que para la localización precisa se utiliza un método FP–ARX, considerando la pala como unidimensional. Los objetivos y contribuciones específicos son:

  1. Análisis de la viabilidad del diagnóstico de daño (detección y localización) en una pala de aerogenerador a escala.
  2. Uso de un solo par de señales vibratorias de excitación/respuesta.
  3. Funcionamiento en una banda de frecuencia baja.

- El Capítulo 5 considera diferentes aplicaciones reales y de laboratorio en el contexto de la coherencia múltiple de cara a la identificación de fuentes de ruido predominantes. Se presentan y comparan tres enfoques en diferentes situaciones: análisis univariable, ejemplo sencillo con dos entradas y una salida y un sistema real complejo. Los objetivos y contribuciones específicos son:

  1. Definición de coherencia múltiple para señales no estacionarias utilizando métodos no paramétricos, semi paramétricos y paramétricos.
  2. Introducción de polinomios de Bernstein para la aproximación de la varianza para asegurar una aproximación positiva/definida positiva.
  3. Aplicación del método de la coherencia múltiple en aplicaciones numéricas y de laboratorio.
  4. Análisis de un caso real de un ascensor con un alto número de fuentes medidas, para tratar de identificar las fuentes y los caminos predominantes en diferentes

salidas consideradas estudiando el efecto de las contribuciones estructurales y aéreas.

- El Capítulo 6 finalmente resume las conclusiones y presenta el trabajo futuro de la tesis desarrollada.

Appendix C

List of Publications

Ana Gómez González – Time series methods for SHM applications and multiple coherence computations: assessment in real and laboratory conditions.

Several publications in international conferences and journal papers have been produced during the development of this thesis. These are listed in the sequel:

- A. Gómez González, J. Rodríguez, X. Sagartzazu, A. Schuhmacher, I. Isasa, "Multiple Coherence Method in Time–Domain for the Analysis of the Transmission Paths of Noise and Vibrations with Non Stationary Signals", in *Proceedings of ISMA 2010*, pp. 3927–3941, Leuven (Belgium), September 2010.

- E. Zugasti, A. Gómez González, J. Anduaga, M.A. Arregui and F. Martínez, "Structural Fault Detection in a Laboratory Tower Using a NullSpace Algorithm", in *Proceedings of the 5th ECCOMAS Thematic Conference on Smart Structures and Materials (SMART11)*, Saarbrücken (Germany), July 2011.

- A. Gómez González, E. Zugasti, J. Anduaga, M.A. Arregui and F. Martínez, "Structural Fault Detection in a Laboratory Tower Using an AutoRegressive Algorithm", in *Proceedings of the 5th ECCOMAS Thematic Conference on Smart Structures and Materials (SMART11)*, Saarbrücken (Germany), July 2011.

- E. Zugasti, A. Gómez González, J. Anduaga, M.A. Arregui and F. Martínez, "Null–Space and AutoRegressive Damage Detection: a Comparative Study", in *Smart Materials and Structures*, vol. 21(2012) 085010 9pp.
  DOI: 10.1088/0964-1726/21/8/085010.

- E. Zugasti, A. Gómez González, J. Anduaga, M.A. Arregui and F. Martínez, "A Comparative Assessment of Two SHM Damage Detection Methods in a Laboratory Tower", in *Proceedings of the 4th International Conference Smart Materials, Structures and Systems (CIMTEC 2012)*, Montecatini Terme (Italy), July 2012.
  Also in *Advances in Science and Technology*, vol. 82, pp. 232–239
  DOI: 10.4028/www.scientific.net/AST.83.232.

- A. Gómez González, E. Zugasti and J. Anduaga, "Damage Identification in a Laboratory Offshore Wind Turbine Demonstrator", in *Proceedings of Damage Assessment of Structures X, DAMAS 2013*, Dublin (Ireland), July 2013.
  Also in *Key Engineering Materials*, vol. 569–570, 2013, pp. 555–562
  DOI: 10.4028/www.scientific.net/KEM.569-570.555.

- A. Gómez González and S.D. Fassois, "Vibration–Response–Based Damage Detection for Scale Wind Turbine Blades under Varying Environmental Conditions", in *Proceeding of RUZGEM 2013 Conference on Wind Energy Science and Technology*, Ankara (Turkey), October 2013.

- A. Gómez González and S.D. Fassois, "Vibration–Based Statistical Damage Detection for Scale Wind Turbine Blades under Varying Environmental Conditions", in *Proceeding of Surveillance 7*, Chartres (France), October 2013. – **Best Student Paper Award**

- A. Gómez González and S.D. Fassois, "Excitation and Vibration Response Based Damage Diagnosis in Wind Turbine Blades: an Exploratory Study", in *Proceedings of the International Conference on Modal Analysis Noise and Vibration Engineering (ISMA 2014)*, Leuven (Belgium), September 2014.

- A. Gómez González and S.D. Fassois, "A Supervised Vibration–Based Statistical Methodology for Damage Detection under Varying Environmental Conditions & its Laboratory Assessment with a Scale Wind Turbine Blade", in *Journal of Sound and Vibration*, 2016, vol. 366, pp. 484–500.

Bibliography

[1] Bernstein polynomials. https://en.wikipedia.org/wiki/Bernstein_polynomial.

[2] Chebyshev polynomials. https://en.wikipedia.org/wiki/Chebyshev_polynomials.

[3] Electricity demand. http://www.ree.es/es/red21/eficiencia-energetica-y-consumo-inteligente/nuestros-habitos-de-consumo.

[4] Legendre polynomials. https://en.wikipedia.org/wiki/Legendre_polynomials.

[5] R. J. Allemang and D. L. Brown. A correlation coefficient for modal vector analysis. In *Proceedings of the 1st international modal analysis conference*, volume 1, pages 110–116. SEM, Orlando, 1982.

[6] L. D. Avendaño-Valencia, M. D. Spiridonakos, and S. D. Fassois. In-operation identification of a wind turbine structure via non-stationary parametric models. In *Proceedings of the 8th International Workshop on Structural Health Monitoring IWSHM*, page 2611, 2011.

[7] D. Balageas, C.-P. Fritzen, and A. Güemes. *Structural health monitoring*, volume 493. Wiley Online Library, 2006.

[8] É. Balmès, M. Basseville, F. Bourquin, L. Mevel, H. Nasser, and F. Treyssède. Merging sensor data from multiple temperature scenarios for vibration monitoring of civil structures. *Structural health monitoring*, 7(2):129–142, 2008.

[9] M. Basseville, M. Abdelghani, and A. Benveniste. Subspace-based fault detection algorithms for vibration monitoring. *Automatica*, 36(1):101–109, 2000.

[10] M. Basseville, L. Mevel, and M. Goursat. Statistical model-based damage detection and localization: subspace-based residuals and damage-to-noise sensitivity ratios. *Journal of sound and vibration*, 275(3):769–794, 2004.

[11] A. Bellino, A. Fasana, L. Garibaldi, and S. Marchesiello. Pca-based detection of damage in time-varying systems. *Mechanical Systems and Signal Processing*, 24(7):2250–2260, 2010.

[12] J. S. Bendat and A. G. Piersol. Random data analysis and measurement procedures. *Measurement Science and Technology*, 11(12):1825, 2000.

[13] M. Benedetti, V. Fontanari, and D. Zonta. Structural health monitoring of wind towers: remote damage detection using strain sensors. *Smart Materials and Structures*, 20(5):055009, 2011.

[14] C. Boller. Structural health monitoring – an introduction and definitions. *Encyclopedia of Structural Health Monitoring*, 2009.

[15] C. Butterfield, W. Musial, and J. Jonkman. Overview of offshore wind technology. In *Presentation at the Chinese Renewable Energy Industry Association WindPower Conference, Shanghai, China*, 2007.

[16] S. Butterfield, W. Musial, J. Jonkman, P. Sclavounos, and L. Wayman. Engineering challenges for floating offshore wind turbines. In *Copenhagen Offshore Wind Conference, Copenhagen, Denmark*, pages 377–382. Citeseer, 2005.

[17] C. C. Ciang, J.-R. Lee, and H.-J. Bang. Structural health monitoring for a wind turbine system: a review of damage detection methods. *Measurement Science and Technology*, 19(12):1–20, 2008.

[18] L. Cohen. Time-frequency distributions-a review. *Proceedings of the IEEE*, 77(7):941–981, 1989.

[19] E. J. Cross, K. Worden, and Q. Chen. Cointegration: a novel approach for the removal of environmental trends in structural health monitoring data. *Proceedings of the Royal Society A: Mathematical, Physical and Engineering Science*, 467(2133):2712–2732, Sept. 2011.

[20] P. J. Davis. *Interpolation and approximation*. Courier Corporation, 1975.

[21] P. De Boe and J.-C. Golinval. Principal component analysis of a piezosensor array for damage localization. *Structural health monitoring*, 2(2):137–144, 2003.

[22] O. R. de Lautour and P. Omenzetter. Damage classification and estimation in experimental structures using time series analysis and pattern recognition. *Mechanical Systems and Signal Processing*, 24(5):1556–1569, 2010.

[23] G. de Novaes Pires, E. Alencar, and A. Kraj. Remote conditioning monitoring system for a hybrid wind diesel system-application at fernando de naronha island, brasil, 2010.

[24] A. Deraemaeker and A. Preumont. Vibration based damage detection using large array sensors and spatial filters. *Mechanical systems and signal processing*, 20(7):1615–1630, 2006.

[25] A. Deraemaeker, E. Reynders, G. D. Roeck, and J. Kullaa. Vibration-based structural health monitoring using output-only measurements under changing environment. *Mechanical Systems and Signal Processing*, 22(1):34 – 56, 2008.

[26] S. W. Doebling, C. R. Farrar, M. B. Prime, et al. A summary review of vibration-based damage identification methods. *Shock and vibration digest*, 30(2):91–105, 1998.

[27] S. W. Doebling, C. R. Farrar, M. B. Prime, and D. W. Shevitz. Damage identification and health monitoring of structural and mechanical systems from changes in their vibration characteristics: a literature review. Technical report, Los Alamos National Lab., NM (United States), 1996.

[28] L. Doliński and M. Krawczuk. Damage detection in turbine wind blades by vibration based methods. In *Journal of Physics: Conference Series*, volume 181, page 012086. IOP Publishing, 2009.

[29] M. Drewry and G. Georgiou. A review of ndt techniques for wind turbines. *Insight-Non-Destructive Testing and Condition Monitoring*, 49(3):137–141, 2007.

[30] T. Ebeling. Condition monitoring for elevators – an overview. Technical report, Issue 6, 2011.

[31] K. B. Eom. Analysis of acoustic signatures from moving vehicles using time-varying autoregressive models. *Multidimensional Systems and Signal Processing*, 10(4):357–378, 1999.

[32] C. Evers and J. Hopgood. Parametric modelling for single-channel blind dereverberation of speech from a moving speaker. *Signal Processing, IET*, 2(2):59–74, 2008.

[33] C. R. Farrar and S. W. Doebling. An overview of modal–based damage identification methods. In *Proceedings of DAMAS conference*, pages 269–278. Citeseer, 1997.

[34] C. R. Farrar, S. W. Doebling, and D. A. Nix. Vibration–based structural damage identification. *Philosophical Transactions of the Royal Society of London. Series A: Mathematical, Physical and Engineering Sciences*, 359(1778):131–149, 2001.

[35] C. R. Farrar and K. Worden. An introduction to structural health monitoring. *Philosophical Transactions of the Royal Society of London A: Mathematical, Physical and Engineering Sciences*, 365(1851):303–315, 2007.

[36] S. D. Fassois and F. P. Kopsaftopoulos. *Statistical time series methods for vibration based structural health monitoring*. Springer, 2013.

[37] S. D. Fassois and J. S. Sakellariou. Time-series methods for fault detection and identification in vibrating structures. *Philosophical Transactions of the Royal Society A-Mathematical Physical and Engineering Sciences*, 365(1851):411–448, feb 2007.

[38] S. D. Fassois and J. S. Sakellariou. Statistical time series methods for shm. *Encyclopedia of Structural Health Monitoring*, pages 443–472, 2009.

[39] S. D. Fassois and J. S. Sakellariou. Statistical time series methods for shm. *Encyclopedia of Structural Health Monitoring*, pages 443–472, 2009.

[40] B. L. G. Manson and W. Staszewski. Eliminating environmental effects from lamb wave-based structural health monitoring. In *Proceedings of ISMA2004*, 2004.

[41] S. N. Ganeriwala, V. Kanakasabai, and M. Richardson. Modes indicate cracks in wind turbine blades. In *Rotating Machinery, Structural Health Monitoring, Shock and Vibration, Volume 5*, pages 509–513. Springer, 2011.

[42] L. Garibaldi and S. D. Fassois. Special issue on the identification of time varying structures and systems. *Mechanical Systems and Signal Processing*, 47(1):1–2, 2014.

[43] K. Genuit. The sound quality of vehicle interior noise: a challenge for the nvh-engineers. *International Journal of Vehicle Noise and Vibration*, 1(1-2):158–168, 2004.

[44] A. Ghoshal, M. J. Sundaresan, M. J. Schulz, and P. Frank Pai. Structural health monitoring techniques for wind turbine blades. *Journal of Wind Engineering and Industrial Aerodynamics*, 85(3):309–324, 2000.

[45] D. F. Giraldo, S. J. Dyke, and J. M. Caicedo. Damage detection accommodating varying environmental conditions. *Structural Health Monitoring*, 5(2):155–172, 2006.

[46] A. Gómez González and S. Fassois. A supervised vibration-based statistical methodology for damage detection under varying environmental conditions & its laboratory assessment with a scale wind turbine blade. *Journal of Sound and Vibration*, 366:484–500, 2016.

[47] A. Gómez González and S. D. Fassois. Vibration–based statistical damage detction for scale wind turbine blades under varying environmental conditions. In *Proceedings of the Surveillance 7 International Conference*, Chartres, France, October 2013.

[48] A. Gómez González and S. D. Fassois. Vibration–response–based damage detection for scale wind turbine blades under varying environmental conditions. In *Proceedings of the Conference on Wind Energy Science and Technology, RUZGEM 2013*, Ankara, Turkey, October 2013.

[49] A. Gómez González, J. Rodrıguez, X. Sagartzazu, A. Schuhmacher, and I. Isasa. Multiple coherence method in time domain for the analysis of the transmission paths of noise and vibrations with non stationary signals. *Proceedings of ISMA 2010*, pages 3927–3941, 2010.

[50] Y. Grenier. Time-dependent arma modeling of nonstationary signals. *Acoustics, Speech and Signal Processing, IEEE Transactions on*, 31(4):899–911, 1983.

[51] M. J. Griffin. *Handbook of human vibration*. Academic press, 2012.

[52] P. Gudmundson. Eigenfrequency changes of structures due to cracks, notches or other geometrical changes. *Journal of the Mechanics and Physics of Solids*, 30(5):339–353, 1982.

[53] M. G. Hall, A. V. Oppenheim, and A. S. Willsky. Time-varying parametric modeling of speech. *Signal Processing*, 5(3):267–285, 1983.

[54] Z. Hameed, Y. Hong, Y. Cho, S. Ahn, and C. Song. Condition monitoring and fault detection of wind turbines and related algorithms: A review. *Renewable and Sustainable energy reviews*, 13(1):1–39, 2009.

[55] J. Hammond and P. White. The analysis of non-stationary signals using time-frequency methods. *Journal of Sound and Vibration*, 190(3):419–447, 1996.

[56] J. D. Hios and S. D. Fassois. Statistical damage detection in a smart structure under different temperatures via vibration testing: A global model based approach. *Key Engineering Materials*, 413-414:261–268, 2009.

[57] ISO18738:2003. Lifts (elevators) – measurement of lift ride quality. 2003.

[58] I. Jolliffe. *Principal component analysis*. Wiley Online Library, 2005.

[59] S. Kanev, F. Weber, and M. Verhaegen. Experimental validation of a finite-element model updating procedure. *Journal of Sound and Vibration*, 300(1):394–413, 2007.

[60] S. M. Kay. *Modern spectral estimation*. Pearson Education India, 1988.

[61] S. M. Kay and S. L. Marple Jr. Spectrum analysis–a modern perspective. *Proceedings of the IEEE*, 69(11):1380–1419, 1981.

[62] H. Kess and D. Adams. Investigation of operational and environmental variability effects on damage detection algorithms in a woven composite plate. *Mechanical systems and signal processing*, 21(6):2394–2405, 2007.

[63] J.-T. Kim, J.-H. Park, and B.-J. Lee. Vibration-based damage monitoring in model plate-girder bridges under uncertain temperature conditions. *Engineering Structures*, 29(7):1354 – 1365, 2007.

[64] J.-T. Kim, Y.-S. Ryu, H.-M. Cho, and N. Stubbs. Damage identification in beam-type structures: frequency-based method vs mode-shape-based method. *Engineering structures*, 25(1):57–67, 2003.

[65] G. Kitagawa. Non-gaussian state–space modeling of nonstationary time series. *Journal of the American statistical association*, 82(400):1032–1041, 1987.

[66] A. Klein, T. Sauer, A. Jedynak, and W. Skrandies. Conventional and wavelet coherence applied to sensory-evoked electrical brain activity. *Biomedical Engineering, IEEE Transactions on*, 53(2):266–272, 2006.

[67] C. G. Koh, L. M. See, and T. Balendra. Estimation of structural parameters in time domain: a substructure approach. *Earthquake Engineering & Structural Dynamics*, 20(8):787–801, 1991.

[68] F. Kopsaftopoulos and S. Fassois. Vibration based health monitoring for a lightweight truss structure: experimental assessment of several statistical time series methods. *Mechanical Systems and Signal Processing*, 24(7):1977–1997, 2010.

[69] F. Kopsaftopoulos and S. Fassois. A functional model based statistical time series method for vibration based damage detection, localization, and magnitude estimation. *Mechanical Systems and Signal Processing*, 2012.

[70] P. Kraemer. *Damage diagnosis approaches for structural health and condition monitoring of offshore wind energy plants*. PhD thesis, University of Siegen (in German), 2011.

[71] R. Y. Liang, J. Hu, and F. Choy. Theoretical study of crack-induced eigenfrequency changes on beam structures. *Journal of Engineering Mechanics*, 118:384–396, 1992.

[72] S. Liberatore and G. Carman. Power spectral density analysis for damage identification and location. *Journal of sound and vibration*, 274(3):761–776, 2004.

[73] N. Lieven and D. Ewins. Spatial correlation of mode shapes, the coordinate modal assurance criterion (comac). In *Proceedings of the sixth international modal analysis conference*, volume 1, pages 690–695, 1988.

[74] A. Light-Marquez, A. Sobin, G. Park, and K. Farinholt. Structural damage identification in wind turbine blades using piezoelectric active sensing. *Structural Dynamics and Renewable Energy, Volume 1*, pages 55–65, 2011.

[75] H. J. Lim, M. K. Kim, H. Sohn, and C. Y. Park. Impedance based damage detection under varying temperature and loading conditions. *NDT & E International*, 44(8):740–750, 2011.

[76] Y. Liu, S. B. Kim, A. Chattopadhyay, and D. T. Doyle. Application of system-identification techniques to health monitoring of on-orbit satellite boom structures. *Journal of Spacecraft and Rockets*, 48(4):589–598, 2011.

[77] L. Ljung. *System identification*. Wiley Online Library, 1999.

[78] G. G. Lorentz. *Bernstein polynomials*. American Mathematical Soc., 2012.

[79] S. L. Marple Jr. *Digital spectral analysis with applications*. Englewood Cliffs, NJ, Prentice-Hall, Inc., 1987.

[80] P. Michaelides and S. Fassois. Uncertain structural dynamics identification via a random coefficient arx model based method. In *Proceedings of the USD International Conference on Uncertainty in Structural Dynamics*, Leuven, Belgium, September 2012.

[81] A. M. F. Miranda de Sa, L. B. Felix, and A. F. C. Infantosi. A matrix-based algorithm for estimating multiple coherence of a periodic signal and its application to the multichannel eeg during sensory stimulation. *Biomedical Engineering, IEEE Transactions on*, 51(7):1140–1146, 2004.

[82] K. K. Nair, A. S. Kiremidjian, and K. H. Law. Time series-based damage detection and localization algorithm with application to the asce benchmark structure. *Journal of Sound and Vibration*, 291(1):349–368, 2006.

[83] C. K. Oh and H. Sohn. Damage diagnosis under environmental and operational variations using unsupervised support vector machine. *Journal of Sound and Vibration*, 325(1):224–239, 2009.

[84] F. W. Olver. *NIST handbook of mathematical functions*. Cambridge University Press, 2010.

[85] B. Peeters and G. De Roeck. One-year monitoring of the z24-bridge: environmental effects versus damage events. *Earthquake Engineering & Structural Dynamics*, 30(2):149–171, 2001.

[86] R. Potter. Matrix formulation of multiple and partial coherence. *The Journal of the Acoustical Society of America*, 61(3):776–781, 1977.

[87] A. Poulimenos and S. Fassois. Parametric time-domain methods for non-stationary random vibration modelling and analysis–a critical survey and comparison. *Mechanical Systems and Signal Processing*, 20(4):763–816, 2006.

[88] M. Priestley. Time-dependent spectral analysis and its application in prediction and control. *Journal of Sound and Vibration*, 17(4):517–534, 1971.

[89] T. S. Rao. The fitting of non-stationary time-series models with time-dependent parameters. *Journal of the Royal Statistical Society. Series B (Methodological)*, pages 312–322, 1970.

[90] D. Rizos, S. Fassois, Z. Marioli-Riga, and A. Karanika. Vibration-based skin damage statistical detection and restoration assessment in a stiffened aircraft panel. *Mechanical Systems and Signal Processing*, 22(2):315–337, 2008.

[91] G. D. Roeck. The state-of-the-art of damage detection by vibration monitoring: the simces experience. *Journal of Structural Control*, 10(2):127–134, 2003.

[92] M. A. Rumsey and J. A. Paquette. Structural health monitoring of wind turbine blades. In *The 15th International Symposium on: Smart Structures and Materials & Nondestructive Evaluation and Health Monitoring*, pages 69330E–69330E. International Society for Optics and Photonics, 2008.

[93] A. Rytter. *Vibrational based inspection of civil engineering structures*. PhD thesis, Department of Building Technology and Structural Engineering, Aalborg University, 1993.

[94] C. Sakaris, J. Sakellariou, and S. Fassois. A time series generalized functional model based method for vibration-based damage precise localization in structures consisting of 1d, 2d, and 3d elements. *Mechanical Systems and Signal Processing*, 74:199–213, 2016.

[95] J. Sakellariou and S. Fassois. Vibration based fault detection and identification in an aircraft skeleton structure via a stochastic functional model based method. *Mechanical Systems and Signal Processing*, 22(3):557–573, 2008.

[96] P. Sas and W. Dehandschutter. Active structural and acoustic control of structure-borne road noise in a passenger car. *Noise & Vibration Worldwide*, 30(5):17–27, 1999.

[97] J. Schäfer and K. Strimmer. A shrinkage approach to large-scale covariance matrix estimation and implications for functional genomics. *Statistical applications in genetics and molecular biology*, 4(1):1175–1189, 2005.

[98] S. Smith. Iterative matrix approximation for model updating. *Mechanical systems and signal processing*, 12(1):187–201, 1998.

[99] H. Sohn. Effects of environmental and operational variability on structural health monitoring. *Philosophical Transactions of the Royal Society A: Mathematical, Physical and Engineering Sciences*, 365(1851):539–560, 2007.

[100] H. Sohn, M. Dzwonczyk, E. G. Straser, A. S. Kiremidjian, K. H. Law, and T. Meng. An experimental study of temperature effect on modal parameters of the alamosa canyon bridge. *Earthquake Engineering & Structural Dynamics*, 28(8):879–897, 1999.

[101] H. Sohn and C. R. Farrar. Damage diagnosis using time series analysis of vibration signals. *Smart materials and structures*, 10(3):446–451, 2001.

[102] M. Spiridonakos and S. Fassois. Parametric identification of a time-varying structure based on vector vibration response measurements. *Mechanical Systems and Signal Processing*, 23(6):2029–2048, 2009.

[103] W. J. Staszewski and D. M. Wallace. Wavelet-based frequency response function for time–variant systems–an exploratory study. *Mechanical Systems and Signal Processing*, 47(1):35–49, 2014.

[104] E. Süli and D. F. Mayers. *An introduction to numerical analysis*. Cambridge university press, 2003.

[105] C. Surace and K. Worden. Novelty detection in a changing environment: A negative selection approach. *Mechanical Systems and Signal Processing*, 24(4):1114–1128, 2010.

[106] M. Trethewey. Window and overlap processing effects on power estimates from spectra. *Mechanical Systems and Signal Processing*, 14(2):267–278, 2000.

[107] M. D. Ulriksen, J. Skov, P. Kirkegaard, and L. Damkilde. Wavelet transformation for damage identification in wind turbine blades. In *Proceedings of the 32nd IMAC, A Conference and Exposition on Structural Dynamics*, 2014.

[108] L. Wang and T. H. Chan. Review of vibration-based damage detection and condition assessment of bridge structures using structural health monitoring. QUT Conference Proceedings, 2009.

[109] K. Worden, G. Manson, and N. Fieller. Damage detection using outlier analysis. *Journal of Sound and Vibration*, 229(3):647–667, 2000.

[110] K. Worden, H. Sohn, and C. Farrar. Novelty detection in a changing environment: regression and interpolation aproaches. *Journal of Sound and Vibration*, 258(4):741 – 761, 2002.

[111] Z. Xing and A. Mita. A substructure approach to local damage detection of shear structure. *Structural Control and Health Monitoring*, 19(2):309–318, 2012.

[112] Y. Xu, S. Haykin, and R. J. Racine. Multiple window time-frequency distribution and coherence of eeg using slepian sequences and hermite functions. *Biomedical Engineering, IEEE Transactions on*, 46(7):861–866, 1999.

[113] A.-M. Yan, P. De Boe, and J.-C. Golinval. Structural damage diagnosis by kalman model based on stochastic subspace identification. *Structural Health Monitoring*, 3(2):103–119, 2004.

[114] A.-M. Yan, G. Kerschen, P. D. Boe, and J.-C. Golinval. Structural damage diagnosis under varying environmental conditions - part i: A linear analysis. *Mechanical Systems and Signal Processing*, 19(4):847 – 864, 2005.

[115] K. C. Yap and D. C. Zimmerman. Optimal sensor placement for dynamic model correlation. In *Proceedings of the 18th International Modal Analysis Conference*, volume 4062, pages 607–612, 2000.

[116] H. Zhao, S. Lu, R. Zou, K. Ju, and K. H. Chon. Estimation of time-varying coherence function using time-varying transfer functions. *Annals of biomedical engineering*, 33(11):1582–1594, 2005.

[117] E. Zugasti, A. Gómez González, J. Anduaga, M. A. Arregui, and F. Martínez. Nullspace and autoregressive damage detection: a comparative study. *Smart Materials and Structures*, 21(8):085010, 2012.